DEVELOPMENT OF A NOVEL MICROREACTOR-BASED CALORIMETER FOR THE STUDY OF FAST EXOTHERMAL REACTIONS IN LIQUID PHASE

THÈSE N° 3069 (2004)

PRÉSENTÉE À LA FACULTÉ SCIENCES DE BASE

Institut des sciences et ingénierie chimiques

SECTION DE CHIMIE ET GÉNIE CHIMIQUE

ÉCOLE POLYTECHNIQUE FÉDÉRALE DE LAUSANNE

POUR L'OBTENTION DU GRADE DE DOCTEUR ÈS SCIENCES

PAR

Marie-Agnès SCHNEIDER

ingénieure chimiste diplômée EPF
de nationalité suisse et originaire de Genève (GE)

acceptée sur proposition du jury:

Prof. F. Stoessel, directeur de thèse
Prof. K. Hungerbühler, rapporteur
Dr F. Mascarello, rapporteur
Dr J. Schildknecht, rapporteur

Lausanne, EPFL
2004

A Christoph,

A mes parents

Le temps met tout en lumière

Thalès

Abstract

Following several tragic chemical accidents that have occurred in recent years, some directives concerning chemical process safety have been issued. The Seveso directive, for example, requires a precise description of the consequences of a possible chemical accident assuming a worst-case scenario. However, to build such scenarios and, hence, make chemical processes safe, profound knowledge of the kinetic and thermal parameters of the reactions in question is necessary.

These parameters are usually determined by calorimetric methods. However, in the existing commercial calorimeters the characterization of fast, exothermal reactions raises several problems. Indeed, on the one hand, it is difficult to maintain the isothermal conditions required to determine the kinetics simply and precisely. On the other hand, the calorimeter should be able to measure the heat flow generated as soon as the reactants are brought into contact. It should be able to do this without the need for a period of thermal equilibration that would perturb the measurements, and without any limitations due to the mixing of the reactants.

The aim of this work is to develop a calorimetric method that is particularly adapted to studying fast exothermal reactions. The proposed system combines a microreactor with a commercially available microcalorimeter.

In the first part of this project a flexible technique for constructing microreactors was chosen. The technique had to be precise, reproducible and inexpensive. The geometry of the microreactor had to fit into the cavity of the commercially available microcalorimeter. The technique chosen was the silk-screen printing of a thick film dielectric. This method makes it possible to build quickly and at low cost numerous microreactors that can be regarded as disposables. The geometry of the reaction channel can be varied and can be adapted to the type of reaction.

Once the microreactors were built, the degree of mixing obtained in the microchannels was estimated first by simulation and then by experiment. The flow in the reaction channel was found to be purely laminar and the mixing time corresponded to the time for radial diffusion. Due to the small size of the channels, the mixing time was found to be adequate and not limiting for the characterization of fast reactions.

The microreactor was then inserted into the cavity of the commercial calorimeter. The resulting microsystem was calibrated using the neutralization reaction of sulphuric acid with NaOH. This system was further modified to optimize the thermal transfer between the reaction channel and

the sensor of the microcalorimeter and to increase its thermal efficiency. Finally, an electrical preheating system of the incoming liquids was put in place and tested.

Once the quality of the thermal signal had been optimized, kinetic studies of chemical reactions could be undertaken. First, a model reaction was studied in order to validate the results obtained with the microsystem and to avoid the risk of systematic errors. In the second stage, a previously unknown fast exothermal reaction was characterized. The heat flows measured during the reaction reached 160'000 $W \cdot kg^{-1}$ but the conditions, however, remained completely isothermal. The global kinetics of this reaction as well as its activation energy were determined.

Version abrégée

A la suite des tragiques accidents chimiques survenus ces dernières années, plusieurs directives concernant la sécurité des procédés chimiques ont été établies. La directive Seveso requiert par exemple la connaissance précise des conséquences d'un éventuel accident chimique en prenant en considération le scénario le plus dramatique. Or la construction de ce type de scénario et la sécurisation des procédés chimiques nécessitent une bonne connaissance des paramètres cinétiques et thermiques des réactions impliquées.

La détermination de ces paramètres se fait habituellement par des méthodes calorimétriques. Il apparaît néanmoins que, dans les calorimètres commerciaux, la caractérisation de réactions rapides et exothermiques pose problème. Effectivement, d'une part, le maintien de conditions isothermes nécessaires à la détermination simple et précise de cinétiques est difficile. D'autre part, le calorimètre doit permettre de mesurer le flux thermique généré dès la mise en contact des réactifs sans qu'une période d'équilibration thermique ne gêne les mesures ou que le temps de mélange des réactifs ne limite la réaction.

Le but de ce travail est de développer une méthode calorimétrique spécialement adaptée à l'étude de ce type de réactions rapides et exothermiques. Le système proposé combine un microréacteur avec un microcalorimètre commercial.

La première partie de ce travail consiste à trouver une technique de construction de microréacteur flexible qui soit à la fois précise, reproductible et peu coûteuse. La géométrie de ce microréacteur est très limitée par celle de la cavité du microcalorimètre commercial. La technique choisie est la sérigraphie d'une couche épaisse de diélectrique. Cette méthode permet de construire rapidement et à faible coût de nombreux microréacteurs qui pourront ainsi être utilisés comme consommables. La géométrie du canal de réaction peut être variée et adaptée au type de réaction étudiée.

Une fois ces microréacteurs construits, le degré de mélange obtenu dans les microcanaux est évalué par simulation d'une part et expérimentalement d'autre part. Il apparaît que l'écoulement dans le canal de réaction est purement laminaire et que le temps de mélange correspond au temps de diffusion radial. Etant donné la petite taille des canaux, ce temps de mélange s'avère être satisfaisant et ne limite pas la caractérisation de réactions rapides.

Le microréacteur est alors inséré dans la cavité calorimétrique. Le nouveau microsystème ainsi obtenu est calibré avec la réaction de neutralisation de l'acide sulfurique par NaOH. Le microsystème est par la suite modifié afin d'optimiser le transfert thermique entre le canal de

réaction et les senseurs du microcalorimètre et d'augmenter ainsi son efficacité thermique. Enfin, un préchauffage électrique des liquides entrants est mis en place et testé.

La qualité du signal thermique étant améliorée, l'étude cinétique de réactions chimiques peut être investiguée. L'étude d'une réaction modèle est tout d'abord menée afin de valider les résultats obtenus avec le microsystème et d'éviter le risque d'erreurs systématiques. Finalement, une réaction rapide et exothermique, jusqu'alors inconnue, est caractérisée. Les flux thermiques mesurés lors de l'étude de cette dernière réaction atteignent 160'000 $W \cdot kg^{-1}$ et les conditions restent néanmoins complètement isothermes. La cinétique globale de cette réaction ainsi que son énergie d'activation peuvent ainsi être rapidement déterminées.

Acknowledgments

First of all, I would like to thank my supervisor Professor Stoessel. I am grateful to him not only for the deep scientific support and the help in writing my thesis but also for his numerous efforts for providing me the best working conditions.

This thesis was an industrial project financed by Hoffmann-la-Roche AG Division Pharma and DSM Nutritional Product. Sincere thanks to Dr. Schildknecht, Dr. Mascarello and J. Jeisy for having closely followed the project from the beginning until the end and for our numerous fruitful discussions. I would also like to thank Dr. Schildknecht and Dr. Mascarello for accepting being part of my thesis jury.

Besides I am grateful to Professor Hungerbühler for being part of my jury and to Professor Von Stockar for accepting directing my Jury.

At the beginning, this PhD was performed in collaboration with the "Laboratoire des systèmes robotiques" of the EPFL microengineering department. I would like to deeply thank Valia Fascio who spent much time helping me using their prototype and supporting me with her humor and constant good mood.

We then started collaboration with the Laboratory of microtechnical production also belonging to the microengineering department. Dr. Thomas Maeder greatly helped me in the field of material science and gave me various useful ideas for the development of the microreactor as well as for the establishment of the heat flow balance of the system. For that, I would like to thank him.
All this work would however not have been done without Giancarlo Corradini and Caroline Jacq who constructed the microreactors and improved the standard technique of the laboratory for the need of the project. Moreover I thank Boris Moll and Matthias Garcin, members of the same laboratory.

My thank goes to Blanca Alonso who carried out reference measurements on a Calvet calorimeter during 5 months and supported me in my project during that time.

I am grateful for the valuable technical support of the “Atelier mécanique” and of the “Atelier d’électronique” where always someone was ready to help with any kind of problems. Additionally, I also would like to thank all my colleges at the EPFL for the pleasant work atmosphere. Special thank goes to Philip for his help with computers.

Sincere thanks to all my friends from Lausanne and Zurich especially to Céline, Camille and Anna for all the pleasant moments we spent together.

Last but not least, I would like to deeply thank my family for their advice and moral support during the last 25 years. Special thanks to my father who helped me a lot in improving my manuscript.
My greatest gratitude and fondness goes to my friend Christoph. His love, generosity, positive thinking and his cooking :) were for me an essential source of energy and confidence throughout these years.

Contents

Nomenclature

Abbreviation

MTT	Maximum temperature for technical reasons
MTSR	Maximum temperature of the synthesis reaction
TMR_{ad}	Time to maximum rate under adiabatic conditions
CFD	Computational fluid dynamics
DSC	Differential scanning calorimeter
WEDG	Wire Electrodischarge Grinding
SEM	Scanning electron microscopy

Symbol

Latin letters

A	Contact area	$[m^2]$
c	Concentration	$[mol \cdot l^{-1}]$
C_p	Heat capacity	$[kJ \cdot kg^{-1} \cdot K^{-1}]$
d	Diameter	[m]
d_h	Hydraulic diameter of the channel	[m]
d_{eff}	Effective diameter	[m]
D_m	Molecular diffusion	$[m^2 \cdot s^{-1}]$
D_{ax}	Axial diffusion	$[m^2 \cdot s^{-1}]$
e	Depth of the channel	[m]
E	Distribution	
E_a	Activation energy	$[J \cdot mol^{-1}]$
f	function	

f_{Re}	Laminar friction factor	[-]
F	Correction factor	[-]
F	Volume force	$[N \cdot m^{-3}]$
ΔH_R	Enthalpy of reaction	$[J \cdot mol^{-1}]$
ID	Inner diameter of the tube	[m]
k	Kinetic constant	[unit depending on reaction order]
k^0	Frequency factor	[unit depending on reaction order]
L	Length of the reaction channel	[m]
m	Mass	[kg]
M	Stoechiometric factor	[-]
$\dot{N}$	Molar flow rate	$[mol \cdot s^{-1}]$
N_{th}	Number of thermocouples	[-]
OD	Outer diameter of the tube	[m]
P	Pressure	[Pa]
P	Wetted perimeter	[m]
Q	Energy	[J]
Q'	Specific energy	$[J \cdot kg^{-1}]$
$\dot{q}$	Heat flow	[W]
r	Radial coordinate	[m]
R	Radius	[m]
R	Molar gas constant	$[J \cdot mol^{-1} \cdot K^{-1}]$
R	Chemical reaction rate	$[mol \cdot l^{-1} \cdot s^{-1}]$
R	Resistance	$[K \cdot W^{-1}]$
S_q	Sensitivity	$[V \cdot W^{-1}]$
t	Time	[s]
T	Temperature	[K]
u	Linear velocity	$[m \cdot s^{-1}]$
U	Output voltage	[V]
$\dot{V}$	Flow rate	$[l \cdot s^{-1}]$
X	Conversion rate	[-]

Greek letters

α_{th}	Seebeck coefficient of the thermocouple	$[V \cdot K^{-1}]$
χ	Constant	[-]

δ	Thickness of a layer	[m]
ΔH_{mix}	Enthalpy of mixing	[$J \cdot mol^{-1}$]
ΔH_r	Enthalpy of reaction	[$J \cdot mol^{-1}$]
ΔT	Temperature rise	[K]
Δp	Pressure drop	[Pa]
λ	Thermal conductivity	[$W \cdot m^{-1} \cdot K^{-1}$]
τ	Space time	[s]
μ	Dynamic viscosity	[$kg \cdot m^{-1} \cdot s^{-1}$]
ρ	Density	[$kg \cdot m^{-3}$]

Script

Subscript

0	Initial condition
1	Of first order
2	Of second order
A, B	Reactant A or B
ad	Under adiabatic condition
ax	Axial
contact	Thermal contact
D	Diffusion
i	Solute i
IC	Integrated circuit
ex	Exchange
f	Final value
Heat carrier	Heat carrier layer
loss	Thermal loss
m	Molecular
meas	Obtain experimentally
mesh	Of the mesh
p	Process
r	Reaction medium
rx	Chemical reaction
th	Thermocouple

Superscript

$\bar{}$	Average value
’	Specific value (relating to mass)
.	Flow (relating to time)
hr	Obtained using a heater resistance
rx	Obtained using a chemical reaction

Dimensionless numbers

Bo	Bodenstein number	[-]	$Bo = \frac{u}{D_{ax}} \cdot L$
Pe	Peclet number	[-]	$Pe = \frac{u \cdot d}{D_m}$
Re	Reynolds number	[-]	$\mathrm{Re} = \frac{\rho \cdot u \cdot d}{\mu}$

Chapter 1

INTRODUCTION

Despite the numerous benefits provided by the chemical industry in our daily lives, most citizens consider chemistry as a threat to human beings and to the environment. Even if, according to the statistics, the risk of chemical accidents is low compared to other industrial activities, these accidents are often spectacular, badly understood by the public and particularly terrifying. The tragic accidents of Seveso in 1976 and Bhopal in 1984 have intensified the fear in society [1, 2].
The dioxin spread out in the atmosphere during the Seveso disaster destroyed large amounts of vegetation and killed about 3300 animals [3]. Numerous people in the affected areas suffered from skin lesions and other symptoms. The consequences of the Bhopal accident were even more dramatic since more than 3800 people were killed and 250'000 were injured [4]. The images of the panic and the horror of this chemical accident are still in everybody's mind. In Switzerland, the fire of November 1st, 1986 in Schweizerhalle near Basel [5] generated a catastrophic pollution of the Rhine river and had an extremely negative impact on the general perception of the Swiss chemistry.

In the last decades, the chemical industry has considerably improved and systematized safety analyses. Efforts and consciousness for safety issues were recently even further strengthened and reinforced by the explosion at AZF in 2001 (Toulouse) killing 29 persons and injuring 700 people. The public reaction to these accidents resulted in the establishment of major process safety legislations like the Seveso Directive or the Ordinance for the prevention of major accidents (OPAM) in Switzerland. These laws have given very strong support to the implementation of risk assessment and risk management methodologies for controlling dangerous technologies. In addition, industries developed a strong safety culture especially in process design.

Integration of chemical process safety in the early stages of process development is an important task in the optimization of the process reliability and ultimately lowers the risks and the costs.

Knowing the hazards requires a more extensive knowledge of the dynamic behavior of a reaction not only under normal operation conditions but also under deviation conditions. Designing a safe process or establishing safety measures for a process are directly related to the thermal potential of the reactions. The determination of the global kinetics and of the enthalpy of the reactions is required for a process safety analysis. This is explained in more detail in the next section.

1.1 ASSESSMENT OF THE THERMAL RISK OF A REACTION

A complete safety analysis consists of three steps, the danger identification, the risk analysis and the establishment of risk-reducing measures. For chemical process safety analysis, the behavior of a chemical system is commonly evaluated by building a run-away scenario and assessing the expected effects and the criticity of the latter.

In case of loss of the temperature control (for example cooling failure) during the process, the reaction carries out in a quasi-adiabatic mode. The main consequences will be an increase of the temperature and therefore of the reaction rate, the potential activation of secondary reactions and a pressure increase due to the evaporation of reaction components or due to decomposition gases. The maximum temperature achieved by the reaction mixture as well as the time available before a possible thermal explosion are extremely important parameters for the risk assessment of the reaction.

The scheme of the thermal run-away of a reaction is represented in Figure 1-1.

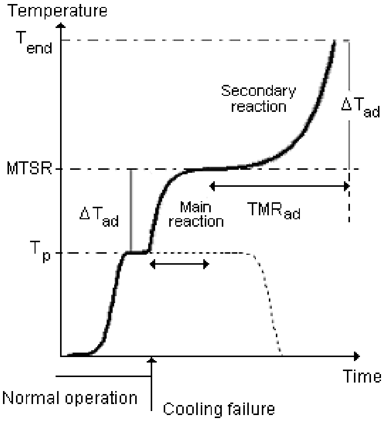

Figure 1-1: Schematic representation of a reaction run-away in a batch reactor.

The different steps of this run-away scenario relating to the main reaction and to the secondary reaction are discussed in the next paragraphs focusing on the importance of knowing the thermal and kinetic parameters for mastering the reactions.

Main reaction

The knowledge of the global kinetics of the main reaction is of crucial importance for the reactor design and for the process development. It is important to know, for example in a multi-step reaction, which steps are critical for the selectivity and for the productivity of the production line. Even if the latter are of particular importance for the optimization of the production conditions, the knowledge of the global kinetics is also required for the determination of the accumulation in the reactor, which is critical in safety analysis.

As represented in Figure 1-1, in case of cooling failure, the heat released by the reaction leads to a temperature increase of the system. The maximum temperature achieved due solely to the main reaction (also called synthesis reaction) is designated *MTSR* (Maximum temperature of the synthesis reaction) and is calculated as follows:

$$MTSR = T_p + (1 - X) \cdot \Delta T_{ad} \text{ with } \Delta T_{ad} = \frac{Q'_r}{C_p} \tag{1.1}$$

This value is correlated to the degree of accumulation of the non-converted controlling reactant [6]. In the worst case scenario, the conversion of the reactant is equal to zero and the temperature increase corresponds to the overall adiabatic temperature rise (ΔT_{ad}).

The consequences of the scenario depend on the level of the *MTSR* in relation with the maximum temperature tolerable for technical reasons (*MTT)* and the temperature at which a potential secondary reaction (e.g. decomposition reaction) becomes significant (see Figure 1-1). The *MTT* can, for example, be the boiling point of the solvent (for an open vessel), or the temperature at which the maximum bearable pressure is achieved (for a closed vessel). The criticity of the potential secondary reaction is detailed below.

Secondary reaction

According to the Arrhenius expression, secondary reactions may take place theoretically at any temperature. However at low temperatures, they become so slow that the time required for the reaction to become critical tends to infinite. In order to settle the definition of what a critical temperature is, it is commonly considered that the reaction rate becomes critical when the time required to reach the maximum rate of the reaction TMR_{ad} becomes shorter than a chosen limit e.g. 24 hours.

The time to maximum rate TMR_{ad} is calculated using the following expression:

$$TMR_{ad} = \frac{C_p \cdot R \cdot T_0^2}{\dot{q}_0 \cdot E_a} \tag{1.2}$$

This time characterizes the probability of occurrence of the run-away. The longer the time, the greater is the probability of avoiding the run-away. This probability is considered as high for TMR_{ad} shorter than 8 hours and low for a TMR_{ad} longer than 24 hours [7].

The effect of the run-away will be seriously affected by the presence, or absence, of a secondary reaction and by its thermal and kinetic parameters.

As shown in equation (1.2), the calculation of the TMR_{ad} requires the knowledge of the activation energy and of the power as a function of temperature.

The TMR_{ad} allows the prediction of the behavior of the decomposition in the early stage of the run-away and therefore the establishment of preventive measures. The best safety measures that can be taken consists of using a inherently safer design [8] e.g. using a semi-batch or continuous process instead of a batch process or using a heating medium, which has a maximum temperature that is too low for the reaction mixture to decompose. Above all, the preferable way for avoiding any hazard is of course to replace a hazardous compound by a safer one, but this is unfortunately often not applicable. If the process cannot be rendered inherently safer, it can still be controlled by the use of sensors, alarms and other control systems that either take automatic action or allow for manual intervention to prevent the development of uncontrolled reaction. Specifying such preventive measures requires a thorough understanding of the chemical process involved, especially the limits of safe operation.

The knowledge of the thermal and kinetic parameters of the secondary reaction is also needed to predict the behavior of the decomposition in the late stage of the run-away and to establish protective or emergency measures in case of failure of the preventive ones. This could be for example to fit emergency relief vents and to ensure the evacuation of the product to a safe place; it could also be e.g. the dumping of the reaction products into a quenching fluid. The prediction of the consequences of a potential chemical accident in a worst case scenario is an important element required by the Seveso directive.

As a conclusion, the global kinetics of both the main and the secondary reaction(s) are required for the establishment of the run-away scenario of the chemical system and thus for the safety analysis of the process.

1.2 MOTIVATION OF THIS WORK

Global kinetics of reactions can be determined by various methods. However, calorimetric methods are preferred for chemical process safety analysis since they allow to directly measure the effect that should be mastered or avoided. Many different calorimetric systems have been developed during the last decades and chapter 2 proposes an overview of the existing systems.

However, fast and highly exothermal reactions are still difficult to characterize in classical systems.
Indeed, measuring high heat release rates under isothermal conditions or at least under strict temperature control requires extremely **high heat exchange rates**.
Moreover, according to the inherent safety principle, such reactions should preferably be studied at small scale, thus involving **small amounts** of very reactive compounds. The use of small quantities is also an advantage when performing safety studies at an early stage of development, when large amounts of compounds are not available or are expensive.
Finally, for fast reactions, **rapid mixing** as well as a precise **control of the reaction start** are mandatory.

The use of a **microreactor-based calorimeter** fulfills all of these requirements:

- The high surface to volume ratio provides a highly efficient heat transfer,
- The small volume of the microchannel means that only small amounts of potentially dangerous chemicals are used,
- The small radius of the microchannel results in short time for radial diffusion and thus good mass transfer,
- The microreactor can be designed as a plug-flow reactor operating continuously at steady state. The reactants are mixed at the beginning of the reaction microchannel. This allows a good control of the reaction start as well as a measurement of the thermal effects as soon as the reactants mix without any perturbation due to the mixing.

A commercially available calorimeter with a high thermal sensitivity can be used to ensure the calorimetric measurement line.

Figure 1-2 summarizes the purpose of the construction of a microreactor-based calorimeter.

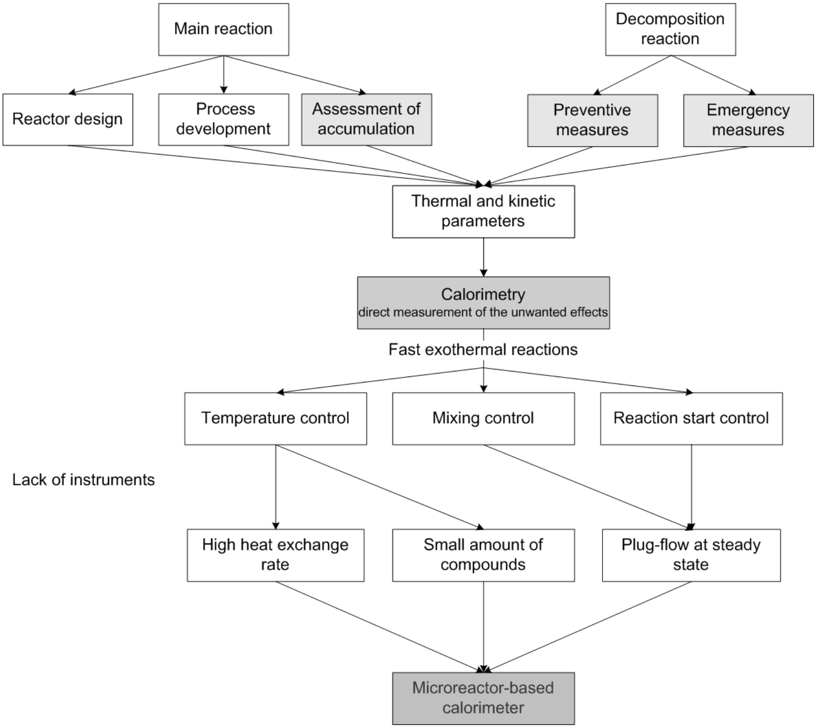

Figure 1-2: The "requirement tree" - scheme representing the purposes of the construction of a microreactor-based calorimeter. In light grey: items directly related to chemical process safety, in dark grey: main items.

The microsystem developed in this work is based on the commercially available microcalorimeter Setline 120 from SETARAM (France). The work principle of this calorimeter is detailed in chapter 2. This microcalorimeter is basically similar to a DSC except that a single crucible containing the reactant is used and no reference crucible is needed.

The basic concept of our project was to replace the crucible used for conventional measurements by a flow-through microfluidic system. The reactants mix at the beginning of the reaction channel and once steady state is reached, the heat released by the reaction and conducted to the sensor of the calorimetric system is analyzed.

Chapter 2

CALORIMETRY AND FLOW-THROUGH MICROCALORIMETERS

2.1 INTRODUCTION

Calorimetry is a broadly used technique for the determination of thermodynamic properties of chemical compounds or materials and for the characterization of reaction kinetics. Predictions for run-away reactions, risk analysis and optimization of risk-reducing measurements are fundamental aspects of safety issues and require the use of calorimetric data. Numerous different calorimeters have been developed in recent years to investigate the broad variety of problems encountered.

This chapter presents a general description of the context of the project. The literature related to specific parts of the project (microchannel construction, assessment of the degree of mixing, reaction kinetics…) is discussed in the corresponding chapters.

An overview of the existing calorimetric systems is first presented focusing on the calorimeters used during this project and on the developments in the field of flow-through microcalorimeters in the last decades. The advantages of microreactors are then briefly explained.

2.2 OVERWIEW OF COMMERCIALLY AVAILABLE CALORIMETRIC SYSTEMS USED IN SAFETY LABORATORIES

2.2.1 General overview

The first calorimeter ever reported was an ice calorimeter developed by Lavoisier and Laplace in 1780 to study the respiration of a guinea pig. A thermodynamic and kinetic evaluation of respiration was derived from the amount of water collected and the rate of melting. Since then, considerable progress has been made in calorimeter technology and many different designs of calorimeters have been reported.

Several overviews of calorimeters have been published [9-12]. These are summarized in the next paragraphs. Thermal analysis groups different experimental methods for the determination of physical and chemical properties of substances. However no universally agreed system of classification can be found in the literature. Hemminger and al. [13] proposed a classification based first on the measuring principles, then on the mode of operation and finally on the principle of construction. In the brief overview proposed here, we will first explain the modes of operation and then discuss the measuring principles of classical calorimeters using a classification close to the one proposed by Regenass [14].

Modes of operation

There are four modes of operation for calorimetric measurements: the temperature-scanning mode, the isothermal mode, the isoperibolic mode and the adiabatic mode.
In the **temperature scanning mode**, the reaction system is heated in an oven following a programmed temperature ramp. This type of measurements provides a general overview of the thermal activity of a substance or a mixture over a broad range of temperatures e.g. fusion, reaction or decomposition and allows determining quantitatively the energy corresponding to these transformations. In the **isothermal mode**, the reaction system is maintained close to constant temperature. Isothermal measurements distinguish the influence of temperature on the reaction rate from the influence of the conversion on the heat flux. This mode thus offers an easy way for determining the kinetic parameters of a reaction. Moreover, autocatalytic reactions can be detected (except with flow-through calorimeters). In the **isoperibolic mode**, the temperature of the environment is maintained constant and the temperature of the reaction system varies (as well as the heat flow). These calorimeters are mainly considered as semi-quantitative and used for screening purposes or for decomposition studies. Finally, in the **adiabatic mode**, the heat released by the reaction is entirely maintained in the system and there is no heat exchange with the environment. This method allows to follow the evolution of the temperature as a function of time, and to determine the Time to Maximal Rate (TMR_{ad}) starting from various temperatures. Activation energies and reaction rates can also been derived from this method.

Measuring principles

Regenass et al. [14] proposed to divide calorimetric methods into two categories, calorimeters using **heat accumulation methods** and calorimeters using **heat flow methods**.

In **heat accumulation** methods, there is no heat flow exchanged with the environment ($\dot{q}_{ex} = 0$) and the heat flow released or consumed by the sample leads to a temperature variation in the cell, which is measured.

Instruments working in adiabatic conditions use the heat accumulation method. For adiabatic measurements, this method can be further divided into two sub-categories depending on the technique used to avoid thermal exchange with the surrounding: these are *thermal isolation* (Dewar) and *power compensation*. Most recent adiabatic calorimeters use the power compensation method, which means in this case that the temperature of the environment is regulated to follow the temperature of the reaction system. This is the case with the Accelerating Rate Calorimeter (ARC). This calorimeter works in a "heat-wait-search" mode; the temperature of the reaction system is increased and then maintained to provide a thermal equilibrium. If the self-increase of the sample temperature is lower than a fixed value, the reaction system is further heated until a temperature increase rate surpassing a predefined level is detected. The calorimeter then switches to the adiabatic mode i.e. the oven temperature follows the exponentially increasing sample temperature. The run-away curve is directly measured. Many other types of adiabatic calorimeters have been reported such as the Vent Sizing Package (VSP) or the Reactive System Screening Tool (RSST). The Automatic pressure Tracking Adiabatic Calorimeter (APTAC) shows interesting properties since it withstands a maximal pressure of 140 bars and allows to follow temperature increases up to 400°C/min.

In the case of instruments working in an isoperibolic mode, the measuring principle is similar since a temperature difference is measured. However part of the heat flow released is exchanged with the surroundings. Even if the data obtained in isoperibolic mode are difficult to interpret, most calorimeters operate in this mode because, such systems are easier to construct since the heat flow control is passive. This is the case for example with the semi-quantitative calorimeters SEDEX, RADEX and SIKAREX. The Differential Scanning calorimeter (DSC) after Boersma also uses this principle. The temperature difference between the sample and a reference is measured. The instrument is calibrated to define the heat corresponding to the temperature difference. As long as the temperature fluctuations are sufficiently small, the latter is considered as an isothermal mode. This is only valid for small samples as used in a DSC.

In **heat flow methods**, in the ideal case, the heat flow is entirely exchanged with the environment ($\dot{q}_{ex} = \dot{q}_r$) and the temperature is maintained constant. This technique allows to operate in isothermal conditions. The instruments using this method can be classified according to the technique used to control the heat flow. If there is no control system ensuring that the heat flow is completely driven to the surrounding, there may be a partial heat accumulation and this leads to an isoperibolic instrument (described above). In fact, many isothermal calorimeters do not effectively work in strictly isothermal conditions but, as explained above with the DSC after Boersma, small temperature variations are neglected.

The heat flow control can mainly be achieved by *power compensation* or *heat conduction*. The "true" DSC (differential scanning calorimeter) is an example of a calorimeter using *power compensation*. Any temperature difference between sample and reference crucible is immediately compensated by appropriate changes in the heating of Peltier elements located below the crucibles. Both the sample and reference temperatures are thus maintained equal and the power required for this operation is determined. A compensation heater can also be introduced directly in the reaction mixture to counter-balance the heat of reaction. Most heat flow calorimeters use this principle. The reaction calorimeter developed by Schildknecht et al. [15] is an example of a calorimeter using a compensation heater. In this system, a constant temperature difference is maintained between the liquid in the reactor jacket and the reaction mass in order to achieve a constant heat flow from the reactor to the jacket. A compensation heater immersed in the reaction mass maintains the reactor temperature equal to a preset temperature. The electrical input required is measured and compared to the baseline electrical input (without reaction).

In *heat conduction* calorimeters, the temperature gradient is propagated to or from a heat sink. The heat sink can for example be a thermostated water (or oil) bath (Thermal Activity Monitor TAM, Reaction Calorimeter RC1), a thermostated air box (in the LKB calorimeter described below), a temperature-regulated Peltier unit (in the Setline 120) or a thermoelectric pile (in the Calvet Calorimeter C80 or BT 215).

Working range

All of these calorimeters have different usability domains and can be classified according to their working temperature range and to the range of heat flows that can be measured (Figure 2-1).

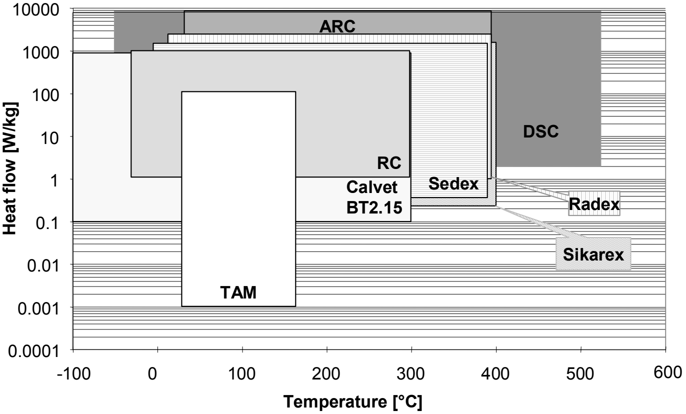

Figure 2-1: Classification of the main calorimeters according to their working range [16].

The basic working principles of selected commercially available calorimeter are summarized in Table 2-1.

Table 2-1: Summary of the characteristics of selected commercially available calorimeters [17]

Technique	Examples of manufacturer	Working principle	Domain of use	Sample size [g]
RC	Mettler-Toledo, HEL, CPI	Isotherm **Heat flow** *(Heat conduction)*	Reactions	300-2000
Calvet	Setaram	Isotherm **Heat flow** *(Heat conduction)* Differential	Reactions, decompositions	0.5-3
TAM	Thermometric	Isotherm **Heat flow** *(Heat conduction)* Differential	Decompositions, storage stability	0.6-25
DSC	Mettler-Toledo, Perkin-Elmer, Setaram	Isotherm, Isoperibolic, Temperature scanning **Heat-flow** *(Power compensation)* **or heat accumulation** Differential	Screening, decompositions	0.05-1
DRC	Setaram, Aventis	Isoperibolic **Heat accumulation** Differential	Reactions	100-500
RADEX, SEDEX, SIKAREX	Systag	Isoperibolic, Adiabatic **Heat accumulation**	Screening, decompositions, storage stability	1.5-3 2-100 5-50
ARC	Thermal Hazard Technology	Adiabatic **Heat accumulation** *(Power compensation)*	Decompositions	0.5-3
Dewar	Chilworth	Adiabatic **Heat accumulation** *(thermal isolation)*	Reactions, thermal stability	100-1000

The Setline 120 and the Calvet calorimeters are described in more detail since they have been used in this work. The Setline 120 calorimeter constitutes the basis of the microreactor-based calorimetric system developed in the frame of this work whereas the Calvet calorimeter has been used for reference measurements.

2.2.1.1 *The Setline 120 calorimeter*

The Setline 120 is a commercially available calorimetric system manufactured by Setaram (France). This compact and light system was originally developed as a portable thermal analyzer.

Figure 2-2 shows a lateral section of the calorimetric cavity.

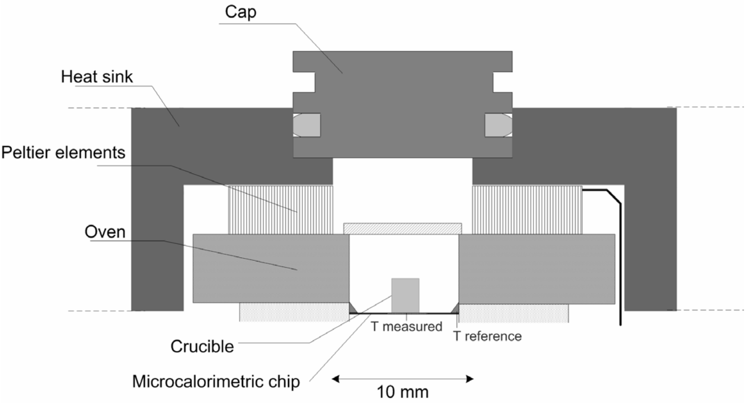

Figure 2-2: Scheme of the calorimetric system Setline 120.

The temperature of the calorimetric cavity is controlled by a Peltier element. Peltier elements are composed of different layers of composite ceramic-type materials. When an electrical current is passed through the Peltier junction, it results a thermoelectric cooling action known as the "Peltier effect", with one side of the element becoming cold and the opposite side becoming hot. When the oven cavity is cooled, the heat is removed by using the heat sink unit. The oven can also be used as heater by reversing the polarity of the power supply.

This calorimeter allows working at temperatures ranging from -10 °C to 120 °C without additional cooling system. The range of working temperatures is shifted to between -25 °C and 105 °C when the system is connected to a cool water circulation.

In the standard procedure, a crucible is introduced in the calorimetric cavity and centered above the microcalorimetric chip. As explained in chapter 1, in the novel microcalorimeter proposed in this work, the crucible is replaced by a microreactor. The heat released or consumed by the reaction is measured by a thermal sensor integrated in this microcalorimetric chip.

Let's describe the working principle of this chip.

Principles of the microcalorimetric chip

Basic principles **[18].** The heat flow of a chemical reaction is measured by converting it into a temperature difference across a structure of known thermal resistance ($\dot{q}_{rx} = \Delta T / R_{th}$).

This temperature difference is translated into an output voltage U by a thermopile ($U = \Delta T \cdot N_{th} \cdot \alpha_{th}$, with $N_{th} \cdot \alpha_{th}$ in $V \cdot K^{-1}$, α_{th} being the Seebeck coefficient of a chosen thermocouple and N_{th} the number of thermocouples).

A calibration is required to convert the output voltage of the thermopile U [V] into a heat flow [W]. This is obtained by applying a Joule effect pulse of 1 mW during a fixed time (typically 60 s) with a small heater resistance integrated in the calorimetric chip. The comparison of this applied signal with the output voltage recorded allows the determination of the sensitivity S of the chip [$\mu V \cdot mW^{-1}$].

This calibration is presented in more detail in chapter 5.

Structure of the chip **[18, 19].** The chip used is the LCM 2524 from Xensor Integration (XI, Netherland). The membrane of this chip is a 8.5 mm × 8.5 mm large mono-crystalline silicon layer with a thickness of 45 μm fixed to a thick silicon rim (see Figure 2-3).

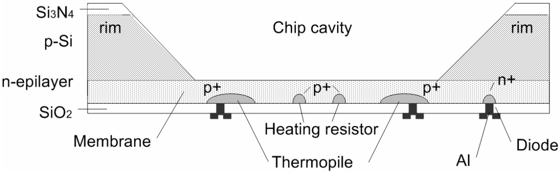

Figure 2-3: The chip LCM 2524 from Xensor Integration (XI).

The center of the membrane is the sensitive area and contains a heater resistance. Between the heater and the rim, a silicon-aluminum thermopile is integrated to measure the temperature increase of the sensitive center with respect to the rim. The rim serves as a mechanical suspension and as a thermal reference. The sensor's sensitivity can be calibrated using the heater as explained above. An integrated diode temperature sensor added on the non-sensitive part of the sensor allows monitoring the ambient temperature. The sensitive part of the membrane has an area of 4 mm × 4 mm.

This sensor chip is encapsulated in a standard ceramic chip carrier (Pid-Grid Array, PGA).

2.2.1.2 The Calvet calorimeter BT 2.15

As the Setline 120, the Calvet microcalorimeter BT 2.15 is manufactured by Setaram. This "low temperature-type" system has temperature limits of -196 to 200 °C. This microcalorimeter can be used for the measurement of different thermal properties. It provides one of the most sensitive methods to measure reaction enthalpies, heats of mixing and phase change enthalpies. It can also be used to characterize reaction kinetics.

The system consists of a thermostatic block with two cavities where reference and reaction cells are located (see Figure 2-4). The temperature of the system can be controlled by means of two elements: an electric heating unit surrounds the cylindrical cavity containing the experimental cells and an external jacket allows the introduction of liquid nitrogen. It can operate in either quasi-isothermal or slow-scanning temperature mode (maximum ca. 2 °C·min^{-1}).

Two symmetrical heat flow detectors are arranged around the measurement cells. These detectors are made of thermocouples connected in series and they thermally connect the cells to the calorimetric block. They deliver an electrical signal proportional to the heat exchange distributed between the cells and the block.

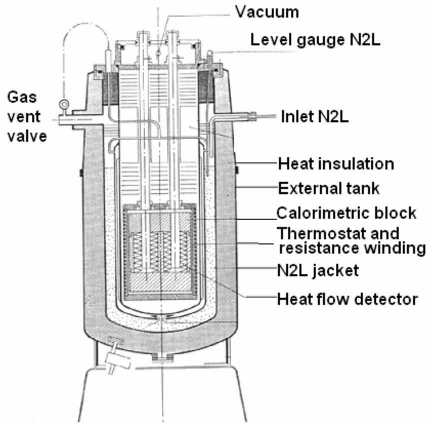

Figure 2-4: Scheme of the Calvet microcalorimeter BT 2.15 [20].

Suitable measurement cells are available for different types of applications.

Additional details about the operating conditions of this system for our particular application are given in chapter 6.

Deconvolution technique

When the time constant of a measurement system is long compared to the time of the reaction investigated, the measurement signal has to be deconvoluted i.e. the dynamics of the equipment have to be separated from the one of the studied system. This is the major disadvantage of the Calvet calorimeter since it is an instrument with a relatively long time constant.

Various methods have been reported and will not be developed in this work. The Differentiation method (numerical inverse filters) [21, 22] and the Fourier transform analysis [21-24] are the most frequently used techniques. A simplified differentiation method is used in the present work.

2.2.2 Reaction calorimetry, characterization of fast and exothermal reactions

As explained above, the determination of the kinetic parameters of a reaction is best performed under isothermal (and isobaric) conditions.

One practical difficulty for the determination of reaction kinetics is to ensure that the thermal equilibrium of the calorimeter is reached as the reaction starts. The second reactant should therefore only be introduced once equilibrium is achieved. This can be done by three different ways. In a RC1 calorimeter, the second reactant can either be added at the beginning (batch calorimeter) or be **pumped into the vessel** (semi-batch reactor) and mixed using an efficient stirrer. Corrections to the signal are needed if the entering fluid has a different temperature from the measuring vessel. A second method involves introducing the second reactant by **piercing or pushing a membrane into the vessel**. This method is for example used in the Calvet calorimeter. In this case, the temperature of both reactants is already thermally equilibrated as the reaction begins. However, since there is no stirrer, the mixing achieved in these vessels is poor and may be limiting for rapid reactions. The third method is to use **flow-through calorimetry** (see §2.3).

These difficulties are even further increased for the characterization of the kinetics of fast exothermal reactions. In this case, both the control of the temperature and a sufficiently rapid mixing are difficult to achieve in the classical systems described above. Moreover, when the reaction time is shorter than the time constant of the system, mathematical tools are needed to deconvolute the curve (as explained for the Calvet calorimeter) and this may reduce the precision of the results.

A novel small reaction calorimetric device has recently been developed at the ETH of Zurich to solve this problem [25]. This device combines the Power-Compensation principle with heat-conduction (heat-flow balance) and allows on-line measurement of the conversion by IR-ATR spectroscopy. The vessel has a volume of 25 to 45 ml. As for the RC1, the geometry of the reaction vessel is similar to an industrial reactor and thus allows investigating industrial problems such as the simulation of industrial mixing conditions or the estimation of heat transfer in a reactor. This gives useful data for the scale up of a process. One drawback is that strictly isothermal conditions are difficult to achieve, when working with highly exothermal reactions.

As briefly mentioned above, an interesting approach for studying reaction kinetics is to use flow-through calorimetry. The next section proposes a more detailed description of a selection of flow-through calorimeters.

2.3 DEVELOPMENTS IN FLOW-THROUGH MICROCALORIMETRIC SYSTEMS

None of the classical techniques described above used flow-through calorimetric cells. Indeed, these techniques create some difficulties. The residence time of the reactants in the reactor is fixed by the working range of flow rates and the size of the vessel. Therefore all types of reactions cannot be studied in the same system. The calorimeter is then often limited to a particular type of application. Moreover, large amounts of chemicals are needed, when working with large-sized reactors.

As the novel system developed in our laboratory is a flow-through microcalorimetric system, we will focus this overview on flow-through systems and describe some interesting examples of existing systems.

2.3.1 Developments in the late sixties

In the late sixties, most of the research involving microcalorimetric measurements was carried out with cell-type instruments. However some developments in the domain of flow-through microcalorimeters were performed to avoid the disadvantages related to the use of cell-type instruments. This technique allows for example to eliminate the time consuming cell-filling step, reduces the time required for thermal equilibrium and eliminates the thermal effects linked with the mixing operation in cell-type instruments (wall puncturing, mercury seal displacement…).

The main purpose of these developments was to obtain the high sensitivity and high accuracy required for the measurement of weak thermal signals (heat of dilution, weak complexes…).

In the next subsections, the three main microcalorimeters existing in the late sixties are described. These systems show similar sensitivity and accuracy, but differ significantly in their principles and characteristics. The subsequent developments of these flow microcalorimeters are also briefly discussed.

2.3.1.1 *Stoesser Flow Microcalorimeter*

The Stoesser Flow Microcalorimeter was developed to study weak complexes [26]. It was one of the first flow microcalorimeter (excepting titration calorimeters).

The main arrangement of the Stoesser twin calorimeter cells is shown in Figure 2-5.

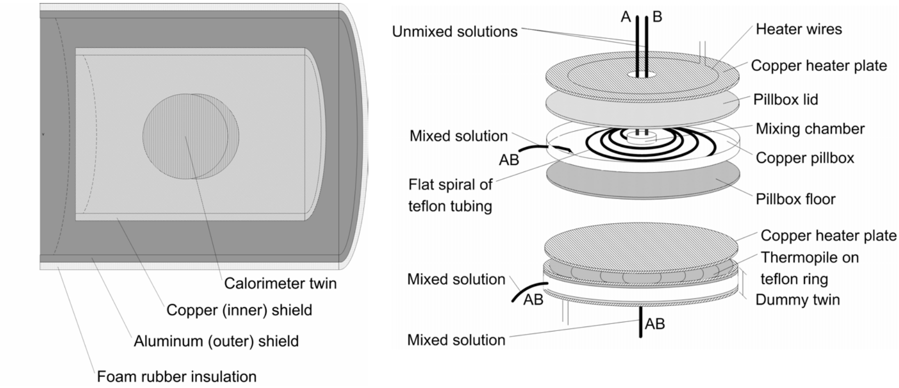

a) b)

Figure 2-5: Arrangement of the Stoesser twin calorimeter cells a) thermal shields around the twin calorimeter cells, b) twin calorimeter cells.

The well-controlled thermal shields (see Figure 2-5a) are used both to precisely preheat the solutions and to provide an adequate thermal insulation of the twin calorimeter elements.

The reagents are brought into contact in the mixing chamber (ID=0.5 mm) of the first twin cell and flow through the equilibration region of this twin (ID=0.965 mm). Then, the mixed solution flows back to the inner shield and is introduced in the dummy twin. In this system, the temperature difference between these two nearly identical calorimeter twins is kept close to zero by a suitable electrical power input.

This design was used later by other authors e.g. for the characterization of dilute polymer solutions [27]. In 1974, S. J. Gill working with Wadsö et al (see next paragraph) developed a novel flow calorimetric technique for the determination of enthalpies of dissolution of poorly soluble liquids [28].

2.3.1.2 Monk-Wadsö Flow Microcalorimeter (LKB microcalorimeter)

A general description of this apparatus is given in Figure 2-6 [29, 30].

The reactants are introduced in the microcalorimeter in two separate streams. They are first preheated by passing through the gold tubes of the heat exchange unit. The liquids are then brought together in a mixing zone of the flow cell. The flow cell is in good thermal contact with the thermocouple plates positioned on either side.

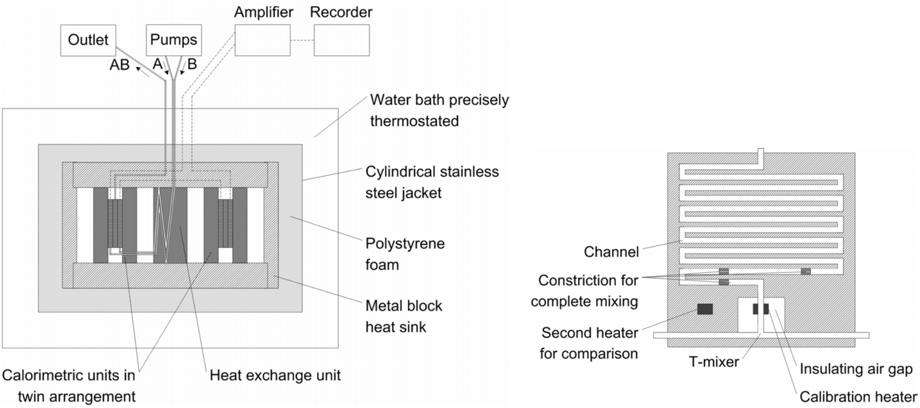

a) **b)**

Figure 2-6: Arrangement of the Monk Flow Microcalorimeter (a) with a focus on the flow cell (b).

Several flow cells with different designs have been tested. The cell shown in Figure 2-6b has been proposed for fast reactions. Between the plate and the lid, a thin gold foil is positioned acting as a gasket. All surfaces in contact with the calorimetric liquid are gold plated.

The reaction channel has a width of 1.5 mm and a depth of 1.5 mm. Three constrictions (0.2 mm) in the channel ensure complete mixing of the reactants.

A 30 Ω calibration heater, insulated from the body of the cell by an air gap, is located between the T-junction and the channel. The calibration heat is thus taken up by the liquid flow and measured in a similar way as for the heat of reaction.

As explained by Kemp et al. [31], this flow-through system was commercialized as the LKB microcalorimeter and was for a long time the most attractive type of calorimeter for biologists, especially for those working with microorganisms. Only recently the Thermal Activity Monitor (TAM, from Thermometric) with its effective stirring and with micro-electrodes directly in the calorimetric vessel opened a true competition for investigations of cellular systems.

In 1982, strengthened by the success of their first flow-through calorimeter, Wadsö and Suurkuusk developed a new type of system, the LKB BioActivity Monitor sold by Thermometric. This microcalorimeter is modular and allows to work either in a batch mode or in a flow mode.

2.3.1.3 Picker Flow Microcalorimeter

The Picker flow microcalorimeter has a response time significantly shorter than the other flow microcalorimeters presented above. This small time of equilibration allows to vary the composition of the mixing fluids or their volume ratio during one experiment and to obtain for example curves of enthalpy of mixing as a function of the volume fraction of the two solutions in less than 1 hour.

Figure 2-7 shows the general principle of this differential flow calorimeter [32].

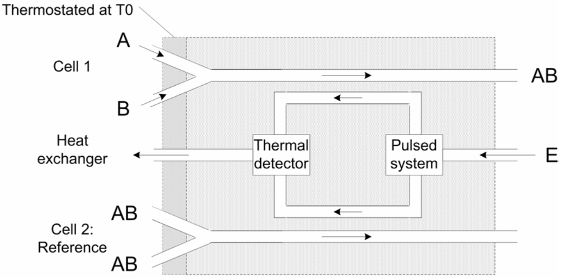

Figure 2-7: Schematic diagram of the Picker Flow Microcalorimeter.

The reactants are thermostated at T_0 and introduced at a constant flow rate in cell 1. The heat released in this cell is exchanged with a counter-current heat exchanger. Most thermal effects not related to the mixing of A and B will be cancelled by the duplicate system (cell 2) in which the mixture AB is introduced.

The system can be made quasi-adiabatic or quasi-isothermal depending on the relative flow rates of the reaction medium and exchanger fluid.

A patent has been filed on this system in 1973 [33]. This flow microcalorimeter has been commercialized by Setaram and is still used world-wide mainly for the determination of heat capacities of substances or mixtures.

In 1980, Roux et al [34] investigated the conditions under which this microcalorimeter could be used to measure reaction enthalpies and reaction rates. The model reaction used for validation was an ester hydrolysis in an alkaline medium. The same model reaction was chosen in the present work.

2.3.2 Recent developments in flow-through microcalorimeters

More recently, new types of flow-through microcalorimeters have been developed based on integrated circuit technology. In these novel devices, a twin system is not anymore necessary for the compensation of parasitic heat flow since the heat capacity of the inertia is very small.

Some of the most interesting devices are shown in this subsection; firstly devices constructed using an integrated circuit similar to the one used in the Setline 120 and then a device using another hand-made circuit.

2.3.2.1 Using an integrated silicon thermopile chip manufactured by Xensor Integration

These devices use the microcalorimetric chip LCM 2524 presented in §2.2.1.1.

Different constructions of integrated-circuit (IC) calorimeters have been realized. Both batch and flow-through calorimeters operating in isoperibolic or temperature scanning mode have been described [19]. We will focus this review on flow-through calorimeters only. Figure 2-8 shows three flow-through devices developed by Lerchner et al. [19, 35].

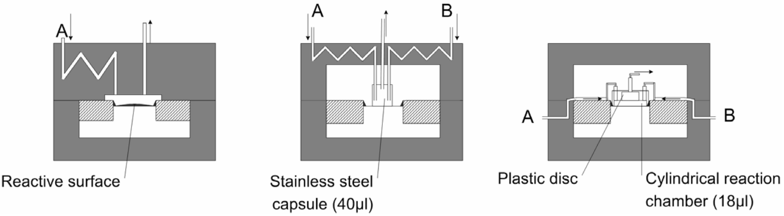

Figure 2-8: Schematic view of different constructions of IC calorimeters.

The first device presented in Figure 2-8 is used for the study of solid-gas interactions and to monitor the heat production of enzyme-catalyzed reactions. The two other devices are used for mixing and reaction measurements. The second device consists of a 40 µl stainless steel capsule glue-bonded on the sensitive area of the silicon membrane. In the third layout, the stainless steel capsule is replaced by a 2 mm thick plastic disk containing a 18 µl cylindrical reaction chamber

The main advantages of these systems compared to classical calorimeters is the small heat capacity of the sample holding and a very small time constant for the heat exchange between the sample and the heat sink.

These microsystems are mainly used to measure low thermal signals. Special developments have been made to increase the accuracy and reduce the systematic error due to external variations [36].

2.3.2.2 Using a BiSb/Sb-thermocouples

This flow-through microcalorimeter constructed by Köhler et al [37] is shown in Figure 2-9. This system is made of two sealed planar chips: a silicon chip with a 0.8 µm membrane containing the thermopile and the heater and a 0.5 mm thick glass chip with etched Y-shaped channels glue-bonded to the silicon chip [35], [37]. The attached glass chip ensures only small heat losses due to its low heat conductivity.

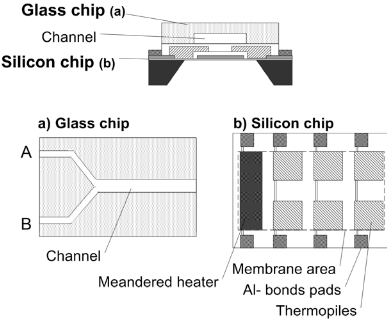

Figure 2-9: Chip reactor for microfluidic calorimetry designed by Köhler et al [37].

The size of the reaction channel is 2 mm wide, 0.1 mm deep and 12.6 mm long. The layout of this system allows to pass a continuous flow of one of the reactants and to introduce a precise amount of the second reactant in a solvent stream. The thermoelectrical response of the thermopile to this pulse is recorded and integrated.

2.3.3 Summary

The main objective for the construction of the microcalorimeters described above was to reach the high accuracy and the high sensitivity required for the study of weak thermal signals. The main applications of these calorimeters are for biological reactions, enzyme-catalyzed reactions or determinations of heats of dilution. The mixing time of the reactants and the type of material used were therefore not of particular importance for the designing of these microcalorimeters. Fast and exothermal reactions cannot be studied in those devices.

All these systems made use of small reaction channels. However the dimensions of the latter were still in the millimeter and not in the micron range. The advantages of using small microchannels are discussed in the next section.

2.4 ADVANTAGES OF USING MICROREACTORS

Microreactors are defined as miniaturized systems fabricated by using, at least partially, methods of microtechnology and precision engineering. The decrease of the physical size (linear dimension and volume) and the increase of the surface to volume ratio lead to several outstanding properties. These are briefly described in this paragraph.

Microreactors essentially find applications in three fields [38]:

- For the safe production of hazardous compounds (e.g. in microstructured reactors).
- For increasing the selectivity of a reaction. The high surface/volume ratio allows a fast interruption of processes, which reduces the contribution of secondary reactions. Moreover, for multiphase reactions, the mass transfer path is minimal and this may also result in a higher selectivity [39].
- For testing chemical and biological probes in mass-screening and combinatorial chemistry [40]. Immunological and biochemical assays such as DNA capture and ELISA (Enzyme-Linked Immunosorption Assay) can also be performed.

Let's focus more on applications in safety. Several examples of processing in microreactors clearly demonstrated safe operation using process parameters of otherwise explosive regimes [39, 41]. This has been done, for example, with the hydrogen/oxygen reaction [42], [6].

Indeed, the decrease in physical size greatly improves safety-related issues:

- The high surface to volume ratio improves the response time that leads to efficient heat transfer and increases the controllability of the process.
- The small size of the microchannels translates into smaller amounts of dangerous chemicals. According to the intensification principle in inherent process safety, in case of incident, only a small amount of material is released in the environment.
- The microstructured features result in reactor dimensions that are less than the quench distances for explosions.
- Microreactors can be designed to provide rapid mixing in the micron-sized channels, an additional advantage when enhanced process control and fast response times are required [43].

For the calorimetric characterization of fast and exothermal reactions, the use of microreactors allows to maintain strict isothermal conditions and thus to avoid thermal explosions.

Various techniques of construction of microreactors are described in chapter 3. Examples of micromixers developed to increase the mixing rate are presented in chapter 7.

2.5 ORGANIZATION OF THE THESIS

Even if many calorimeters have been developed during the last century to fulfill the requirements of numerous specific applications, the characterization of fast exothermal reactions still remains a difficult challenge in classical systems.

The developments reported recently in the field of flow-through microcalorimeters have been mainly applied to biological systems or to the measurement of small heat flows. However, these calorimeters made of small reaction microchannels show a high surface/volume ratio and could allow the establishment of isothermal conditions even for high heat flows.
The combination of microreactors with microcalorimeters should offer new possibilities for the isothermal characterization of highly exothermal reactions. This is the subject of the present work.

The thesis is organized as follows: The first step of this work is the construction of the microreactor. A technique providing a microreactor resistant to corrosion and that fits easily in the small cavity of a commercially available calorimeter is reported (Chapter 3).
This microreactor should provide a rapid mixing to allow the investigation of fast reactions. Therefore the second step of the work is the assessment of the degree of mixing achieved at the end of the reaction channel. This is discussed in Chapter 4.
The microreactor is then inserted in the calorimetric cavity of a commercially available calorimeter. The resulting microsystem is calibrated and the thermal efficiency of the system optimized. The preheating of the entering fluids is also ensured (Chapter 5).
After improvement of the quality of the thermal signal, the determination of the kinetics of a simple model reaction is used to validate the results obtained. Reactions involving high heat flows are then investigated (Chapter 6).
The conclusions are summarized in Chapter 7.

Chapter 3

CONSTRUCTION OF THE MICROCHANNELS AND THE MICROREACTOR

3.1 INTRODUCTION

During the last decades, extensive progress has been achieved in microreactor technology and this novel concept has been introduced in chemistry, molecular biology and pharmaceutical chemistry. Many different advanced micro-engineering techniques have been proposed to produce a broad variety of microreactors adapted to specific needs.

The first step of the construction of the novel microreactor-based calorimetric system is to select a precise, inexpensive and flexible method for the machining of the reaction microchannel. Since these microreactors are intended to be introduced into commercially available calorimetric systems, many geometric restrictions have to be taken into account for the construction.

The initial concept was to proceed in two steps and to build two different devices. The first one would be exclusively used for the characterization of the mixing in the reaction channel (cold mockup) and the second device would allow the calorimetric measurements.

After a brief overview of the standard techniques reported in the literature, two different approaches for constructing the microchannels are investigated. The second method shows significantly better results than the first one and was selected for the rest of the project.

3.2 STANDARD TECHNIQUES FOR MICROCHANNEL CONSTRUCTION

Many different techniques have been used to microstructure workpieces [44],[45]. Let's make a short overview of the most common methods reported in the literature.

Table 3-1: Overview of some standard techniques used for microchannels construction

Methods	Materials	Principles	Ref.
Anisotropic wet chemical etching	Single crystalline silicon Glass (FOTURAN)	Simple structures are generated by lithography using patterned etch stop layers. *Example for FOTURAN:* - Exposure to UV light and subsequent heat treatment leads to partial glass crystallization. - Crystalline phase (Li_2SiO_3) is more soluble in hydrofluoric acid than the surrounding unexposed amorphous glass.	[44] [45] [46]
Dry etching	Not limited to single crystalline material	Low-pressure plasma or ion beam generated in high vacuum are used for the anisotropic removal of material.	[44] [45]
Various process using Laser-assisted Polymerization	Polymers	Irradiated liquid monomer polymerizes by a chain reaction into a solid polymer. Non-irradiated liquid dissolves during rinsing.	[47] [48]
LIGA process	Metal, Polymers, Ceramics and even Glasses	- A 3-D structure is generated by lithography process. - A complementary metal device is generated by electroforming. - The metal device serves as a mould insert for subsequent replication process.	[49]
Electro Discharge machining	Conductive materials (independent on their mechanical properties)	- A switching DC voltage supply is applied to the tool electrode and the workpiece. - The plasma generated and the very high local temperature melt and vaporize the workpiece.	[50] [51]
Advanced mechanical processes based on precision engineering	Metal, Polymers	For batch processes possessing a number of restrictions due to the peculiarities of their implementation.	[52]

General remarks

Most of these techniques are however expensive and not available in the micro-engineering department of the Swiss Federal Institute of Technology in Lausanne (EPFL).
As the layout of the microreactor needed is simple, methods existing in the micro-engineering department are tested. These methods are described in the next sections.

3.3 SPARK-ASSISTED CHEMICAL ENGRAVING OF GLASS

In the early stage of this project, the construction of the microreactor was planned to result from collaboration with the “Laboratoire des systèmes robotiques” (LSR, Institute of Production and Robotics, EPFL). The LSR was working on the development of a prototype for glass engraving and gave us the opportunity to use it. This interdepartmental project constituted a nice application for their prototype and provided an innovative way of constructing a microchannel in a glass layer at low cost.

Unfortunately this approach did not fulfill our requirements and was finally abandoned. The reasons are discussed below.

3.3.1 Advantages of the technique

Glass is an interesting material for the construction of microchannels. Its chemical inertia allows performing various types of corrosive reactions and its transparency facilitates the understanding of the flow behavior. The concept is to seal the glass to a conductive layer that guides the heat flow released in the channel to the thermal sensor at the bottom of calorimetric cavity. The low thermal conductivity of glass limits heat losses on the opposite side.

3.3.2 Principles of the technique

The construction of small microchannels using Spark-assisted chemical engraving requires first to machine small microtools. The width of the microchannel engraved in the glass layer is then directly related to the size of the microtool used.
The microtools were obtained by Wire Electro discharge grinding (WEDG). This technique is part of the Electro discharge machining processes mentioned in Table 3-1 in the section §3.2.

Construction of microtools by Wire Electrodischarge Grinding (WEDG)

This method allows the construction of microtools with diameters down to 20 microns.

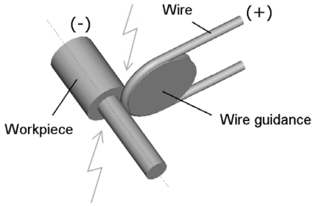

Figure 3-1: Scheme of the principle of the WEDG technique.

A pulsed voltage is applied between the rotating workpiece (microtool) and the wire. Sparks are then generated and induce the removal of material from the workpiece. The workpiece was, in our case, made of stainless steel. This technique was first proposed by Masuzawa et al. [53] and is now commonly used [54] [55].

Spark-assisted chemical engraving of glass

As shown in Figure 3-2, the glass layer is dipped into an electrolyte solution (NaOH 30 % wt) while a constant voltage (25-30 V) is applied between the microtool-cathode (Stainless steel | H_2 | H^+) and the anode (Stainless steel | OH^- | O_2).

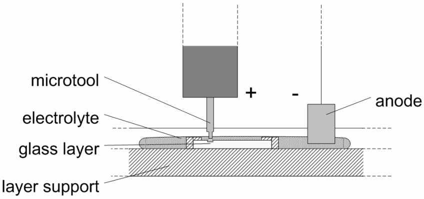

Figure 3-2: Layout for the spark assisted chemical etching.

Electrolysis takes place at the cathode (H_2 generation) and, through the gas film, sparks are generated, which attack the glass. In this process, a combination of thermal (sparking) and chemical (glass etching) phenomena are induced.

These phenomena were studied in more detail in several recent publications of the LSR ("Laboratoire des systèmes robotiques", Institute of Production and Robotics, EPFL) [56-58].

3.3.3 Resulting microchannels

Microtools created using WEDG

This technique was well implemented and allows a reproducible machining of microtools. The diameter of the rod was determined by scanning electron microscopy (SEM). Examples of machined tools are shown in Figure 3-3.

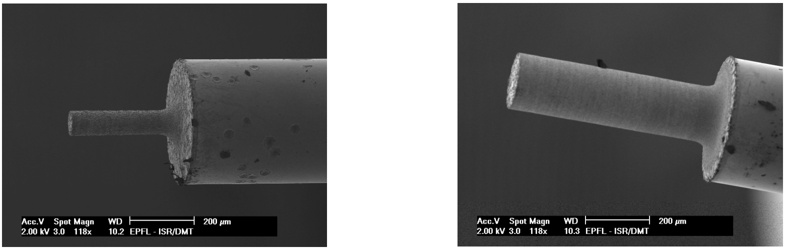

a) **b)**

Figure 3-3: SEM Pictures of microtools. The diameters of the rods are respectively 80 µm (a) and 180 µm (b).

The rods obtained were very fragile and should be manipulated with great care.

Engraving of the microchannels

This technique wasn't yet fully implemented and was still under development at the LSR.

For the first microreactors, the tool used to machine microchannels was positioned manually and many alignment problems were experienced (see Figure 3-4).

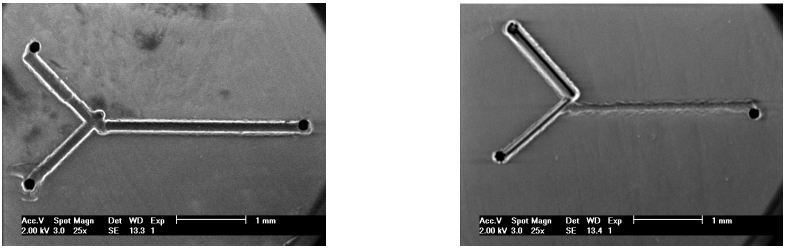

Figure 3-4: Examples of misfired microreactors obtained with manual positioning of the microtool.

This issue was solved by using a newly developed prototype on which tool displacements were controlled by computer (Figure 3-5). The major difficulties encountered then were the ability of creating holes through the entire layer without breaking the glass and the adjustment of the quantity of electrolyte to guaranty a good surface quality of the channel.

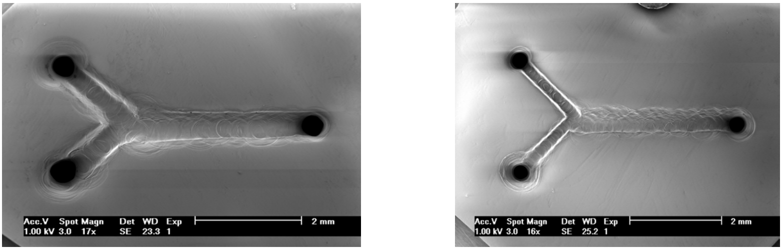

Figure 3-5: Examples of microreactors obtained with a computer-controlled microtool.

The depth of the microchannel was controlled electronically. The width of the channel could not be precisely predicted and was determined at the end of the machining on the basis of scanning electron microscope pictures (like those presented in Figure 3-5). The entire process of engraving including the preparation of the prototype was very time-consuming (about half-day of work in the absence of any technical problem).

The construction of more complicated designs was also investigated (see Figure 3-6). Obtaining such designs took several hours and it was never possible to guarantee that no technical problems occurred during that time. The amount of electrolyte had to be constantly checked. The glass layer had to be precisely and firmly fixed. Any slight deviation from the protocol during the time of engraving rendered the microchannel unusable.

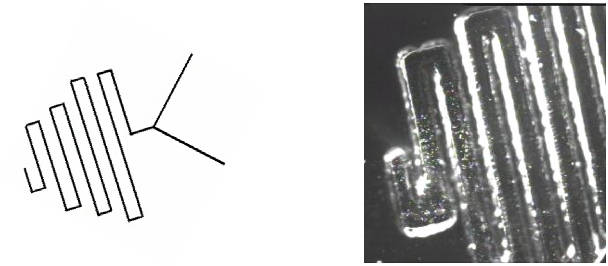

a) **b)**

Figure 3-6: Machining of a bended microchannel, a) scheme of the design b) picture of a microchannel engraved (before piercing the holes).

Such complicated microchannels could not be obtained without breaking the glass layer at the end of the machining. At this state of development of the prototype, only simple microchannels could be engraved.

3.3.4 The microchannel lid

Investigations about the choice of the lid were then carried out. Let's first take into consideration some of the requirements of this layer.

Firstly, as this layer is intended to be in direct contact with the measurement membrane of the calorimeter, the lid should ensure the conduction of the heat released in the channels toward the sensor. This layer should thus have a good thermal conductivity.

Secondly, the dilatation coefficient of the lid with temperature should be close to the one of glass to avoid the destruction of the weakened engraved glass layer during sealing.

Moreover the sealing of the two layers should be perfectly hermetic to avoid leakage that would give a wrong estimate of the flow rate in the microchannel. As the engraving is a very time-consuming step, the quality of the sealing should also be very reproducible to avoid the loss of an engraved glass layer.

Tests were performed with different layers and the best results were obtained with a silicon layer.

Silicon can easily be bound to the glass layer by anodic bonding. This well-known technique was frequently used in the group of "Advanced silicon microsystem" of the Microsystems laboratory (LMIS4, Institute of Microelectronics and Microsystems, EPFL).

The glass and silicon wafers are brought into contact and heated at 300-400 °C while a voltage of approximately 200-1000 V is applied.

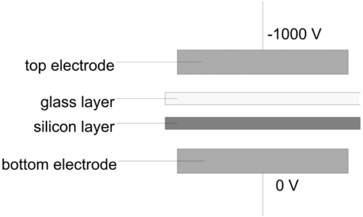

Figure 3-7: Layout of the anodic bonding.

As shown in Figure 3-7, a high negative potential is applied to the glass to attract the positive ions (Na^+) to the negative electrode, where they are neutralized. Such a removal permits the formation of a space charge at the glass-silicon interface, which creates a strong electrostatic attraction between the silicon and the glass wafers that holds both pieces firmly in place. A chemical bond is presumed to occur that fuses the wafers together.

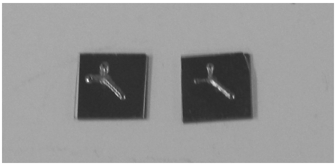

Figure 3-8: Picture of microreactors of glass sealed to a silicon layer.

The main disadvantage of using this technique is that the silicon layer is easily attacked by alkaline solutions. This significantly restricts the type of reactions that can be carried out in the microreactor.

Once the microreactor was assembled, the issue of the tube fixation was investigated.

3.3.5 Fixation of the inlet and outlet tubes

A device was first constructed for flow visualization. This housing made of Plexiglas was machined following the representation shown in Figure 3-9. It was closed by longitudinal screws. The reactions performed in this first device were non corrosive.

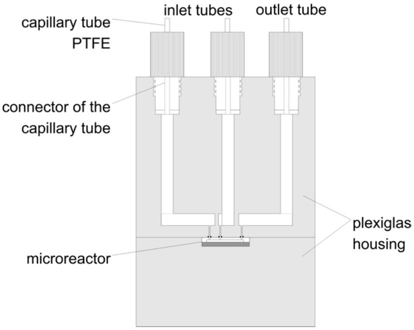

Figure 3-9: Plexiglas housing for flow visualization in the microreactor constructed by spark-assisted chemical engraving.

This device allowed to assess the degree of mixing achieved in the microchannel and to check the hermetic sealing obtained by anodic bonding.

However, this device could not be inserted in the calorimetric cavity due to geometric restrictions of the commercial calorimeter and to heat transfer issues. Moreover, the use of Plexiglas was obviously not appropriate when corrosive media were used.

Glue could theoretically be used to directly fix the tubes to the holes but as the inlet and outlet holes were in the glass layer of the microreactor, this would have required new testing. This tubing issue emphasized the existing limit of this way of constructing microreactors.

3.3.6 Limits of the use of spark-assisted chemical engraving for the construction of microreactors

As this method was still under development, major problems were faced.

As already mentioned the channel engraving in the glass layer was very time-consuming. The precision and repeatability of the engraving were low: many parameters were involved in the machining (voltage, electrolyte quantity, tool shape, plate fixation...) and the exact removal rate was not precisely known. Numerous plates were broken before the end of the channel engraving, mainly during the machining of the holes. A deviation from the desired diameter by 20µm was often observed. The same problem occurred with regard to the channel depth.

Moreover, the designs of the microchannels were limited by the programmable moves of the tool. For example, curves were not possible. The programming became also very complicated for designs different from a simple Y.

In addition even if anodic bonding of a silicon layer appeared to be an efficient technique to hermetically close the microreactor, the high reactivity of silicon greatly limited the type of reaction that could be studied in the channels.

Finally, with the techniques available in the laboratory, the construction of an appropriate device for calorimetric measurement was an almost insurmountable challenge.

In conclusion, a long and extensive development effort would be required to render this approach suitable for our specific application. A more conventional and well-known technique was therefore preferred.

3.4 SILK-SCREEN PRINTING OF A THICK FILM DIELECTRIC

Microreactors obtained by silk-screen printing were machined by the Laboratory of microtechnical production (LPM, Institute of Production and Robotics, EPFL). All experiments that are presented in the rest of this document have been carried out with this type of microreactors.

3.4.1 Advantages of the technique

This well-implemented technique can guarantee a good precision and reproducibility in the microchannel size. No further developments are needed for the construction of the microchannel. Moreover, a large number of microreactors can be produced in short time (100 microreactors on each substrate). The base and the lid of the microreactor are made of alumina (Al_2O_3) which presents a satisfactory chemical inertia and has a good thermal conductivity (25 $W \cdot m^{-1} \cdot K^{-1}$). The observation of the flow behavior is in this case performed with a special microreactor built above a glass layer but having the same design as the standard ones.

3.4.2 Principles of the technique

Detailed information about this technique can be found in [59, 60].

The first step of this technique is the preparation of the silk screen. This screen will subsequently be used to deposit a paste (dielectric) above the substrate. Once fired, this paste forms the walls of the microchannels.

The technique used for the screen preparation has similarities with the wet chemical etching and the laser-assisted polymerization processes described in section §3.2.
The screen is a weft covered by an emulsion of UV-sensible monomers (around 30 μm). The "negative" of the wished designs is deposited above the screen and exposed to UV radiation. Under the action of light, the monomer polymerizes and the emulsion solidifies. In the black part of the negative, the monomer is protected from light and remains liquid. It can be washed away with water. The meshes of the weft are in this way open in the corresponding black parts of the negative and closed in the white parts.

These steps are illustrated in Figure 3-10.

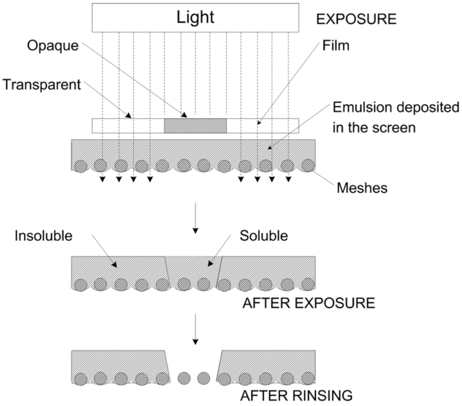

Figure 3-10: Preparation of the screen.

The screen is then fixed in a frame and machining begins (Figure 3-11).
The paste is put down on the silk-screen printing support. Under the action of the scraper and because of its flexibility, the screen reaches the substrate which is 0.5-1.0 mm apart.
The scraper traverses right through the screen forcing the paste to pass through the open meshes. The size of the meshes (characterized by the number of meshes of the screen) determines the precision of the paste deposition.

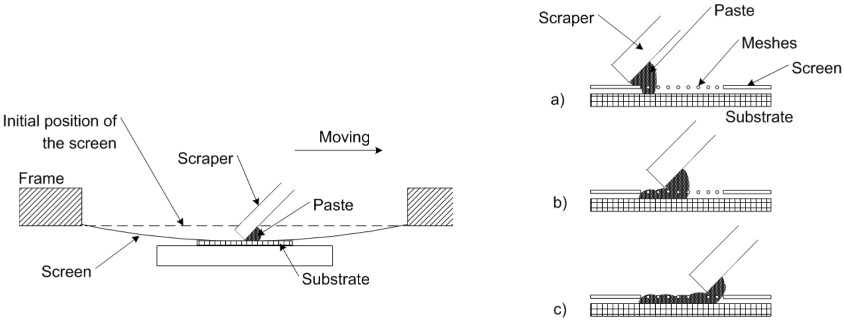

Figure 3-11: Silk-screen printing. a), b) and c) illustrate the movement of the scraper above the screen.

The paste is then dried and fired using a thermal cycle.

The paste layer has then a height close to 25 µm. The operation can be repeated to increase the wall depth to the desired value.

3.4.3 Construction of the first microreactors

As shown in Figure 3-12, different shapes were constructed varying the length of the reaction channel and the angle of contact of both reactants (T-mixer and V-mixer). The inlet and outlet positions remained constant. As these microreactors were intended to be introduced in a commercially available calorimeter (see chapter 5), the geometry had to be precisely studied. One of the restrictions was that the size of the plate containing the microchannels shouldn't exceed 8.2 mm ×8.2 mm.

The channel was 250 μm broad and its depth was 100 μm. The most frequently used design in the experimental part was the design 3 (see Figure 3-12). The other designs were built to test the influence of the channel shape on the mixing or used for special applications only.

The black parts indicate the location and the shape of walls.

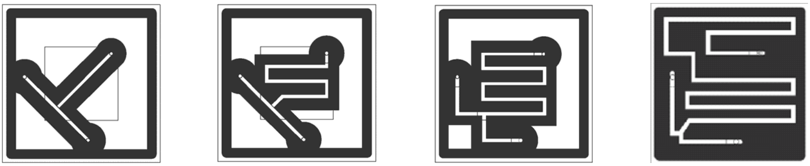

Design 1	**Design 2**	**Design 3**	**Design 4**
d = 0.25 mm	d = 0.25 mm	d = 0.25 mm	d = 0.25 mm
L = 2.85 mm	L = 11.30 mm	L = 18.75 mm	L = 44.00 mm
e = 0.10 mm	e = 0.10 mm	e = 0. 10 mm	e = 0. 10 mm

Figure 3-12: Representation of the negatives of the four different designs[1]. Design 3 was the most frequently used in the experiments.

Alumina (Al_2O_3) plates used as supporting material had a thickness of 250 μm. The original dimensions of these alumina plates were around 10 cm × 10 cm. More than one hundred microchannels were thus built above each plate and then cut out at the desired size of 8.2 mm × 8.2 mm by laser. A typical plate is represented in Figure 3-13.

---

[1] The inner square indicates the corresponding position and the dimension of the thermal sensor on the calorimetric membrane which is intended to be in contact with the microreactor. However, as shown in chapter 5 the lateral position of the microchannel related to the thermal sensor does not interfere with the thermal signal. The design 4 is therefore also suitable.

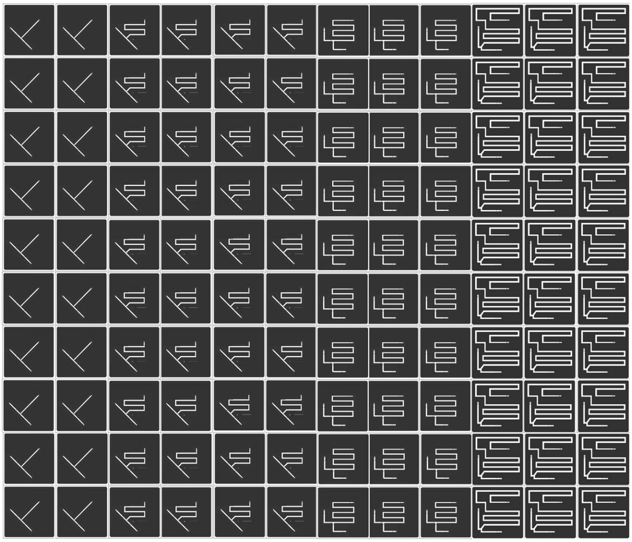

Figure 3-13: Typical representation of an entire alumina plate after silk-screen printing.

The screen used had 325 meshes and was covered with a 40 µm layer of emulsion (called 325/40).

The paste defining the channel walls was the dielectric ESL 4913. This paste was dried 15 min at 150 °C and then fired 30 min using a temperature profile with a maximum temperature of 850 °C.

Using the same silk-screen, a layer of around 20 µm of sealing glass (ESL 4026 AHV) was then deposited above the dielectric layer. This layer allowed the thermal sealing of the lid, another plate of alumina of 250 µm depth. This plate contained the holes required for the introduction of the inlet and outlet tubes (Figure 3-14).

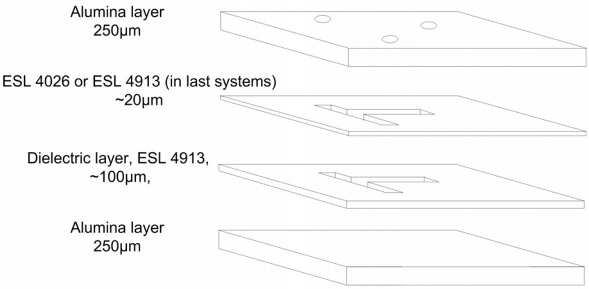

Figure 3-14: Representation of the different layer used for the construction of the microchannels.

To check the precision of the channel shape, lateral laser section of an assembled microchannel of design 4 were carried out and pictures were taken using a scanning electron microscope (SEM) (Figure 3-15). Areas of the channel section could thus be estimated after each bend along the same axis. Variations between these areas were about 2.5 % (within the precision limits of the measurement method).

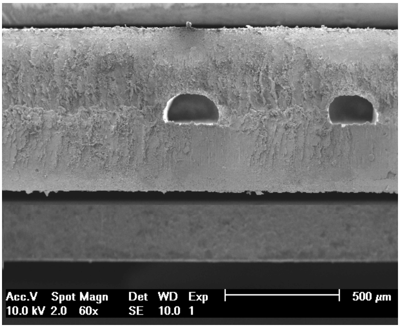

Figure 3-15: SEM Picture of a lateral section of the assembled microchannel.

Tube fixation. Stainless steel tubes (AISI 316L, ID=0.65 mm, OD=1.00 mm) were fixed in the lid by a slight internal application of glue (Cyanolyte loctite 401) and by an external application of an epoxy resin (Stycast 2651 MM, ABOVO). The latter polymerized two hours at 65 °C.

A plate (epoxy and glass fiber, 8.2×8.2×2.4 mm) was fixed 2 mm above the upper alumina layer to hold the tubes and avoid their lateral movements (Figure 3-16).

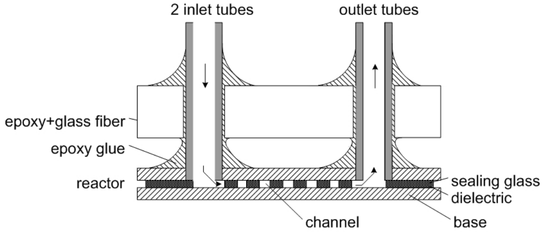

Figure 3-16: Scheme of the lateral view of the first microreactors assembled.

PTFE tubes (ID 0.97 OD 1/16”) were then directly fixed to the stainless tubes.

Flow rate Control. A syringe pump (Bioblock Scientific KDS 200, Ismatec, Switzerland) with two Hamilton glass syringes (1001 TLL, Hamilton, Verrerie de Carouge, Switzerland) was used for the control of liquid flow rates. Needles having an external diameter of 1 mm (Unimed, Switzerland) were inserted in the PFTE tubes and fixed to the Luer Lock hub of the syringes.

3.4.4 Problems of corrosion

During preliminary studies on the determination of reaction kinetics, the reactor was opened and corrosion of the sealing glass layer could be noticed. Corrosion tests were performed and it turned out that it was due to the acidic solutions. In contact with strong acids, some oxides such as PbO and B_2O_3 present in the glass structure are extracted and evacuated by the flow; the frame of the glass structure is destroyed leaving a residue of SiO_2 in powder form. This "free" SiO_2 falls then into the channel.

a) b)

Figure 3-17: Corrosion of the sealing glass with acidic solutions a) initial microchannel b) microchannel after two weeks of experimentation with an acidic solution.

Corrosion tests with aqueous solutions of H_2SO_4 1 $mol \cdot l^{-1}$ and NaOH 1 $mol \cdot l^{-1}$ were then performed with various other pastes. The dielectric ESL 4913 was finally chosen for its good chemical inertia and its vitreous property that permitted the sealing of the upper alumina layer. The ESL 4016 layer was thus replaced by an ESL 4913 layer.

The sealing layer of ESL 4913 was first fired at 700 °C and then sealed to the alumina layer at 1050 °C.

3.4.5 Construction of a special microreactor for the mixing visualization

For the construction of a microreactor allowing the mixing visualization, the base of alumina was replaced by a glass layer (Float glass, Schott Guichard SA) having a depth of 2 mm. The dielectric used for the construction of the previous channels cannot be used in this case because the temperature of 850 °C, needed to fire the paste of the channel wall, would melt the glass layer. The channels were therefore built using a vitreous paste (DP QQ600, Dupont) fired at 580 °C.

a) b)

Figure 3-18: Picture of the microreactor with a glass base a) top view, b) bottom view.

The paste deposition on this substrate was not as precise as on an alumina layer because the smooth surface of the glass provided a lower adherence of the paste to the base. However, this special microreactor allowed the visualization of the mixing by laser induced fluorescence. These experiments are described in chapter 4.

3.4.6 Evolution of the microreactor design

Some changes in the microreactor design had to be done to improve the sensitivity of the microcalorimetric system. Figure 3-19 shows several microreactors that were constructed. The purposes of these modifications as well as their respective influence on the heat flow signal are discussed extensively in Chapter 5.

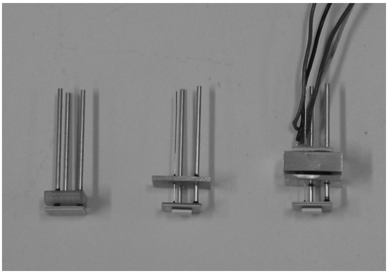

Figure 3-19: The three generations of microreactor design.

The construction of the first generation of microreactors is described in subsection §3.4.3.

All the modifications performed are illustrated in the scaled representation of the Figure 3-20 and are detailed in the next paragraph.

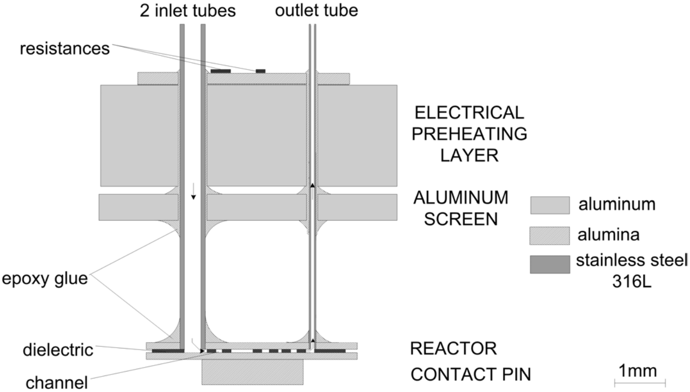

Figure 3-20: Scaled representation of the latest version of the microreactor.

Contact pin. A contact pin was introduced under the microchannel base to direct the heat flow released in the channel to the sensitive part of the microcalorimetric membrane. This contact pin was made of a square plate of alumina having a width of 4 mm and a thickness of 1 mm. It was fixed with a small amount of thermal conductive glue (Epotek H70S, Polyscience). The latter polymerized one hour at 100 °C.

Aluminum screen. An aluminum screen was then glued to the tube 6.0±0.05 mm above the bottom of the contact pin. The purpose of this screen was to fix the position of the microreactor in the calorimetric cavity. This screen prevents any mechanical force from the microreactor to the microcalorimetric chip and thus avoids the risks of damaging the fragile calorimetric membrane. This aluminum screen was made of a rectangular plate of 9.5 mm width, 12 mm length and 1 mm depth. The reproducible distance was achieved by using the support represented in Figure 3-21.

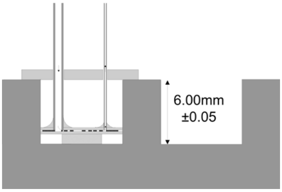

Figure 3-21: Support used for the reproducible positioning of the aluminum screen.

This screen was first fixed with a rapid glue (Cyanolyte loctite 401). Then a small amount of Epoxy resin (Stycast 2651MM, ABOVO) was then deposited around the tubes. This resin was polymerized at 65 °C during 2 hours. The previous plate (epoxy and glass fiber) was removed, its function being achieved by the aluminum screen.

Outlet tube. The internal diameter of the outlet tube was decreased from initially 0.65 mm to 0.12 mm to prevent the heat released after the reaction channel from interfering with the measurements. This effect was observed during kinetics determinations and is discussed in more detail in chapter 6.

A small washer was added at the bottom of the tube to better fix it in the hole. The rest of the standard procedure for the tube fixation was as described above. As the outer diameter of the stainless steel tube was then 0.25 mm, the PTFE tube was replaced by a tube made of Ismaprene (ID=0.25 mm, SC 0337, Ismatec, Switzerland) glued to the stainless steel outlet (Araldite, Ciba SC, Switzerland).

Preheating layer. In the last generation of microreactors, a second aluminum plate of 9.5 mm width, 12 mm length and 4 mm depth was put on top of the aluminum screen and fixed to the tube by the same procedure (Cyanolyte loctite 401 and Stycast 2651MM). A plate of ceramic containing two resistances was fixed to this aluminum plate (Figure 3-22) with the Stycast 2651MM resin (polymerized two hours at 65°C).

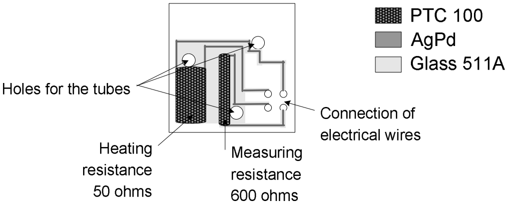

Figure 3-22: Electrical circuit of the electrical preheating layer.

The smaller resistance measured the temperature of the plate (600 Ω) and the larger one (50 Ω) heated the plate to the desired temperature. This electrical circuit was built by silk-screen printing. The paste used for the resistance was a PTC 100.

The entire microreactor assembly in its latest configuration took about half a day of work due to polymerization time of the resin. However only few manipulations were required and several microreactors could be prepared at the same time.

3.5 CONCLUSIONS

Even if the use of microstructured glass offers broad possibilities in chemical applications, the technique of spark-assisted chemical engraving induced many technical difficulties for our particular application and was finally abandoned.

The silk-screen printing technique appeared to be an appropriate way for the construction of the microchannel. It allowed building quickly, reproducibly and at low cost numerous reactors that can be used as disposables for calorimetric measurements. Technical problems such as tube blockade can be easily by-passed by changing the microreactor.

Moreover this approach provides considerable freedom in the design of microreactors. For example, a layout with a third inlet arriving at the end of the reaction channel was constructed. This third inlet allows the quenching of the reaction and the off-line analysis of reaction products by gas chromatography. Many other variations using the same technique can be envisaged depending on the type of application and the problematic encountered.

Chapter 4

ASSESSMENT OF THE DEGREE OF MIXING IN THE MICROCHANNELS

4.1 INTRODUCTION

In the previous chapter, an appropriate way of constructing the microreactors was described. However the efficiency of a microreactor highly depends on the degree of mixing achieved in the reaction channel. This is especially true for fast reactions where mixing can be the rate limiting step. The knowledge of the flow regimen and of the mixing time are thus important issues for the determination of reaction kinetics.

The present chapter is devoted to the characterization of the degree of mixing. The flow characteristics are first theoretically estimated in terms of Reynolds number and pressure drop. The distribution of the residence times in the microchannel is then assessed by the calculation of the Bodenstein number. In a second stage, the flow in the microchannel is simulated by computational fluid dynamics and the expected mixing time is discussed. Finally, the behavior of the flow and the mixing time are measured experimentally using three different methods: a chemical method, a calorimetric method and a visual method using the laser-induced fluorescence of a dye.

4.2 THEORITICAL CALCULATIONS OF THE FLOW CHARACTERISTICS IN THE MICROCHANNEL

In this section, some theoretical models are presented and applied to our current microchannel design i.e. the so-called design 3 (see chapter 3). The Reynolds number is first calculated as a preliminary characterization of the flow. The dispersion model and the segregation model are then discussed.

4.2.1 Hydraulic diameter of the microchannel

As the microchannels are not cylindrical but have a rectangular shape, a hydraulic diameter has to be calculated in order to use the theories developed for tubular reactors. The hydraulic diameter is defined as follows:

$$d_h = \frac{4 \cdot A}{P} = \frac{4 \cdot area}{wetted\ perimeter} \tag{4.1}$$

In the standard microchannel, the width is 250 μm and the depth 100 μm; the hydraulic diameter d_h calculated from equation (4.1) is thus 143 μm. This approximation is however not valid for all rectangular shaped channels, the aspect ratio of the channel has to be calculated to take into account the laminar friction constant f_{Re}. According to White et al [61], the effective diameter d_{eff} can be calculated by:

$$d_{eff} = \left(\frac{64}{f_{\mathrm{Re}}} \right) \cdot d_h \tag{4.2}$$

As reported in the tables [61], for an aspect ratio of 0.4, the f_{Re} is of 65.74. This gives:

$$d_{eff} = \left(\frac{64}{65.74} \right) \cdot d_h = 0.97 \cdot d_h \approx d_h$$

Thus the use of the hydraulic diameter d_h instead of d_{eff} provides a reasonably good estimate for the prediction of the flow characteristics.

4.2.2 Reynolds number and pressure drop

The most common way for characterizing a flow is the calculation of the Reynolds number (equation (4.3)). This parameter allows distinguishing a laminar regimen from a turbulent regimen:

$$\mathrm{Re} = \frac{\rho \cdot u \cdot d_h}{\mu} \tag{4.3}$$

Let's calculate as an example the Reynolds number obtained in the microreactor at a flow rate of 10 μl·min^{-1}.

$$\mathrm{Re} = \frac{1000[kg/m^3] \cdot 6.7 \cdot 10^{-3}[m/s] \cdot 1.4 \cdot 10^{-4}[m]}{8.9 \cdot 10^{-4}\ [kg/m \cdot s]} = 1.0$$

The flow rates used in the microreactor range between 1 and 40 µl·min^{-1}. The same expression (equation (4.3)) is used to estimate the Reynolds number for each different flow rate. The corresponding Reynolds numbers vary between **0.1 and 4.2**.

According to the literature [62, 63], in tubular channels, the flow is laminar for Reynolds numbers below 2100 and turbulent above this value. But some recent publications cast doubt on the application of this theory in the case of microchannels. The relatively high roughness of microchannels might reduce the critical Reynolds number for the transition from laminar to turbulent flow. Peng et al [64] detected transitions to turbulence flow at Reynolds numbers between 200 and 700, with the transition value depending on the hydraulic diameter. This was however contradicted by Pfund [65]. The latter took into account the pressure drop within the channel itself to exclude entrance and exit losses and considered also the surface roughness of the channel for its calculation. Transitions to turbulence were observed with flow visualization. For smaller width channels, the transition occurred at a Reynolds number of 1700.

In any case, the Reynolds numbers achieved in our microchannel are much lower than the critical Reynolds number for transition to turbulent flow. Therefore laminar flow can be assumed in the entire application range of our microsystem. This has an important consequence since it means that mixing occurs only by diffusion and not by convection as in the case of turbulent flow.

Another important parameter to characterize when working with small microchannels is, as mentioned above, the pressure drop obtained through the channels. According to Debray et al [66], in a laminar regimen, the latter can be estimated as follows:

$$\Delta p = \frac{96}{\mathrm{Re}} \cdot \frac{\rho \cdot u^2}{2} \cdot \frac{L}{2e} \tag{4.4}$$

In the domain of flow rates currently used (1-40 µl·min^{-1}) the pressure drop varies between 20 and 763 Pa. This corresponds to a $\Delta p/L_{tot}$ ranging between **1 and 41 kPa·m^{-1}**. The pressure drop in the microchannel is thus negligible in this application range.

4.2.3 Tubular reactor with laminar flow

The calculations above predict pure laminar flow in the entire domain of flow rates used. The purpose of the present subsection is to calculate the corresponding velocity profile in the tube and to estimate the distribution of residence times in the microchannel.

According to Taine et al [67], the axial velocity varies in the radial direction following the Hagen-Poiseuille equation:

$$u(r) = 2 \cdot \bar{u} \cdot \left[1 - \left(r/R\right)^2\right] \tag{4.5}$$

The linear rate profile in a laminar regimen is shown in Figure 4-1.

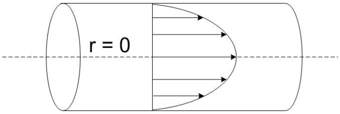

Figure 4-1: Velocity profile in the tubular reactor with laminar flow.

Assuming such a laminar velocity profile in the microchannel, the distribution of the residence times can be derived according to Baerns et al [68] and corresponds to:

$$\frac{d\dot{V}}{\dot{V}} = E(t) \cdot dt = \frac{\tau^2}{2 \cdot t^3} dt \tag{4.6}$$

Where the space time τ is defined as follows:

$$\tau = \frac{V}{\dot{V}} \tag{4.7}$$

The conversion observed can then be written as:

$$\overline{X} = \int_{t_{\min}}^{\infty} X(t) \cdot E(t) \cdot dt \tag{4.8}$$

For a first order reaction,

$$\overline{X} = \int_{t_{\min}}^{\infty} (1 - \exp(-k \cdot t) \cdot \frac{\tau^2}{2 \cdot t^3} \cdot dt \tag{4.9}$$

The characterization of reactions with more complex kinetics than first order involves more complex calculations.

However for the derivation of these equations, the mass transfer was not taken into account. In fact, the solute transported in the flow diffuses between streamlines and will also move forward or backward relative to the average fluid velocity by molecular diffusion (Fick's law). With both axial and radial diffusion occurring, the distribution of residence times of the solute transported is modified. If the radial diffusion of the solute is faster than the axial diffusion, the velocity profile of the solute tends to a plug-flow reactor (see Figure 4-2).

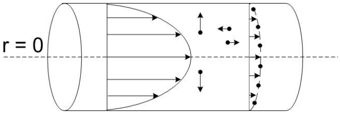

Figure 4-2: Influence of the axial and radial diffusion of the solute transported in the flow on the distribution of the residence times.

The transport of solute should therefore be described by a convective-diffusion equation and this is done in the next paragraph using the dispersion model.

4.2.4 Dispersion model

The mass flow due to dispersion can be described by Fick's law:

$$J = -D_{ax} \cdot \frac{dC}{dz} \tag{4.10}$$

In this model [69, 70], the main parameter is the axial diffusion constant D_{ax} and an dimensionless number called Bodenstein number is defined to characterize the behavior of the reactors.

$$Bo = \frac{u}{D_{ax}} \cdot L \tag{4.11}$$

The Bodenstein number *Bo* characterizes the ratio between the convection and the axial diffusion in a tube of length *L* where a fluid flows at an axial velocity *u*.
Bo tends to infinite for an ideal plug-flow reactor and to zero if the back mixing is very high. In the second case, the reactor behaves more like a flow-through stirred tank reactor.
The profile in the channel is considered as being a plug-flow when *Bo* exceeds 100.

The axial diffusion is calculated using the following expression [68]:

$$\frac{D_{ax}}{u} = \frac{D_m}{u} + \frac{u \cdot d_h^{\,2}}{\chi \cdot D_m} \tag{4.12}$$

In equation (4.12), χ is a constant equal to 192 and D_m is the molecular diffusion constant equal to $1 \cdot 10^{-8}$ $m^2 \cdot s^{-1}$ for protons.
The axial diffusion calculated by this formula varies with the linear velocity and thus with the space time in the channel when the same design is used (Figure 4-3).

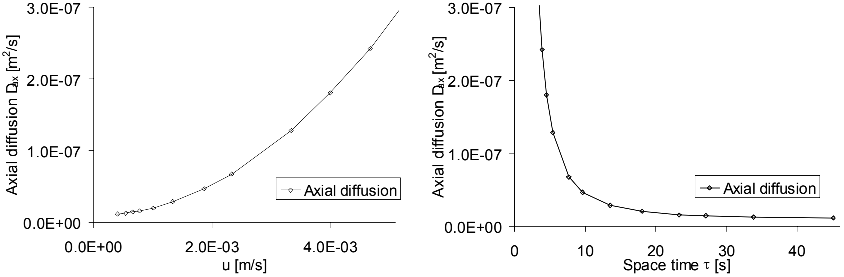

a) b)

Figure 4-3: Variation of the axial diffusion a) with the linear velocity and b) with the corresponding space time for the microreactor of design 3.

The Bodenstein number thus varies with the velocity and its optimum can be calculated:

$$\left(\frac{u}{D_{ax}}\right)_{\max} \text{ for } u = \sqrt{\chi}\cdot\frac{D_m}{d_h} \tag{4.13}$$

In our case this corresponds to a linear velocity in the microchannel of 1 mm·s^{-1} i.e. a space time of around 18 s. The corresponding flow rate is 1.5 µl·min^{-1}.

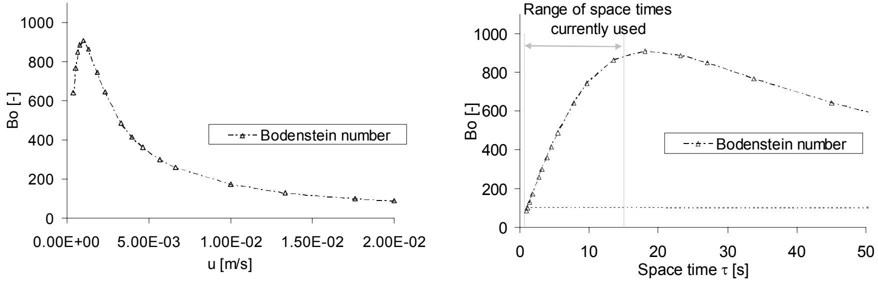

a) **b)**

Figure 4-4: Variation of the Bodenstein number a) with the linear velocity and b) with the corresponding space time for the microreactor of design 3.

Figure 4-4b shows that for space times exceeding 0.5 s, the *Bo* is higher than 100 and the microreactor therefore behaves like a plug-flow microreactor. In the range of space times currently used (from 0.5 to 15 s), back mixing is thus negligible. The corresponding range of flow rates is between 2 and 40 µl·min^{-1} in the design 3 microchannel i.e. between 1 and 20 µl·min^{-1} for each inlet.

This prediction of plug-flow behavior of the solute in the microchannel will be an important point for the determination of reaction kinetics. The residence time in the channel is thus directly given by the space time[2]. It will significantly simplify the calculations.

4.2.5 Segregation model

Moreover, the segregation in the microchannel has to be characterized. The time required to achieve complete mixing can be calculated as follows [69]:

$$t_D = \frac{d_h^{\,2}}{4\cdot D_m} \tag{4.14}$$

In our case, the hydraulic diameter d_h is equal to 143 µm (subsection §4.2.1) and the molecular diffusion constant D_m is $1\cdot10^{-8}$ m^2·s^{-1} for protons; t_D is then 0.51 s. This mixing time has to be compared to the time of reaction.

The time of reaction can be calculated as follows:

---

[2] In the rest of this work, the term residence time is used instead of space time.

$$t_{rx} = \frac{c_0}{R_0} \tag{4.15}$$

For the characterization of reaction kinetics, the mixing time should be short compared to the time of reaction. This is checked for the kinetics in chapter 6.

4.3 COMPUTATIONAL FLUID DYNAMIC 2D-SIMULATION OF THE FLOW IN MICROCHANNELS

Computational fluid dynamic simulations are often used in the literature to predict and analyze the results obtained with microreactors [71, 72]. This method is based on three fundamental principles: mass conservation, energy conservation and the second law of Newton (F = ma). These fundamental principles can be expressed in terms of partial differential equations. Computational Fluid Dynamics (CFD) allows determining a numerical solution to these equations of fluid flow.

The program used for these simulations is called FEMLAB and is a toolbox of Matlab developed by Comsol. FEMLAB is an interactive environment for modeling and simulating scientific and engineering problems based on partial differential equations. FEMLAB offers CAD tools, interfaces for physics or equation definitions, automatic mesh generation, equation solving, visualization and post-processing.

The 2D-simulation of the mixing has been performed for the four layouts made by silk-screen printing (d=250 μm) described in chapter 3. The detailed choice of the parameters for the simulation is explained in the next subsection.

4.3.1 Definition of the system of equations

4.3.1.1 Navier-Stokes equation for incompressible fluids

The 2-D incompressible Navier-Stokes equation describes the velocity profile in the microchannel. For a stationary state, this equation can be written as follows:

$$\begin{cases} -\mu\nabla^2 u + \rho(u \cdot \nabla)u + \nabla p = F \\ \nabla \cdot u = 0 \end{cases} \tag{4.16}$$

Boundary conditions. The choice of the velocity profile at the two inlets determines the resulting velocity fields in the reaction channel.

Because of the 2D-geometry, the Hagen-Poiseuille equation (4.16) valid in a 3-D tubular reactor, cannot be directly applied. The profile established in this simulation corresponds to the velocity field achieved between two planar parallel plates with a maximal velocity equal to 3/2 of the average velocity.

At the borders of the channel, the velocity is set to zero (u,v=0). At the inlets, two different profiles can be introduced. One way to proceed is to set the velocity at the inlets constant along the width of the channel. The velocity profile is then established after a few micrometers. Another way is to directly introduce the velocity profile expected as inlet profile. The second approach was chosen for these simulations since it allows to speed up and to facilitate the convergence of the computation. The velocity profile used was:

$$u = 6 \cdot \overline{u} \cdot s \cdot (1 - s) \tag{4.17}$$

The parameter s is a FEMLAB parameter varying from 0 until 1 along the channel (being 0.5 at the center of the channel).
At the outlet, the pressure was set to zero.

Properties of the fluid. The physical properties of water have been used (ρ=1000 kg·m^{-3}, μ=1·10^{-3} kg·m^{-1}·s^{-1}).
Additional friction forces are set to zero because of the small size of the channels.

4.3.1.2 Convection and diffusion equation

The behavior of the solute in the microchannel is calculated using the convective-diffusion equation. In stationary state, this equation can be written:

$$\nabla(-D_i \cdot \nabla c_i + c_i \cdot u) = R_i \tag{4.18}$$

Boundary conditions. The solute concentration was arbitrarily set at 1.5 at the first inlet and at zero at the second inlet. This simulates the diffusion of a tracer in pure water. At the outlet, it was assumed that the convection was much higher than the diffusion. The orthogonal mass flows were set at zero (Ni · n=0) at the channel borders.

Properties of the fluid. As the purpose of these first simulations was the characterization of the mixing, the solute was considered as a non-reactive species. The molecular diffusion constant of the solute was considered isotropic and set at 1·10^{-8} m^2·s^{-1} which corresponds to the diffusion of the H$^+$ species.

Simulations of a flow transporting two reactive species in the microchannel were also performed and are presented in chapter 6.

4.3.2 Meshing of the geometry

In the finite element model, the geometry is divided in several triangles and the differential equations are solved for each node of the resulting weft. The division of the geometry is called the meshing and should obey to some restrictions to guarantee the convergence of the calculations. The mesh Peclet number should be lower than the critical value of 100 and a mesh Reynolds number lower than 10 allows a better accuracy of the results [73].

The typical sizes of the meshes are around 30 µm. The maximal linear velocity tested in the microchannel is 2.66·10^{-2} m·s^{-1} which corresponds to an inlet flow rate of 10 µl·min^{-1}.

The corresponding mesh Reynolds number and mesh Peclet number are then:

Typical mesh Reynolds number $\mathrm{Re} = \dfrac{\rho \cdot u \cdot d_{mesh}}{\mu} = 0.8$

Typical mesh Peclet number $Pe = \dfrac{u \cdot d_{mesh}}{D_m} = 80$

A good convergence and accuracy of the computation is thus predicted for the entire range of velocity tested.

4.3.3 Parameters used for the equation solving

The differential equations defined in subsection §4.3.1 are expressed for each node and assembled in a matrix A. The system of equation can thus be simplified as follows:

$$A \cdot x = b \tag{4.19}$$

This matrix A is complex but sparse (contains many zero values). To solve equation (4.19), FEMLAB uses the Gauss method [74, 75]. In this method, the matrix A is broken down into two matrices L and U ($A = L \cdot U$). L is the lower triangular matrix and U the upper triangular matrix. This operation allows lowering the number of zero values.

Let's put down that $U \cdot x = y$, knowing L, U and b, the algorithm does first a descent to solve $L \cdot y = b$ and then an ascent to solve $U \cdot x = y$ and find x.

The equation solving is performed in stationary state using an iterative solver. This iterative method requires the use of a preconditioner. The preconditioner used for these simulations is the standard preconditioner suitable for general applications and is called "Incomplete *LU*" preconditioner. The linear solver chosen was the default solver called "Good Broyden".

4.3.4 Results obtained for the mixing in the four layouts

4.3.4.1 Velocity fields

As an example, the velocity field in Design 3 is shown for a linear velocity of $6.66 \cdot 10^{-3}$ m·s^{-1} in each feed channel i.e. $1.33 \cdot 10^{-2}$ m·s^{-1} or 20 µl·min^{-1} in the reaction channel (Figure 4-5a). Figure 4-5b shows a cross-section plot of the velocity profile at the end of the reaction channel.

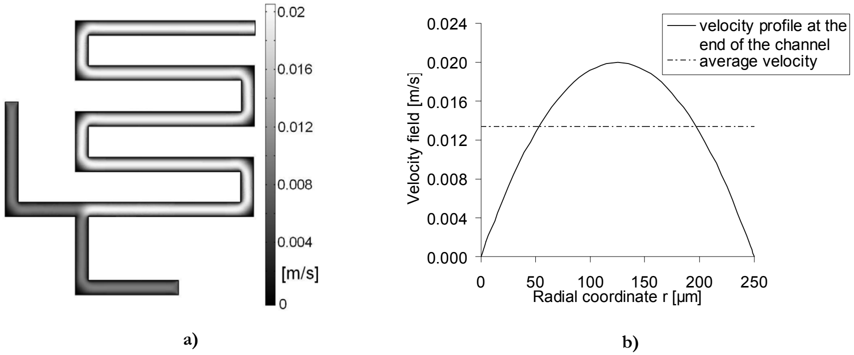

Figure 4-5: Velocity fields for Design 3 at a velocity in the microchannel of 1.33 ·10^{-2} m·s-1 (total flow rate of 20 µl·min^{-1}). a) Representation of the velocity fields in the entire reaction channel, b) Velocity field at the end of the reaction channel.

As expected, the velocity in the center of the channel is 3/2 times the average velocity. The resulting velocity fields are similar in the entire channel length and no eddies indicating turbulent flow are predicted. Some dead zones are observed in angles.

4.3.4.2 *Comparison of the mixing in the four layouts*

As stated in subsection §4.3.1.2, in order to assess the quality of mixing in the four layouts, the mixing of a fluid having a concentration of tracer of 1.5 mol·l^{-1} with pure water was simulated. This tracer was assumed to diffuse like a proton. For complete mixing, the expected tracer concentration at the end of the channel should be 0.75 mol·l^{-1}.

The concentrations in the channel were calculated using the velocity profiles calculated in subsection §4.3.4.1 and the convection and diffusion equation. Figure 4-6 shows the variation of the concentration of tracer along the channel. A tracer concentration of 1.5 mol·l^{-1} is represented in white and pure water (c=0 mol·l^{-1}) is represented in black.

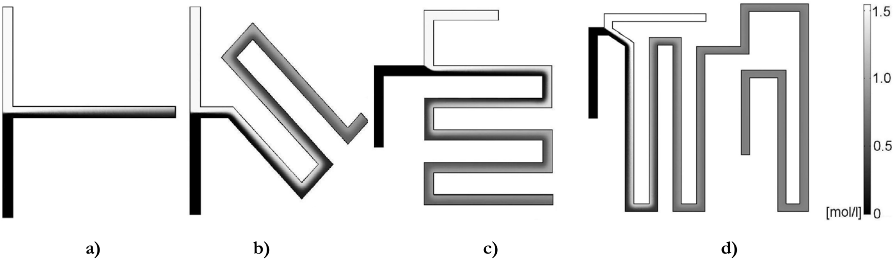

Figure 4-6: Concentration profile when introducing a tracer in one inlet for Design 1 (a), Design 2 (b), Design 3 (c) and Design 4 (d).

At the beginning of the channel, both fluids flow as two separate layers. This is typical for a fully laminar system. These two layers mix then slowly along the channel by radial diffusion.

Cross section plots are represented at the end of the channel to evaluate the distribution of the tracer in the channel and thus to characterize the degree of mixing of the reaction channel. This is done for each design of the reaction channel and for various flow rates. As an example, Figure 4-7 shows the profiles obtained at the outlet in Design 3 with different flow rates.

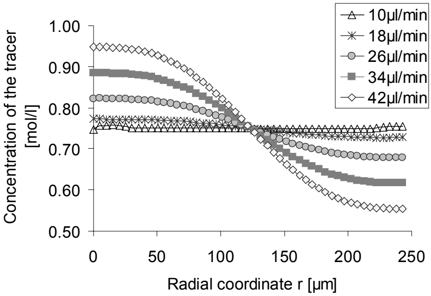

Figure 4-7: Cross section plot of the concentration at the end of the reaction channel of the design 3 for various flow rates in the reaction channel.

As seen in Figure 4-7, for Design 3, with a flow rate of 10 µl·min^{-1}, the concentration is homogeneous across the channel; the mixing is complete. At an inlet flow rate of 26 µl·min^{-1} and above, two separate layers of concentrations are observed and mixing is no more complete.

In order to compare more easily the quality of mixing obtained with different designs and different flow rates, an index of segregation was defined as follows,

$$X = 1 - \frac{c_{r=240\mu m}}{c_{r=10\mu m}} \tag{4.20}$$

The parameter *r* is the radial coordinate, the values at 10 µm and 240 µm were chosen in order to avoid the border effect and the potential divergence at the surface of the channel walls. This index is equal to zero when the concentration is homogeneous along the width of the channel, which means that the mixing is complete in the microreactor and is equal to one when there is still no mixing in the channel ($c_{x=240\,\mu m}=0$).

The four different designs were then compared using this index of segregation (Figure 4-8).

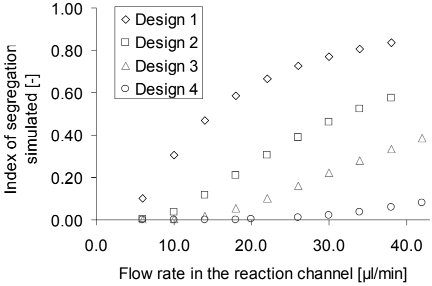

Figure 4-8: Comparison of the mixing achieved in the four designs using the index of segregation.

As seen in Figure 4-8, a raise of the index of segregation is observed with increasing flow rates and with decreasing length of the reaction channel. This is due to the related variation of the residence time in the channel. For short residence times, the tracer has less time to diffuse across the channel and the degree of mixing drops.

To observe the influence of the bends of the reaction channel or of the type of mixer used (T-mixer or V-mixer), one has to compare the index of segregation obtained for the same residence time with the different flow rates (see Figure 4-9).

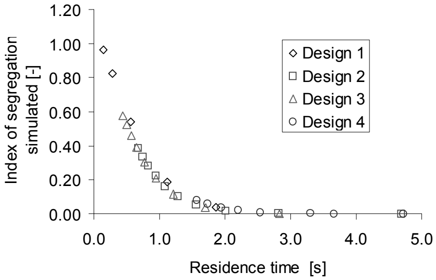

Figure 4-9: Index of segregation obtained for the four designs versus the residence time in the reaction channel.

As seen in Figure 4-9, the type of mixer and the number of bends of the reaction channel do not influence the time required for mixing. Flow is purely laminar in every case and the mixing time is given by the time of radial diffusion in the channel. In the geometry drawn for these 2D-simulations the hydraulic diameter of the channel is, in this case, 250 µm, the corresponding time for radial diffusion is thus, according to equation (4.14):

$$t_D = \frac{\left(2.5\cdot10^{-4}\right)^2}{4\cdot1\cdot10^{-8}} = 1.56s$$

This value correlates well with the observations in Figure 4-9.

4.4 EXPERIMENTAL ASSESSMENT OF THE MIXING TIME

Many techniques have been reported in the literature for the assessment of the degree of mixing in a microchannel. They can be mainly divided in two categories: qualitative methods and quantitative methods. Among the qualitative methods, one can find the use of pH indicators such as phenol red in phosphate buffers [43] or methyl orange or the assessment of the size of an air bubble when air and water are mixed [76]. The use of parallel systems of chemical reactions is a quantitative method. Various reactions have been proposed in the literature in particular the Bourne reaction [77, 78] or the Barthole reaction [79]. The Dushman reaction is however more appropriate for the determination of short mixing times.

The degree of mixing was determined experimentally using three different methods. It was first estimated using the Dushman reaction. The observations and conclusions obtained with this technique were then verified by a calorimetric method. Finally, the mixing was recorded in real time by laser induced fluorescence of a pH-dependent dye.

4.4.1 The Dushman reaction (iodate-iodide system)

4.4.1.1 Principle of the measurements

The Dushman reaction is one of the most frequently used chemical system for the assessment of mixing [80-84]. This method is based on a competitive parallel reaction system:

$H_2BO_3^- + H^+ \leftrightarrows H_3BO_3$ quasi-instantaneous (I)
$5\,I^- + IO_3^- + 6\,H^+ \leftrightarrows 3\,I_2 + 3\,H_2O$ very fast (II)

H^+ is added in stoechiometric defect. In case of perfect mixing, H^+ is totally consumed by the first reaction and no iodine (I_2) is produced. If the incoming feed stream is segregated, there are locally higher concentrations of H^+ and the second reaction takes place. The iodine reacts then instantaneously further:

$I_2 + I^- \leftrightarrows I_3^-$ (III)

The product I_3^- is stable and can be analyzed off-line by UV-spectrometry at 352 nm. The amount of iodide ions is proportional to the segregation in the channel.

Guichardon et al. [84] determined the kinetics of the Dushman reaction, confirmed the fifth-order process widely reported [80] and proposed a simple micromixing model to quantitatively determine the time of micromixing.

4.4.1.2 *Experimental protocol*

The concentrations had to be optimized to improve the sensitivity of the method in the small reaction channels [83]. The following concentrations were used: $c_{KIO3} = 2.3 \cdot 10^{-3}$ mol·l^{-1}, $c_{KI} = 1.7 \cdot 10^{-2}$ mol·l^{-1}, $c_{NaOH} = 9.1 \cdot 10^{-2}$ mol·l^{-1}, $c_{H3BO3} = 1.8 \cdot 10^{-1}$ mol·l^{-1} and $c_{H+} = 2.0 \cdot 10^{-2}$ mol·l^{-1}.

The flow rates of the feed streams varied from 3 to 19 μl·min^{-1}. One syringe contained the solution of KIO_3, KI, NaOH and H_3BO_3; the other syringe contained the aqueous solution of sulphuric acid.

A sample of 50 μl was taken off-line once steady state was achieved. The absorbance at 352 nm of the reaction product I_3^- was measured at each flow rate. Absorbance measurements were performed in a 50 μl cuvette (HELLMA) with an UV-spectrometer HP 8452 (Hewlett Packard, USA). Ideal mixing is characterized by an absorbance at 352 nm close to zero.

The microreactors used for these experiments were the Designs 1, 2 and 3 presented in chapter 3 with large outlet tubes (ID=0.65 mm). The advantage of having an outlet tube much larger than the microchannel size is to observe a significant drop of the degree of mixing when the mixing is not achieved in the reaction channel.

4.4.1.3 *Results and discussions*

A slight degradation of the resulting iodine was observed during the time required to fill the UV cuvette. Therefore the absorbance values obtained cannot be directly used for quantitative calculation of the micromixing time but are rather used for qualitative observations.

The degree of mixing was assessed in three different designs in order to evaluate the influence of the length and of the geometry of the channel on the quality of mixing (see Figure 4-10).

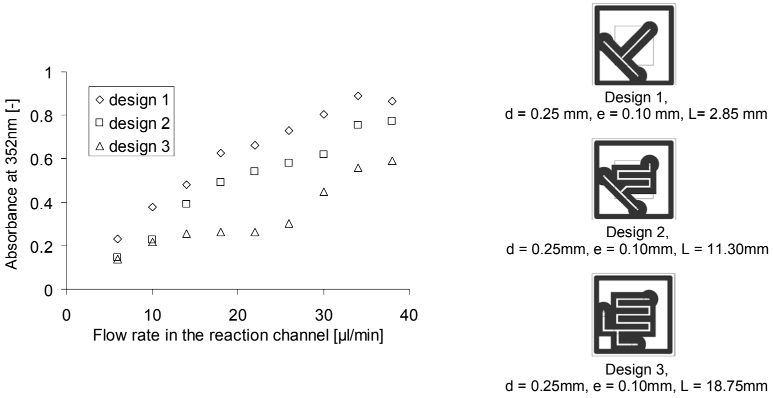

a) b)

Figure 4-10: a) Influence of the geometry of the microchannel on the degree of mixing achieved at various flow rates, b) reminder of the corresponding geometry of the microchannels.

As predicted with simulations (see subsection §4.3.4.2), the absorbance increases with increasing flow rates for all three designs. In addition, it appears that at a fixed flow rate, the longer the channel, the better the degree of mixing. This is expected since the residence time in the microchannel is also longer. This trend was also observed by Floyd et al. [43]. Floyd measured the degree of mixing using two phenol red streams at pH of 6.4 and 8.0 and measured the absorbance on-line at the end of the channel. At low flow rates, the absorbance dropped because the solution had a pH close to 7.2. An inverse trend was reported by Ehrfeld et al. [85] using the iodide-iodate system, but this was explained by the very high flow rate used (more than 1000 times higher than the ones used in our layout). In this case, the slow formation of iodine (reaction II) was only observed at low flow rates and the absorbance increased as the residence time increased.

In Figure 4-11, the data of Figure 4-10a have been plotted as a function of the residence time instead of the flow rate.

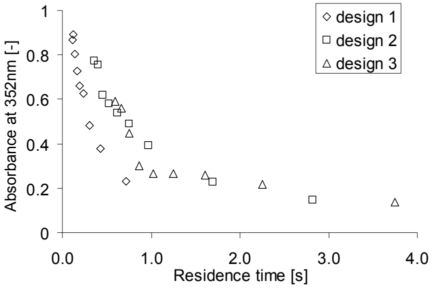

Figure 4-11: Absorbance at 352 nm obtained in the three different designs according to the residence time in the reaction channel.

Figure 4-11 shows that, for residence times exceeding 1 s, the degree of mixing is practically independent of the design of the reaction channel and of the flow rate. This is expected for a fully laminar system [85]. However for shorter residence times, a significant raise in the absorbance value is observed. The degree of mixing becomes highly dependent on the flow rate. Mixing is not achieved within the reaction channel and takes place in the outlet tube. Since the outlet tube has a larger diameter than the reaction channel, a higher degree of segregation is observed.

It was predicted from theoretical calculations and from simulations that the flow was laminar and that mixing was only achieved by molecular diffusion. As calculated in subsection §4.2.5, the time of radial diffusion in the microchannel is approximately 0.5 s in the case of protons. For shorter residence times, mixing is achieved in the outlet tube. The experimental value is even slightly longer than expected; this shows that there are no turbulences induced that would shorten the mixing time.

In the three layouts tested, the shape of the reaction channel did not significantly affect the degree of mixing. However a sufficient length of the channel was found necessary to ensure that the mixing is entirely achieved within the reaction channel. This is important for calorimetric measurements since only the reaction channel is in contact with the sensitive area of the calorimetric chip.

4.4.2 Using calorimetric measurements

The neutralization of H_2SO_4 by NaOH was performed in a microchannel of Design 1 with a slightly smaller depth than the classical microreactor, 80 μm instead of 100 μm. As this reaction is quasi-instantaneous, the limiting step is mixing.

The time required for complete mixing by molecular diffusion was re-calculated for this channel depth:

$$t_D = \frac{d_h^{\,2}}{4 \cdot D_m} = 0.37\text{s}$$

The experimental results are presented in Figure 4-12.

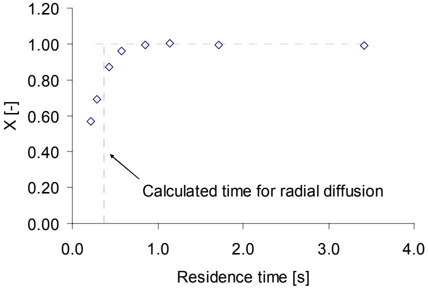

Figure 4-12: Neutralization of H_2SO_4 by NaOH- Reaction limitation due to the mixing.

As seen in Figure 4-12, for residence times equal to or shorter than about 0.5 s, the entire amount of heat expected is not measured. This gives us an experimental value of the mixing time. As observed with the Dushman reaction, the mixing time measured experimentally is slightly longer than the time predicted for radial diffusion, meaning that no turbulence is involved. This again proves that the mixing in the channel is limited solely by molecular diffusion.

4.4.3 Using Laser Induced Fluorescence (LIF) measurements

4.4.3.1 Principle of the measurement

During the past 15 years, there has been a remarkable growth in the use of fluorescence in biological sciences. Recently, applications have also been proposed in process engineering and fluid dynamics research. Laser induced fluorescence (LIF) is an optical measuring technique used to assess instantaneously whole fields of concentration [86] or temperature [87] in fluid flows.

A fluorescent dye is introduced in the vessels and labels the fluid. Excited by a laser source (typically Nd:YAG or Argon-ion lasers), the latter absorbs the light energy and re-emits light at a longer wavelength that can be detected by a photodetector. This photodetector is a CCD camera equipped with a sharp cut-off or narrow-band filter, so that only fluorescent light is recorded. This camera acts as an array of light detectors (pixels). In μ-LIF, the photographic lens used for conventional LIF is replaced by a microscope lens.

The set-up of the system is shown in Figure 4-13.

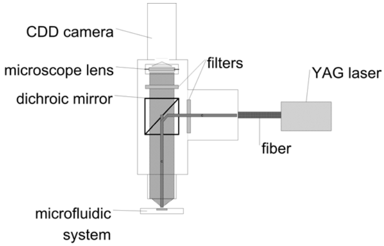

Figure 4-13: Simplified set-up for micro-laser induced fluorescence.

The measurements were performed in collaboration with the company Dantec Dynamics (Erlangen, Germany).

4.4.3.2 Experimental protocol

Microreactors similar to the ones currently used were constructed on a glass layer (see chapter 3). However, the silk-screen printing of the channel on a glass layer was not as precise as on an alumina layer and the internal volume of the channel could not be precisely controlled. Therefore quantitative results could not be obtained. Nevertheless this technique allowed to observe the mixing and to visualize the stationary state of the flow.

The fluorescence dye SNARF-5F (Molecular Probes, Netherland) was introduced in the reaction channel and excitation was achieved by a YAG laser at 543 nm. The dye chosen showed a pH dependent absorbance (See Figure 4-14).

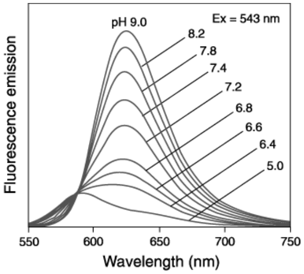

Figure 4-14: Emission spectra of the dye SNARF-5F at various pHs (between 5.0 and 9.0).

One milligram of the dye was dissolved into 100 ml of distilled water. NaOH was added to set the pH of the resulting solution at 9 ($c_{NaOH}=1.0 \cdot 10^{-3}$ mol·l^{-1}). A sulphuric acid solution at pH 3 ($c_{H2SO4}=1.1 \cdot 10^{-3}$ mol·l^{-1}) was also prepared. The alkaline solution was introduced into a syringe; a second syringe contained the acidic solution. The pH of the resulting solution was 4. At this pH, there was no fluorescence emission of the dye. Proton diffusion was measured by following the decrease of the dye fluorescence.

The experimental set-up is shown in Figure 4-15.

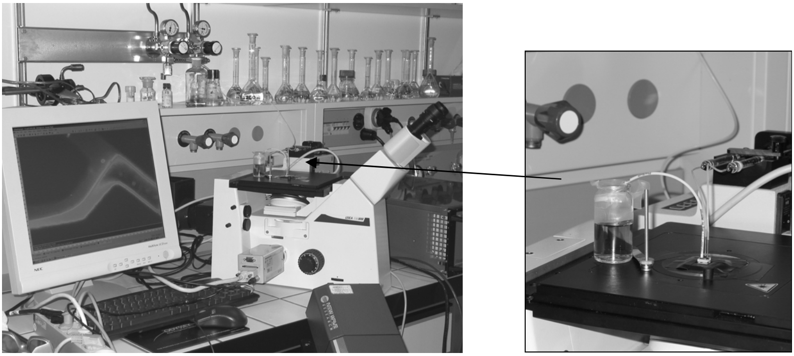

Figure 4-15: Picture of the equipment used to perform LIF measurements.

Mixing was observed for the four designs of microchannels shown in section §4.3.4.2. For each design, the flow rates were changed and the concentrations at the inlet and the outlet of the channel were recorded. Due to the magnification of the microscope, pictures of the entire reaction channel could not be taken. However, movies of the flow behavior along the channel were recorded.

4.4.3.3 Results and discussions

In the following pictures, the dye is bright before reaction with the protons and becomes darker after reaction (no fluorescence).

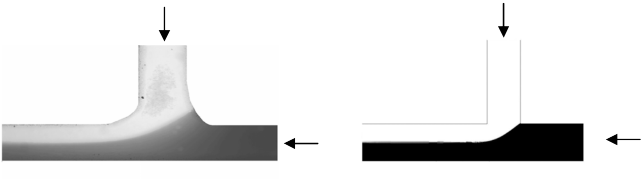

a) b)

Figure 4-16: Inlet of Design 3, 2 µl·min^{-1} a) picture taken by LIF measurements, b) FEMLAB-based simulations. The white part is the dye in the alkaline solution and the black part is the acidic solution.

Figure 4-16a shows a picture of the mixing taken at the inlet of Design 3 with a flow rate of the feed stream of 2 µl·min^{-1}. The white part is the dye in the alkaline solution and the black part is the acidic solution. The flow is clearly laminar; the inlet streams are clearly separated. A small area of diffusion can be observed between the two layers. The movies recorded showed that at flow rates lower than 2 µl·min^{-1} the pulses due to the micro-step motor of the pump were detectable.

FEMLAB-based simulations were performed for the same geometry (Figure 4-16b), with a molecular diffusion coefficient corresponding to proton diffusion ($1 \cdot 10^{-8}$ m^2·s^{-1}). The white part corresponds to a high concentration of protons (c_0=1.5 mol·l^{-1}) and the black part corresponds to pure water (c=0 mol·l^{-1}). A perfectly mixed solution corresponds then to a concentration of $c_0/2$ and is gray.

In the experiments above, the representation of the mixing is binary: the fluid is either black (mixed) or white (not mixed). No shading can be observed. In order to get a better insight of the mixing pattern, the color range of the simulation was decreased from 0-1.5 mol·l^{-1} to 0.7-0.8 mol·l^{-1}. When the proton concentration exceeds 0.8, the fluid is white (not mixed). Below this value, the fluid is considered as mixed (black).

Pictures at the end of the channel were also taken to see the degree of mixing achieved at various flow rates (Figure 4-17). Quantitative information cannot be obtained but the images could be qualitatively compared with the CFD simulation (with a color range of 0.7 mol·l^{-1}-0.8 mol·l^{-1} as explained above).

a) Inlet flow rate of 2 µl·min^{-1}

b) Inlet flow rate of 5 µl·min^{-1}

c) Inlet flow rate of 10 µl·min^{-1}

Figure 4-17: End of the reaction channel for Design 3 at three inlet flow rates. Qualitative comparison of the experiments with the simulations.

For a feed stream flow rate of 2 µl·min^{-1}, mixing was entirely achieved at the end of the channel (Figure 4-17a). For a flow rate of 10 µl·min^{-1}, mixing was not complete (Figure 4-17c) and the flow was still perfectly laminar. The diffusion zone can clearly be seen in the experiments as well as in the simulation. Experiments and simulations correlate very well.

The same experiments were performed for Design 2 corresponding to a T-mixer (Figure 4-18).

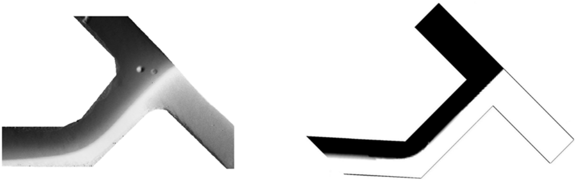

a) **b)**

Figure 4-18: Mixing in the inlet of Design 2 at 2 µl·min^{-1} a) measured by LIF b) simulated using FEMLAB.

The same laminar regimen was observed with the T-mixer. Movies showed a very stable behavior at stationary state. With this layout, the pulses of the pump were not visible even at flow rates of 1 µl·min^{-1}.

These µ-LIF experiments confirmed that the flow in the microchannel occurred exactly as predicted by CFD simulation. The flow is not stuck in the angle. The two inlet streams are parallel and do not enter in the reaction channel in small blocks. No unexpected phenomenon was observed.

4.5 CONCLUSIONS

In this chapter, the mixing time in the reaction channel was calculated theoretically, estimated by CFD simulations and measured experimentally using three different techniques.

Theoretical calculation predicted that the flow is purely laminar but due to the high Bodenstein number of the microchannel (high radial diffusion of the solute compared to the linear velocity of the flow) the solute transported in the flow behaves like in an ideal plug-flow reactor. This will significantly simplify the distribution of the residence times of the solute in the microchannel and thus the characterization of reaction kinetics.

The experimental results confirmed that flow was purely laminar and that the mixing time corresponded to the time of radial diffusion in the channel. The mixing time could thus be easily estimated for the different layouts used. For the type of microchannels used in this work (d=250 μm, e=100 μm), this time corresponded to 0.5 s. This value was integrated in the following experiments by working with residence times in the channel always longer than 0.5 s. Smaller diameters would be needed when working with substances with a lower molecular diffusion than protons.
Finally, Laser-Induced Fluorescence measurements allowed to visualize the flow and to verify that it was as predicted by CFD simulations.

Chapter 5

THE MICROREACTOR-BASED CALORIMETRIC SYSTEM

5.1 INTRODUCTION

In chapter 4, the degree of mixing obtained at the end of the reaction channel was determined for different layouts of microchannels.

In the present chapter, the microreactor is introduced into the commercially available calorimeter (Setline 120 from Setaram, see chapter 2) and the suitability of the resulting microreactor-based system for calorimetric measurements is investigated.

After explaining the calibration method of the system, improvements related to the efficiency of the system are presented detailing the purpose and effect of each modification.
To get a better insight of these effects and to define the relevant resistances of the system towards heat transfer, a heat balance is then performed on the microcalorimetric cavity. Moreover, the preheating of the incoming fluids is investigated to shield the system against external influences.
Finally, the repeatability and reproducibility of the system are checked.

5.2 CALIBRATION OF THE MODIFIED CALORIMETRIC SYSTEM

Two different calibrations were required in our system. The first calibration (described in subsection §5.2.1) corresponds to the calibration of the microcalorimetric chip and is also performed when using the Setline 120 calorimeter in the standard manner (with a crucible). The second calibration (described in subsection §5.2.2) characterizes the efficiency of the heat transfer from the reaction channel to the sensitive part of the microcalorimetric membrane.

5.2.1 Using the heater resistance

As stated in chapter 2, the raw signal delivered by the calorimeter is directly recorded by the thermopile as a voltage in microvolts. A calibration is therefore required to determine the thermal sensitivity of the chip, i.e. to convert this voltage into thermal power [W].

This is done using a heater resistance incorporated in the center of the sensitive area. A Joule effect of $\dot{q} = 1\text{mW}$ is applied to the system during 60 s (or 120 s) and the resulting output voltage, U, measured by the thermopile, is integrated. The thermal sensitivity of the chip S_q can be calculated from the following equation:

$$S_q = \frac{U}{\dot{q}} \tag{5.1}$$

This sensitivity is systematically determined before each measurement by performing two impulses at 1 mW.

However, this sensitivity only characterizes the microcalorimetric chip but not the entire system. The heat transfer from the reaction channel to the membrane of the chip is not taken into account and a complementary calibration is therefore needed.

5.2.2 Using a chemical reaction

In our novel system, the reaction takes place in the reaction channel of the microreactor. The heat released in the channel can be distributed in four main ways:

- in the sensitive part of the microcalorimetric membrane (desired way),
- in the non-sensitive part of the microcalorimetric membrane,
- in the stainless steel tubes, or in the air above the reactor,
- as heat accumulation in the outlet flow.

Only the heat distributed in the sensitive part of the microcalorimetric membrane is measured; the heat distributed in other directions leads to heat losses.

A calibration is therefore needed to correlate the heat flow released in the microchannel by the chemical reaction $\dot{q}_{rx}$ with the heat flow effectively measured $\dot{q}_{meas}$ (heat distributed in the sensitive part of the microcalorimetric membrane). This ratio is called the thermal efficiency and is used as a correction factor, F, in all subsequent experiments:

$$F = \dot{q}_{meas} / \dot{q}_{rx} \tag{5.2}$$

This ratio allows the quantification of heat losses. An important parameter, which determines the thermal efficiency, is the quality of the thermal contact between the reactor and the sensors of the calorimetric membrane. This is presented in detail in section §5.4.

For flow-through reactors, the global heat flow $\dot{q}_{rx}$ released by the reaction in the channel is:

$$\dot{q}_{rx} = \dot{V} \cdot (-\Delta H_r) \cdot (c_0 - c_f) = \dot{V} \cdot (-\Delta H_r) \cdot c_0 \cdot X \tag{5.3}$$

The well-known neutralization of H_2SO_4 by NaOH was selected as calibration reaction (see (I)).

$$H_2SO_4 + 2\ NaOH \rightarrow 2\ H_2O + Na_2SO_4 \tag{I}$$

The enthalpy of this reaction is -130 kJ·mol^{-1} [88] and as this neutralization reaction is quasi-instantaneous, the conversion achieved in the reaction channel is equal to one (X=1). The heat flow released by the reaction is thus, according to equation (5.3), directly proportional to the molar heat flow of reactants, i.e. the flow rate times the initial concentration.

This calibration reaction is carried out in the reaction channel at different flow rates or concentrations. The heat flow measured by the calorimeter is recorded and the heat effectively released in the microchannel is calculated using equation (5.3). The linearity of the heat flow measured with the heat flow expected is then checked (Figure 5-1). The correction factor F or thermal efficiency of the system is the slope of this plot.

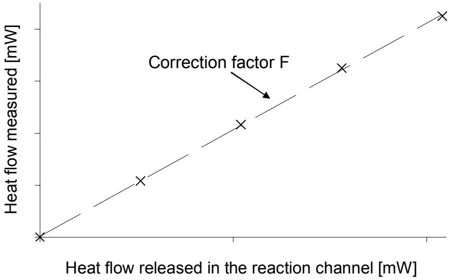

Figure 5-1: Typical plot for the calibration of the system using a chemical reaction.

As explained above, this factor is used in subsequent experiments to calculate the reaction heat flow. By arranging (5.2),

$$\dot{q}_{rx} = \dot{q}_{meas} / F \tag{5.4}$$

This calibration has to be performed for every change in the microsystem, i.e. for geometric changes of the reactor as well as for changes in the position of the microreactor on the sensor.

5.3 OPTIMIZATION OF THE SENSITIVITY OF THE MODIFIED SYSTEM

The microreactor is inserted in the calorimetric cavity of the Setline 120, replacing the crucible classically used (Figure 5-2). As stated in chapter 3, a syringe pump with two Hamilton glass syringes is used for the control of liquid flow rates.

5.3.1 First experiment

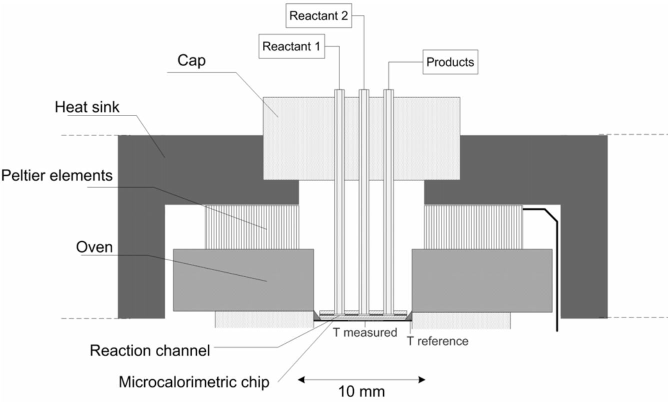

Figure 5-2: First experiment: Introduction of the microreactor in the calorimetric cavity without any modification of the microreactor design.

In a first experiment, the microreactor was simply inserted into the cavity without any modification (see Figure 5-2).

The efficiency of this configuration was assessed using the calibration reaction (see 5.2.2). The flow rate of the feed streams was maintained at 10 µl·min^{-1} and the initial concentrations of H_2SO_4 and NaOH were varied between 0.1 mol·l^{-1} and 0.3 mol·l^{-1}. The raw data are shown in Figure 5-3a and the thermal efficiency is assessed using Figure 5-3b.

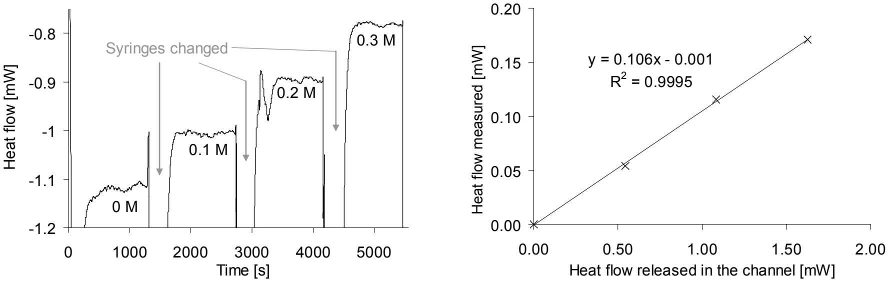

Figure 5-3: Data obtained for the first experiment, T=30°C a) raw data (corrected for the sensitivity of the chip Sq), b) determination of the efficiency.

As can be seen from Figure 5-3b, the signal obtained varied linearly when the concentrations were increased but the thermal efficiency of the system was only 10 %.

In this configuration, the heat released in the microchannel is equally distributed in the entire area of the microcalorimetric membrane. However more than 75 % of the surface of the membrane is non-sensitive (no thermocouples) and the heat conducted in the latter is lost. Indeed, the sensitive part of the membrane is a square of 4 by 4 mm in the center of the 8 by 8 mm squared membrane (see chapter 2). Moreover, the probable residual air layer between the microreactor and the membrane majors the contact resistance and lowers the amount of heat measured.

Thus a first objective was to focus the heat released in the reaction channel as much as possible towards the central, sensitive part of the sensor. These efforts are presented in the following subsection.

5.3.2 Modification in the microreactor design

Some modifications in the microreactor design were required to reduce the contact resistance between the microreactor and the microcalorimetric membrane (Figure 5-4).

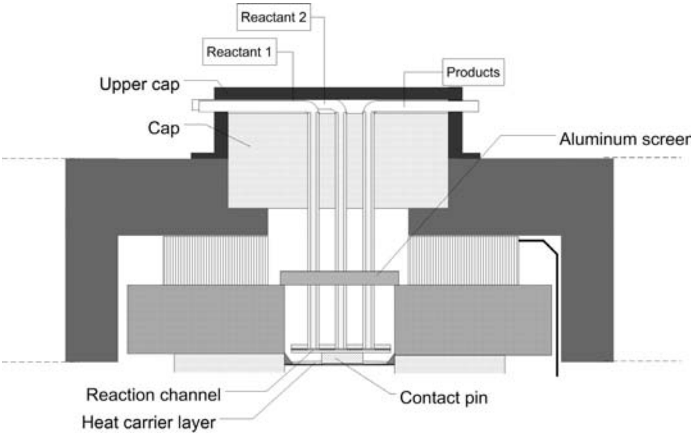

Figure 5-4: Modification of the microreactor performed to improve the sensitivity of the system.

A 4 mm × 4 mm contact pin was glued under the reaction microchannel to direct the heat flow released in the channel to the sensitive part of the microcalorimetric membrane. In addition, a heat carrier (Polyethylene-glycol 300, Fluka, Switzerland) was put in between the contact pin and the microcalorimetric membrane in order to eliminate the air layer between these two elements.

An aluminum screen was glued to the inlet and outlet tubes, mimicking the screen present in the original configuration of the calorimeter (see chapter 2). This screen ensured a reproducible positioning of the microreactor in relation to the microcalorimetric membrane and formed a thermal bridge above the oven that allowed the preheating of the incoming fluids. The effect of the aluminum screen on the preheating of the fluids is discussed in the next paragraph (§5.5).

An upper cap was added to the top of the existing cap to maintain the position of the outgoing tubes and avoid any movement of the microreactor during the replacement of the syringes. It also improved the contact between the aluminum screen and the oven, and between the contact pin and the membrane, by applying a small mechanical force on the microreactor.

The effects of these different modifications are described in the following paragraphs.

5.3.2.1 Influence of the contact pin and the heat carrier layer

The effect of the contact pin and the heat carrier layer on the sensitivity of the system is shown in Figure 5-5. These results were obtained using the H_2SO_4 /NaOH calibration reaction.

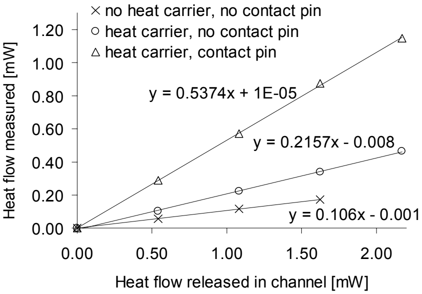

Figure 5-5: Improvements made to the sensitivity of the system by adding a heat carrier layer and a contact pin.

The addition of a heat carrier layer (PEG 300) directly on top of the membrane doubled the thermal efficiency of the system by eliminating the air layer above the microcalorimetric membrane. The thermal efficiency was further increased by up to 53 % by using a contact pin which reduced the heat losses in the non-sensitive part of the membrane. As stated in chapter 3, the contact pin was made of alumina. However, no significant effect of the pin material was observed since tests performed with a contact pin made of aluminum instead of alumina showed a comparable efficiency.

The combined addition of a contact pin and a heat carrier layer multiplied the thermal efficiency of the system by a factor of more than five and, therefore, very significantly improved the heat transfer from the microchannel to the sensor.

5.3.2.2 Influence of the upper cap, vertical positioning of the reactor on sensors

The upper cap, originally added to maintain the positioning of the outgoing tubes, showed an influence on the thermal efficiency. This cap was screwed to the heat sink of the calorimeter and important variations were observed depending on the strength of its fixation.

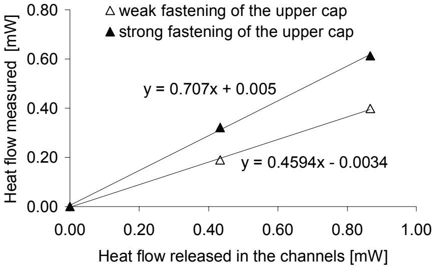

Figure 5-6: Influence of the strength of the fastening of the upper cap on the thermal efficiency of the system.

As shown in Figure 5-6, the amount of heat transferred increased when the upper cap was firmly fixed. Actually the mechanical pressure applied on the tubes decreased the distance between the microreactor and the calorimetric membrane. The typical thermal efficiencies measured varied between 70% and 80%. The results shown in Figure 5-6 for a weak fixation of the upper cap are not directly comparable to the ones presented in Figure 5-5 because a novel microreactor was installed in this case.

An important point to note from this experiment is that once the microreactor is installed and the calibration is performed, the position of the upper cap, i.e. its strength of fixation, should not be modified.

The combined effect of the upper cap, the contact pin and the heat carrier layer made it possible to increase the thermal efficiency of the system from 10 % to 70 % or more. The latter is mostly governed by the improvement of the quality of thermal contact between the reactor and the sensors. In order to examine this aspect more closely, a heat flow balance of the microcalorimetric system was performed and is presented in the next section.

5.4 HEAT FLOW BALANCE

To better evaluate the individual contribution of the different parts of the system, a heat flow balance is required.

The mathematical program FEMLAB presented in chapter 4 was first used to try to simulate the thermal exchanges in the microreactor-based calorimetric system. For these simulations, the geometry of the calorimetric cavity should be simplified and represented in two dimensions. However a 2-D representation of the cavity did not allow to accurately model the thermal profile effectively established in our three dimensional cavity. The computation of a three dimensional geometry became highly complex and this approach was quickly abandoned.

As the entire system is too complex to be modeled, a simplified balance defining the major resistances to heat transfer is proposed.

As explained in subsection §5.2.2, the heat released in the reaction channel flows to the calorimetric membrane on one hand and directly to the oven on the other hand. These heat flows can be characterized using the resistance to heat transfer on each path.
Three resistances were defined to achieve a global description of the system (Figure 5-7):

- the resistance of the integrated circuit (calorimetric membrane) called R_{IC},
- the resistance due to the heat transfer from the reaction channel to the sensors called $R_{contact}$,
- the resistance due to the various losses (air convection, heat accumulation in the outlet flow, heat conduction in the stainless steel tube and in the non-sensitive part of the membrane) called R_{loss}.

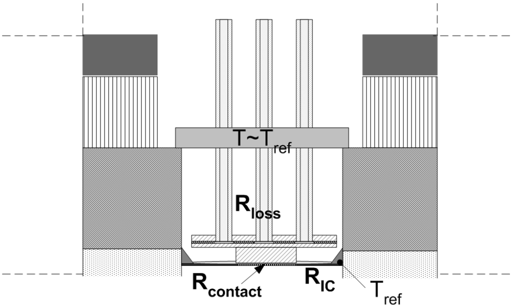

Figure 5-7: Drawing of the calorimetric cavity - Heat flow balance.

Using these resistances, the heat transfer can be schematically drawn as shown in Figure 5-8.

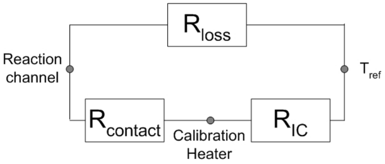

Figure 5-8: Scheme of the heat transfer in the calorimetric system in terms of resistances.

To estimate the three unknown resistances, three different experiments were performed using the different types of calibrations described in section §5.2. The calculations are detailed in Appendix A, at the end of the chapter but the most important expressions are summarized in the following subsections.

5.4.1 Heat source on the chip: calibration using the heater resistance

A Joule effect was applied in the center of the membrane first with an empty cavity, i.e. with no microreactor in place, and then with the microreactor introduced into the cavity. The output voltage measured in each case was compared to the heat flow applied. The respective sensitivities S_{q0}^{hr} and S_{q}^{hr} were determined. The ratio of these sensitivities can be expressed as:

$$\frac{S_q^{hr}}{S_{q0}^{hr}} = \frac{R_{contact} + R_{loss}}{R_{IC} + R_{contact} + R_{loss}} \tag{5.5}$$

The mathematical development leading to equation (5.5) is detailed in Appendix A. The sensitivity obtained was 1500 µV·mW^{-1} for the empty cavity (S_{q0}^{hr}) and 1080 µV·mW^{-1} for the entire system (S_{q}^{hr}) (Figure 5-9).

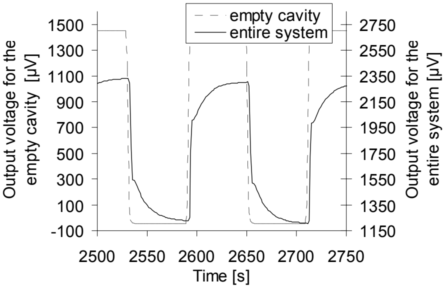

Figure 5-9: Comparison of the sensitivity with and without a microreactor in the calorimetric cavity.

The resistance of the integrated circuit R_{IC} can be calculated from the sensitivity of the empty cavity using equation (5.22) in Appendix A. This gives us $\boldsymbol{R_{IC}} = \mathbf{21.4\ K{\cdot}W^{-1}}$.

The sum ($R_{loss} + R_{contact}$) can then be estimated from equation (5.5) and is equal to 55 K·W^{-1}.

5.4.2 Heat source in the reaction channel: calibration using a chemical reaction

In this case, the neutralization of H_2SO_4 by NaOH was performed in the microchannel and the corresponding output voltage was measured. For this experiment, the flow rates of the feed streams were varied from 4 to 16 µl·min^{-1}. The concentrations used for H_2SO_4 and NaOH were 0.6 mol·l^{-1}.

The sensitivity obtained in this case S_q^{rx} can be compared to the previous one S_q^{hr}:

$$\frac{S_q^{rx}}{S_q^{hr}} = \left(\frac{R_{loss}}{R_{contact} + R_{loss}} \right) \tag{5.6}$$

Since the sum ($R_{loss} + R_{contact}$) is known from the first calculation, R_{loss} can be estimated and thus compared to $R_{contact}$.

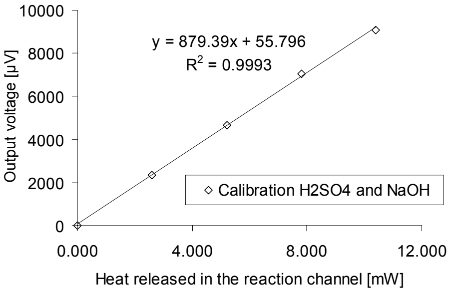

Figure 5-10: Determination of the sensitivity of the system for a heat source in the reaction channel – Calibration reaction with flow rates varying from 4 to 16 µl·min^{-1} and initial concentrations of 0.6 mol·l^{-1}, T=40°C.

The sensitivity S_q^{rx} determined by this method was 879 µV·mW^{-1} (Figure 5-10). The value of the contact resistance and the loss resistance can be deduced from equation (5.6), giving $R_{contact}$ **= 11 K·W^{-1}** and R_{loss} **= 44 K·W^{-1}**.

5.4.3 Remarks on the heat flow balance

The establishment of this simplified heat flow balance and especially the values of loss resistance and contact resistance lead to several observations.

First of all, the contact resistance is significantly lower than the loss resistance. The main part of the heat released in the channel is thus measured. In an ideal case, the loss resistance should tend to infinite and the contact resistance to zero.

The remaining loss sources and limits for the heat transfer are discussed in the next subsections by analyzing the different contributions to the loss and contact resistances.

Loss resistance

The linearity of the calibration curve (Figure 5-10) shows that there is no variation of the loss resistance with the flow rates and the concentrations. This would not be the case if heat accumulation in the outgoing fluid occurred. Isothermal conditions are thus achieved in the range of flow rates and concentrations tested.

Further developments with regard to the contribution of the heat conduction through the tubes are presented in chapter 6. These developments revealed that the tubes resistance was high compared to the loss resistance estimated with this heat flow balance. The conduction through the tube is thus not an important source of heat losses.
Since it appears that the contribution of both the heat accumulation in the outgoing fluid and the heat conduction through the tube are small, the main part of the remaining heat lost is probably due to heat transfer to the non-sensitive part of the membrane. We will come back to this point at the end of this subsection.

Contact resistance

The resistance to thermal diffusion through the polyethylene glycol layer can be estimated as a first approximation of the contact resistance. As this glycol layer is thin (ca. 50 μm), natural convection cannot develop and a purely conductive mechanism can be assumed.

The resistance in this heat carrier layer can be evaluated as follows assuming a purely conductive mechanism:

$$R_{heat\ carrier} = \frac{\delta}{\lambda \cdot A} \approx R_{contact} \tag{5.7}$$

Assuming a thickness of 50 μm for the PEG 300 layer, with a contact area of 16 mm^2 and given that the thermal conductivity of polyethylene glycol is 0.23 W·m^{-1}·K^{-1} at 25 °C, the resistance is 13.6 K·W^{-1}. This value is close to the experimental value of 11 K·W^{-1} determined for the contact resistance, which confirms that the limiting factor for the heat transfer in this area is the resistance of the heat carrier. This also explains why the material of the contact pin did not affect the efficiency of the system.
Moreover, equation (5.7) shows a linear relationship between the thickness of the heat carrier layer and the contact resistance. The lower the thickness of the heat carrier, the lower is the contact resistance. This explains the observation made in subsection §5.3.2.2, i.e. the mechanical force applied via the upper cap tends to reduce the thickness of the layer and thus lowers the resistance.

The time constant for thermal diffusion in the heat carrier layer can be roughly estimated from:

$$t = R_{heatcarrier} \cdot m \cdot C_p \tag{5.8}$$

Given that C_p is 2 kJ·kg^{-1}·K^{-1}, and assuming that the mass of PEG is 0.1 g, the time constant is close to 3 s. This time is much longer than the time required for the lateral distribution in the alumina plate of the microreactor (estimated using the same method as 50 ms). The thermal equilibrium is therefore already achieved along the base of the microreactor, when the heat released in the reaction channel reaches the sensors. The position of the reaction channel on the base of the microreactor will therefore not influence the thermal efficiency of the system and should not be restricted to the area overlaying the contact pin, i.e. the sensors. This observation allows the construction of the microchannel of design 4 (see chapter 3).

The time for thermal diffusion is also much longer than the time for the lateral distribution in the microcalorimetric membrane (around 10 ms). This is, however, not a limiting point since all measurements are made at steady state.

In conclusion, the heat carrier layer is the limiting point for the heat transfer; it is the main contribution to the contact resistance due to the slow heat transfer through this layer.

Moreover, since the heat carrier layer cannot be exclusively placed above the sensitive part of the microcalorimetric membrane, this layer also directs part of the heat flow to the non-sensitive part of the membrane. This is the main source of heat lost.

5.5 THE FEED STREAMS PREHEATING

5.5.1 Importance of the feed preheating

The reactant solutions may be at a different temperature from the temperature of the oven. In this case, their introduction into the calorimetric cavity induces a sensible heat. This sensible heat should be systematically calibrated for the different flow rates used.

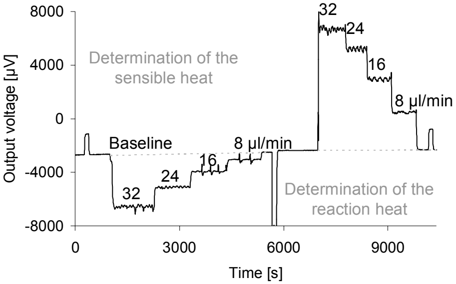

Figure 5-11: Example of the importance of the determination of the sensible heat - Calibration reaction (H_2SO_4 + NaOH) at high flow rates, T=40°C.

As can be seen from Figure 5-11, the determination of the sensible heat doubles the duration of the experiment. Moreover, an additional source of error can be introduced into the results due to the difference in calorific capacity between the solvent used for the calibration and the reaction mixture. This correction of the sensible heat can be avoided for the calibration reaction by varying the concentration of the reactant instead of the flow rates (as shown in Figure 5-3).

However, the possibility of working at variable flow rates, i.e. various residence times, is a crucial point for the determination of reaction kinetics (see chapter 6).

5.5.2 Influence of the aluminum screen

As stated earlier, the aluminum screen, glued to the inlet and outlet tubes, is slightly larger than the calorimetric cavity so that it rests on the oven. This forms a thermal bridge which slightly preheats the tubes and thus the microreactor. The effect of this screen can be observed in two main ways:

- The baseline position,
- The sensible heat measured.

5.5.2.1 On the baseline position

The influence of the aluminum screen on the baseline was tested by varying the temperature of the oven. The microreactor was filled with water and the flow rate was then set to zero.

At steady state, the baseline is ideally expected to be close to zero. However, if the temperature of the microreactor stays below the oven temperature, an endothermic signal is observed. As can be seen from Figure 5-12, without the aluminum screen the temperature of the microreactor never reaches the oven temperature and the baseline is negative. However, when an aluminum screen is added, a slightly exothermal signal is observed.

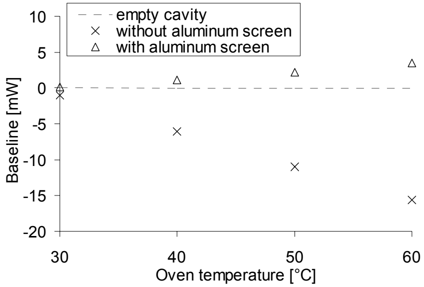

Figure 5-12: Influence of the aluminum screen on the position of the baseline at different oven temperatures – microreactor filled with water, no flow rate applied.

Thus the introduction of the aluminum screen has a major effect on the temperature of the microreactor. Actually, the temperature of the microreactor is slightly higher than the oven temperature. This can be explained by a heterogeneous distribution of the temperature in the oven. The upper side of the oven which is directly in contact with the Peltier elements seems to be at a slightly higher temperature than the lower side in contact with the reference. This temperature difference can be estimated as 0.05 °C at the highest temperature tested (60 °C) and will not influence the determination of kinetics.

If this baseline increase is effectively due the inhomogeneous temperature across the oven, the temperature achieved by the microreactor should be dependent of the quality of the thermal contact between the aluminum screen and the top of the oven. In the subsection §5.3.2.2, the strength of fastening of the upper cap showed an influence on the quality of contact between the microreactor and the calorimetric membrane due the vertical mechanical force applied to the microreactor. This should also have an influence on the contact between the aluminum screen and the oven as the aluminum screen is glued to the microreactor. This was tested and the results are reported in Figure 5-13.

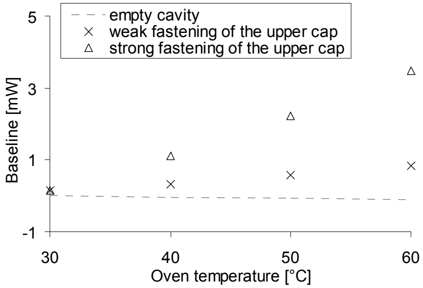

Figure 5-13: Influence of the strength of fastening of the upper cap on the baseline position – microreactor filled with water, no flow rate applied.

Figure 5-13 shows that the strength of fastening of the upper cap has an important influence on the baseline position. This result confirms that the baseline increase is due to a slight temperature difference between the top and the bottom of the oven. This is also in agreement with the observation of a higher baseline increase when a conductive paste is added between the aluminum screen and the oven (results not shown).

5.5.2.2 On the sensible heat

It was observed in the previous paragraph that the introduction of the aluminum screen allowed preheating the microreactor at a temperature even slightly higher than the oven temperature. This investigation was however performed without applying a flow through the channel and the effective influence of the aluminum screen on the preheating of the entering fluids could therefore not be assessed.

The influence of the aluminum screen on the sensible heat measured was determined by using different flow rates of water at 25 °C in the oven at a temperature of 40 °C.

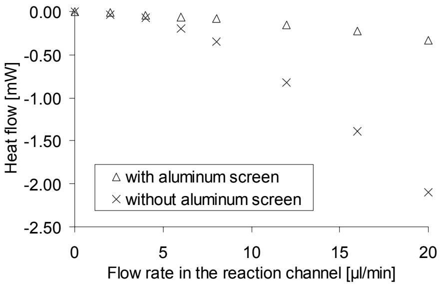

Figure 5-14: Influence of the aluminum screen on the preheating of the entering water at 25 °C in the oven at 40 °C.

As seen in Figure 5-14, the introduction of the aluminum screen resulted into a significant preheating of the entering fluids even at a flow rate in the reaction channel of 20 $\mu l \cdot min^{-1}$.

However, at higher temperatures and higher flow rates, the aluminum screen did not provide sufficient preheating and a calibration of the sensible heat was therefore required. Moreover, as described in subsection §5.5.2.1, the efficiency of the preheating obtained with this method was highly dependent on the quality of the contact between the oven and the screen and varied each time a different microreactor was installed.

In conclusion, the aluminum screen, in addition to its role for the vertical positioning of the microreactor, allows to slightly preheat the fluids and reduces significantly the sensible heat measured. However, a reliable and reproducible method is required to ensure a well-controlled preheating of the entering fluids especially when working with reactions with weak heat flows. The next paragraph describes the technique chosen for this work: the introduction of an electrical preheating layer.

5.5.3 Introduction of an electrical preheating layer

The last major modification made to the microreactor-based calorimetric system was the introduction of an electrical preheating layer. This layer was added on top of the aluminum screen as shown in Figure 5-15.

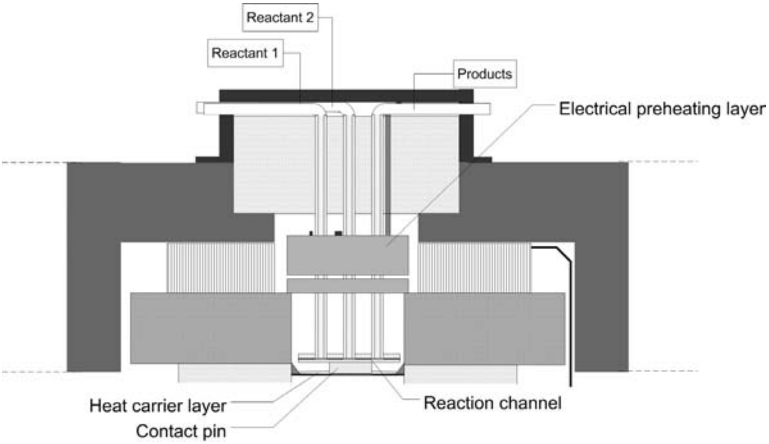

Figure 5-15: Final configuration of the microcalorimetric system – Introduction of an electrical preheating layer.

As mentioned in chapter 3, this preheating layer is made of two different layers: an alumina layer on which two resistances are deposited by silk-screen printing (one to heat the plate and the other to measure the temperature reached) and an aluminum block of 4 mm depth glue-bonded to the alumina plate. The addition of the thick aluminum block distributed the heat generated by the heating resistance vertically and thus increased the contact surface with the tubes.

Following an approach similar to the one described in subsection §5.5.2.2, water at 25 °C was introduced at various flow rates into the oven heated at 55 °C and the resulting sensible heat was measured. The results are shown in Figure 5-16 and are compared with the results obtained solely with the aluminum screen.

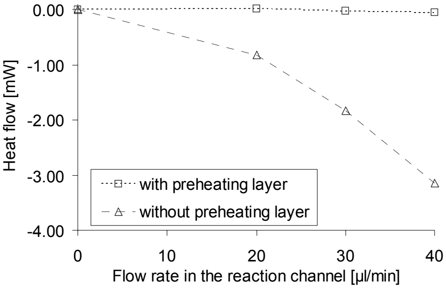

Figure 5-16: Influence of the electrical preheating layer on the preheating of the entering water at 25 °C in the oven at 55 °C.

As shown in Figure 5-16, at the highest flow rates tested, the sensible heat was entirely compensated when the preheating layer was switched on. No baseline corrections were therefore required when the flow rates were varied.

However, this electrical preheating layer obviously does not allow the cooling of the entering fluids when working at temperatures below ambient. In this case, only the aluminum screen ensures the thermal conditioning of the fluids.

For temperatures above ambient, this improvement significantly reduced the experimental time required, simplified the data analysis and increased the precision of the data.

5.6 REPEATABILITY OF THE SYSTEM

In the previous sections, the thermal efficiency of the system was determined. It was explained that this efficiency would be used as a correction factor in subsequent experiments. In addition the duration of the experiments could be reduced by shielding the system against external influences. However, all these points are irrelevant if we cannot guarantee that the signal given by the calorimetric system is repeatable and reliable and that the correction factor does not vary with time. This key topic is presented in the following subsection.

At first, the repeatability of the system was checked by performing the calibration reaction several times. The oven temperature was set at 35 °C. The microreactor was neither changed nor moved during the duration of the experiment. Nine experiments were carried out varying the concentration of NaOH and H_2SO_4 (0, 0.1, 0.2, 0.3 and 0.4 mol·l^{-1}) and the flow rates (2 µl·min^{-1}, 4 µl·min^{-1} and 6 µl·min^{-1}). This series of experiments was repeated over a week to assess the repeatability over time. An average deviation of 3 % was observed between the nine experiments (see Figure 5-17).

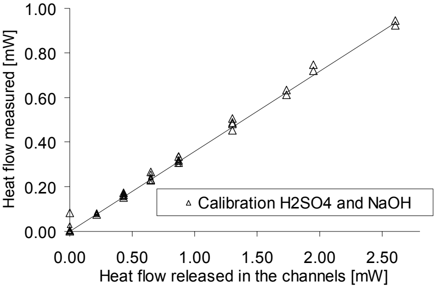

Figure 5-17: Calibration reaction of H_2SO_4 with NaOH at flow rates varying from 2 to 6 µl·min^{-1} and initial concentrations varying from 0.1 to 0.4 mol·l^{-1}, T=40°C.

As can be seen from Figure 5-17, the thermal efficiency determined in the different experiments was found to be constant and no systematic variation over time was observed. This study was performed before the introduction of the upper cap, which explains why the thermal efficiency values obtained were lower that the ones presented in subsection §5.3.2.2.

In a second step, the reproducibility was tested by changing the reaction. The standard calibration reaction was replaced by the neutralization of hydrochloric acid by sodium hydroxide (see (II)) which shows a different reaction enthalpy.

$$HCl + NaOH \rightarrow H_2O + NaCl \tag{II}$$

The thermal efficiency determined in Figure 5-17 was used as correction factor to deduce the reaction enthalpy of this neutralization.

Combining (5.3) with (5.4), one can find that:

$$\frac{\dot{q}_{meas}}{F} = \dot{V} \cdot (-\Delta H_r) \cdot c_0 \cdot X \tag{5.9}$$

The slope of the plot of the corrected heat flow versus the molar flow rate ($\dot{q}_{measured}/F = \mathrm{f}\,(\dot{V} \cdot c_0)$) gives the enthalpy of reaction.

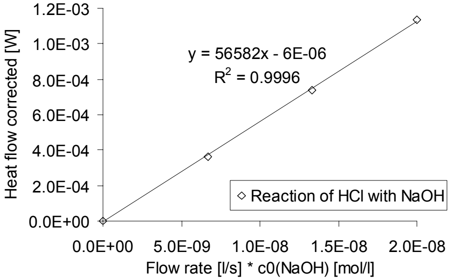

Figure 5-18: Determination of the enthalpy of reaction of the neutralization of HCl by NaOH for initial concentration of 0.1 and 0.2 mol·l^{-1} and flow rates of 4 and 6 µl·min^{-1}, T=40°C.

The enthalpy of reaction found with this technique was -56.6 kJ·mol^{-1} and is close to the value reported in the literature -57.4 kJ·mol^{-1} [88]. The results obtained with the system are thus reliable.

5.7 CONCLUSIONS

The critical success factors for an improved efficiency of the calorimetric measurements were found to be: the use of a contact pin to focus the flow on the sensitive area of the sensor, the use of a heat carrier layer to remove the air layer on the contact surface and finally the combined action of an aluminum screen, glued to the inlet and outlet tubes, and of an upper cap to position the microreactor relative to the sensor.

These modifications in the design of the microreactor increased the thermal efficiency of the calorimetric system from 10 % up to 70-80 %. The heat balance of the system showed that the limiting part for the heat transfer was still the contact between the microreactor and the calorimetric membrane and in particular the transfer through the heat carrier layer.

Besides efficiency improvements, the introduction of an electrical preheating layer ensured the preheating of the fluids at temperatures up to 55 °C. Under these conditions, the sensible heat was entirely compensated and no baseline corrections were required when the flow rates were changed. The conditioning of the fluids at temperatures above ambient was partially obtained by the aluminum screen mentioned above that rests on the top of the calorimetric cavity and forms a thermal bridge above the oven.

The modified system showed good repeatability and the determination of the enthalpy of reaction of a well-known reaction showed a margin of error not exceeding 2 %.

5.8 APPENDIX A

5.8.1 Heat source on the chip: Calibration using the heater resistance

Applying a Joule effect of $\dot{q}$ =1mW, the sensitivity is defined as:

$$S_q^{hr} = \frac{U_{meas}^{hr}}{\dot{q}_{hr}} \tag{5.10}$$

Empty cavity. Without microreactor, the heat flow generated by the heater resistance $\dot{q}_{hr}$ can be divided in two parts:

$$\dot{q}_{hr\,0} = \dot{q}_{meas\,0}^{hr} + \dot{q}_{loss\,0}^{hr} \tag{5.11}$$

where $\dot{q}_{loss\,0}^{hr}$ is the heat flow lost by natural convection in the air contained in the oven and is equal to:

$$\dot{q}_{loss\,0}^{hr} = \left(\frac{1}{R_{air}}\right) \cdot \Delta T \tag{5.12}$$

Where ΔT is the temperature difference between the heat source and the reference and $\dot{q}_{meas\,0}^{hr}$ is the heat flow measured by the IC membrane:

$$\dot{q}_{meas\,0}^{hr} = \left(\frac{1}{R_{IC}}\right) \cdot \Delta T \tag{5.13}$$

Because the resistance of the air is high compared to the resistance of the integrated circuit, the equation (5.11) can be simplified to:

$$\dot{q}_{hr0} = \dot{q}_{meas\,0}^{hr} \tag{5.14}$$

Entire system. With the microreactor and the heat carrier layer, the contribution of the resistances can be approximated as shown in Figure 5-19.

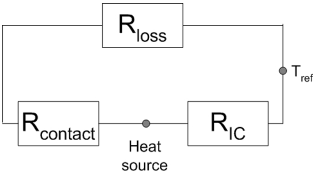

Figure 5-19: Scheme of the resistance contributions for the entire system with a heat source on the chip.

In this case, the heat flow lost is equal to:

$$\dot{q}_{loss}^{hr} = \left(\frac{1}{R_{contact} + R_{loss}} \right) \cdot \Delta T \tag{5.15}$$

This gives:

$$\dot{q}_{hr} = \left(\frac{1}{R_{IC}} + \frac{1}{R_{contact} + R_{loss}} \right) \cdot \Delta T \tag{5.16}$$

Rearranging equation (5.16),

$$\dot{q}_{hr} = \left(\frac{R_{contact} + R_{loss} + R_{IC}}{R_{IC} \cdot \left(R_{contact} + R_{loss} \right)} \right) \cdot \Delta T \tag{5.17}$$

or:

$$\dot{q}_{hr} = \left(\frac{R_{contact} + R_{loss} + R_{IC}}{R_{contact} + R_{loss}} \right) \cdot \left(\frac{\Delta T}{R_{IC}} \right) \tag{5.18}$$

The expression of the heat flow measured $\dot{q}_{meas}^{hr}$ becomes then:

$$\dot{q}_{meas}^{hr} = \dot{q}_{hr} \cdot \left(\frac{R_{contact} + R_{loss}}{R_{IC} + R_{contact} + R_{loss}} \right) \tag{5.19}$$

Combining (5.14) and (5.19), we obtain:

$$\frac{\dot{q}_{meas}^{hr}}{\dot{q}_{meas\,0}^{hr}} = \frac{U_{meas}^{hr}}{U_{meas\,0}^{hr}} = \frac{\dot{q}_{hr}}{\dot{q}_{hr0}} \cdot \left(\frac{R_{contact} + R_{loss}}{R_{IC} + R_{contact} + R_{loss}} \right) \tag{5.20}$$

The ratio of the measured sensitivities is then:

$$\boxed{\frac{S_q^{hr}}{S_{q0}^{hr}} = \frac{U_{meas}^{hr} / \dot{q}_{hr}}{U_{meas\,0}^{hr} / \dot{q}_{hr0}} = \frac{R_{contact} + R_{loss}}{R_{IC} + R_{contact} + R_{loss}}} \tag{5.21}$$

R_{IC} can be estimated by the following relation:

$$S_{q0}^{hr} = (N_{th} \cdot \alpha_{th}) \cdot R_{IC} \tag{5.22}$$

The term ($N_{th} \cdot \alpha_{th}$) described in chapter 2 corresponds to the temperature coefficient of the calorimetric membrane and is equal to 0.07 V·K^{-1} [19].

The sum (R_{loss} + $R_{contact}$) can then be obtained using (5.21).

5.8.2 Heat source in the reaction channel: calibration using a chemical reaction

In this case, the contribution of the contact resistance changes (see Figure 5-20).

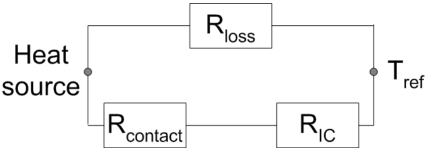

Figure 5-20: Scheme of the resistance contributions for the entire system with a heat source in the channel.

The sensitivity is then defined as:

$$S_q^{rx} = \frac{U_{meas}^{rx}}{\dot{q}_{rx}} \tag{5.23}$$

The heat released in the channel due the chemical reaction $\dot{q}_{rx}$ can be divided in two parts:

$$\dot{q}_{rx} = \dot{q}_{meas}^{rx} + \dot{q}_{loss}^{rx} \tag{5.24}$$

where $\dot{q}_{loss}^{rx}$ is the heat flow lost equal to:

$$\dot{q}_{loss}^{rx} = \left(\frac{1}{R_{loss}} \right) \cdot \Delta T \tag{5.25}$$

and $\dot{q}_{meas}^{rx}$ is the heat flow measured by the calorimetric membrane:

$$\dot{q}_{meas}^{rx} = \left(\frac{1}{R_{contact} + R_{IC}} \right) \cdot \Delta T \tag{5.26}$$

From (5.24), (5.25) and (5.26) we can derive:

$$\dot{q}_{meas}^{rx} = \dot{q}_{rx} \cdot \left(\frac{R_{loss}}{R_{contact} + R_{IC} + R_{loss}} \right) \tag{5.27}$$

and combining (5.19) with (5.27),

$$\frac{\dot{q}_{meas}^{rx}}{\dot{q}_{meas}^{hr}} = \frac{U_{meas}^{rx}}{U_{meas}^{hr}} = \frac{\dot{q}_{rx}}{\dot{q}_{hr}} \cdot \left(\frac{R_{loss}}{R_{contact} + R_{loss}} \right) \tag{5.28}$$

Comparing the sensitivity S_q^{rx} obtained in this case with the one obtained in the previous paragraph S_q^{hr}:

$$\frac{S_q^{rx}}{S_q^{hr}} = \frac{U_{meas}^{rx} / \dot{q}_{rx}}{U_{meas}^{hr} / \dot{q}_{hr}} = \frac{R_{loss}}{R_{contact} + R_{loss}} \tag{5.29}$$

Knowing the sum (R_{loss} + $R_{contact}$) from the first calculation and knowing R_{IC}, R_{loss} can be estimated and thus compared to $R_{contact}$.

Chapter 6

DETERMINATION OF REACTION KINETICS

6.1 INTRODUCTION

In Chapter 5, the novel calorimetric system was calibrated using a neutralization reaction and its thermal efficiency was improved by several modifications of the microreactor design.

The present chapter is dedicated to the determination of reaction kinetics with the final configuration of the microsystem.

FEMLAB-based simulations are first presented to check the suitability of the microchannel-based system for the determination of reaction kinetics and to assess the influence of the mixing time of the reactants on the resulting conversion at the end of the channel.

After a theoretical explanation of the way of deducing kinetics from the raw data of the calorimeter, the applicability of this novel system for the assessment of kinetics is proven by characterizing a model reaction well described in literature. This allows validating the system in the region of specific heat flows ranging from 50 to 200 $W \cdot kg^{-1}$.

In the second part of this chapter, the application of this system to reactions generating high heat flow is investigated. The expected range of heat flows providing isothermal conditions in the microchannels is first estimated using finite element modeling. Kinetics studies of the reaction of two unsaturated ethers with an acidic solution of methanol are then presented. The latter involves heat flows up to 160'000 $W \cdot kg^{-1}$. The advantages of the use of the temperature-scanning mode are also discussed using the same reaction.

The limits of the current system in terms of kinetic determination are finally identified and discussed.

6.2 CFD SIMULATIONS: KINETICS OF A REACTION IN THE MICROCHANNEL

CFD simulations were first performed with the mathematical program FEMLAB presented in chapter 4 to illustrate the experimental results and to check the suitability of the microchannel for the determination of reaction kinetics.

The reaction of ethyl acetate 0.8 mol·l^{-1} with NaOH 1.0 mol·l^{-1} was computed[3].
The predicted variation of the ethyl acetate concentration along the channel is represented in Figure 6-1a for a linear velocity of the feed streams of $9.33 \cdot 10^{-4}$ m·s^{-1} (corresponding to 1.4 µl·min^{-1}) and a temperature of 70 °C.

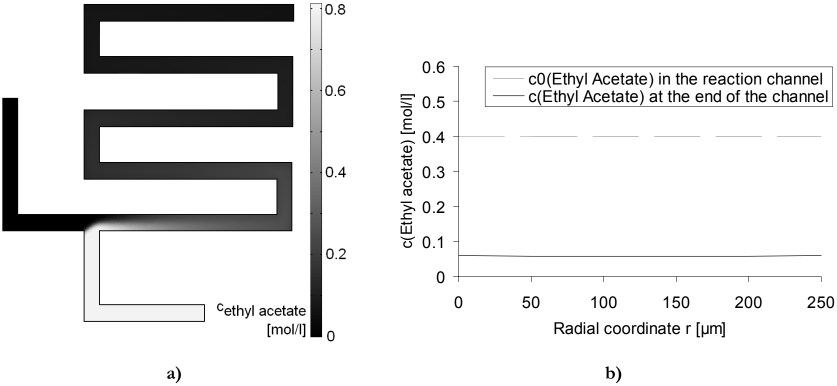

Figure 6-1: Simulation of the reaction of ethyl acetate 0.8 mol·l^{-1} with NaOH 1.0 mol·l^{-1} with linear velocities at the inlets of $9.33 \cdot 10^{-4}$ m·s^{-1}, T=70 °C. a) Concentration of ethyl acetate along the channel, b) cross plot section at the end of the channel.

In Figure 6-1b, a cross-section plot of the concentration of ethyl acetate at the end of the reaction channel is represented. The concentration of ethyl acetate calculated is compared to the initial concentration in the channel. This allows calculating the conversion achieved at the end of the channel.

By varying the inlet velocities, the conversion can be calculated for various residence times. One can check that the conversions predicted by simulation are similar to those simply calculated from the expression of the reaction rate without taking the geometry into account (using the same kinetic parameters).

---

[3] This reaction is used as a model reaction in §6.3.2 for the experimental validation of the microreactor-based calorimetric system.

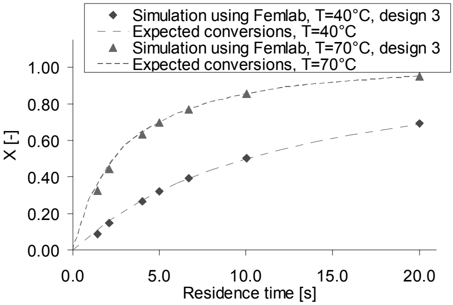

Figure 6-2: Simulations of the conversion at the end of the channel at T=40 °C and T=70 °C. Comparison with the one predicted without taking the geometry into account.

As seen in Figure 6-2, both calculations correlate well. Thus there is no influence of the flow established in the microchannel on the evaluation of the reaction kinetics. According to these predictions, the mixing time does not influence the results.

Computations performed with faster reactions did not converge due to saturation of the computer's memory used for simulations.

6.3 VALIDATION OF THE CALORIMETRIC SYSTEM USING A SIMPLE MODEL REACTION

6.3.1 Interpretation of the raw data of the microsystem

6.3.1.1 Determination of the enthalpy of reaction

For the determination of reaction kinetics, the first step is to measure the enthalpy of reaction. This is achieved by choosing temperature and concentration conditions ensuring complete conversion at the end of the channel.

As explained in chapter 5, the heat flow measured can be written as follows:

$$\frac{\dot{q}_{measured}}{F} = \dot{V} \cdot c_0 \cdot (-\Delta H_R) \cdot X = \dot{N} \cdot X \cdot (-\Delta H_R) \qquad (6.1)$$

F is the correction factor. The determination of this factor is described in Chapter 5. From equation (6.1) one can deduce that for X=1, the slope of the plot of the corrected heat flow versus the molar flow rate ($\dot{q}_{measured}/F$ =f($\dot{V} \cdot c_0$)=f($\dot{N}$)) gives the enthalpy of reaction. The enthalpy of reaction can thus be determined either by maintaining the concentration constant and varying the flow rate or inversely by maintaining the flow rate constant and varying the concentration.

6.3.1.2 Determination of the enthalpy of mixing

The enthalpy of mixing of two non-reactive fluids can simply be determined as described in the previous subsection by applying equation (6.1).
This is done for example in subsection §6.4.2.2 to determine the heat of mixing of the solvent used to dilute ether A with another solvent, methanol.

This determination gets more complicated when a reaction is involved. The heat measured is then a combination of the mixing and reaction enthalpies. The distinction between the heat due to mixing and the heat due to the reaction is difficult to achieve. The global heat flow measured can then be written as follows:

$$\dot{q}_{measured} = F \cdot \dot{V} \cdot c_0 \cdot \left[(-\Delta H_R) \cdot X + (-\Delta H_{mixing})\right] \tag{6.2}$$

However, as the mixing phenomenon is often faster than the reaction, the heat of mixing can be estimated by working at low residence times (high flow rates) to decrease the contribution of the enthalpy of reaction. The heat flow measured tends then to:

$$\dot{q}_{measured} \approx F \cdot \dot{V} \cdot c_0 \cdot (-\Delta H_{mixing}) \tag{6.3}$$

The value obtained should however only be used as an estimate because the contribution of the enthalpy of reaction is never entirely removed.
This is one of the major limitation of the system (see section §6.6).

6.3.1.3 Determination of the conversion achieved at the end of the channel

When a reaction is not completed at the end of the channel, the conversion rate can be simply calculated using equation (6.1) and knowing the enthalpy of reaction:

$$X = \frac{\dot{q}_{measured}}{F \cdot \dot{V} \cdot (-\Delta H_R) \cdot c_0} \tag{6.4}$$

As presented above with the CFD simulations (section §6.2), the variation of the flow rate allows calculating the conversion at the end of the channel at various residence times in the microchannel.

For a reaction with a mixing enthalpy, this equation becomes:

$$X = \frac{\dot{q}_{measured} - F \cdot \dot{V} \cdot (-\Delta H_{mix}) \cdot c_0}{F \cdot \dot{V} \cdot (-\Delta H_R) \cdot c_0} \tag{6.5}$$

Thus a poorly-characterized mixing enthalpy affects significantly the assessment of the conversion of the reaction.

6.3.1.4 *Determination of the kinetic constant k*

The calculation of the kinetic constant k depends obviously of the order of reaction. In the following paragraph the equations needed for the calculation of k are derived for reactions kinetics of first and second order. These derivations are explained in more details by Levenspiel [89].

For a first order reaction

The rate equation can be written as follows:

$$\frac{dc_A}{dt} = k_1 \cdot c_A \tag{6.6}$$

Equation (6.6) can be rewritten in terms of conversion giving:

$$c_{A0} \cdot \frac{dX}{dt} = k_1 \cdot c_{A0} \cdot (1 - X) \tag{6.7}$$

The integration of the equation (6.7) allows the calculation of k_1 using the following expression:

$$\boxed{k_1 = -\frac{1}{t} \cdot \ln(1 - X)} \tag{6.8}$$

For a second order reaction

The rate equation of a second order reaction involving two species A and B can be written:

$$\frac{dc_A}{dt} = k_2 \cdot c_A \cdot c_B \tag{6.9}$$

Supposing that the amounts of A and B are not always added in stoechiometric proportions,

$$c_{A0} \cdot \frac{dX}{dt} = k_2 \cdot (c_{A0} - c_{A0} \cdot X) \cdot (c_{B0} - c_{A0} \cdot X) \tag{6.10}$$

Letting $M = c_{B0}/c_{A0}$ and after simplification, equation (6.10) becomes:

$$\frac{dX}{dt} = k_2 \cdot c_{A0} \cdot (1 - X) \cdot (M - X) \tag{6.11}$$

which after integration and simplification gives,

$$\frac{1}{1 - M} \cdot \ln\left(\frac{M - X}{M \cdot (1 - X)} \right) = c_{A0} \cdot k_2 \cdot t \tag{6.12}$$

or

$$\boxed{k_2 = -\frac{1}{(c_{B0} - c_{A0}) \cdot t} \cdot \ln\left(\frac{1 - X}{1 - (c_{A0}/c_{B0}) \cdot X} \right)} \tag{6.13}$$

6.3.1.5 Determination of the energy of activation and of the pre-exponential term

The temperature dependency of the rate constant can be written as follows,

$$k = k^0 \cdot \exp\left(\frac{-E_a}{R \cdot T}\right) \tag{6.14}$$

The linearization of the equation (6.14) gives:

$$\ln k = \ln k^0 - \frac{E_a}{R \cdot T} \tag{6.15}$$

The slope of the plot of $\ln k = f(1/T)$ allows the determination of the activation energy E_a and the ordinate at the origin provides the frequency factor k^0.

6.3.2 Validation using the saponification of ethyl acetate in alkaline solution

The saponification of ethyl acetate in alkaline solution was selected as model reaction for the validation of the novel calorimetric system (see (I)). This reaction is fairly fast, exothermal and well-described in literature [34, 90-94]. Moreover, no mixing enthalpy is reported. The reaction kinetics is of second-order.

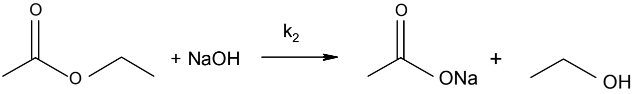

(I)

Ethyl acetate is diluted in water to obtain the various concentrations used. As ethyl acetate slowly hydrolyzes at room temperature, fresh solutions have to be used for each experiment. The alkaline solutions are obtained by dilution in water of a standard 1 mol·l^{-1} NaOH solution.

6.3.2.1 Determination of the enthalpy of reaction

In order to ensure that the reaction is complete at the end of the channel, ethyl acetate 0.1 mol·l^{-1} is mixed with NaOH 1 mol·l^{-1} at 40 °C. The longest microchannel (design 4, length of 44 mm) was used to increase the residence times. As explained in subsection §6.3.1.1, the enthalpy of reaction is given by the slope in Figure 6-3.

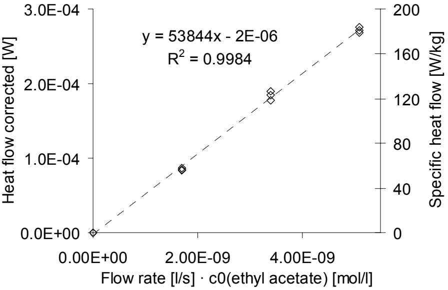

Figure 6-3: Determination of the enthalpy of reaction of ethyl acetate 0.1 mol·l^{-1} with NaOH 1 mol·l^{-1}, T=40°C. The experimental points (corrected with the correction factor F) are represented in W and the corresponding specific heat flow of each point is represented in W·kg^{-1} in the right ordinate scale.

The enthalpy of reaction determined experimentally was -53.8 kJ·mol^{-1} in good agreement with the value reported in the literature -54.7 kJ·mol^{-1}[34, 91]. The error is less than 2 %. The range of specific heat flows measured in this experiment varied from 50 to 170 W·kg^{-1}.

This experimentally determined enthalpy of reaction is also very close to the typical value of -53.4 kJ·mol^{-1} obtained during control experiments using a Calvet calorimeter (Figure 6-4) and 500 µl of each solution.

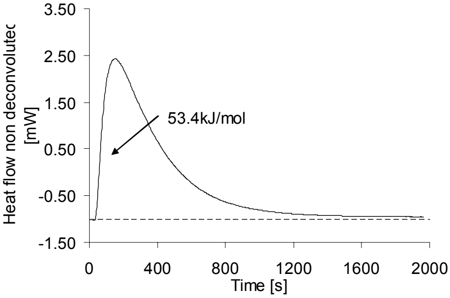

Figure 6-4: Enthalpy of reaction obtained during control experiment in a Calvet calorimeter at 40°C. Raw signal without deconvolution.

We will come back to the Calvet measurement and detail the operating conditions in subsection §6.4.2.2.

6.3.2.2 Determination of kinetics parameters

The concentrations were then changed to slow down the reaction and study the kinetics. The reaction of ethyl acetate 0.8 mol·l^{-1} with NaOH 1 mol·l^{-1} was performed at 5 different temperatures. As mentioned in the previous subsection, the Design 4 microchannel was used. The residence time in the reaction channel was changed by varying the flow rate of the entering fluids.

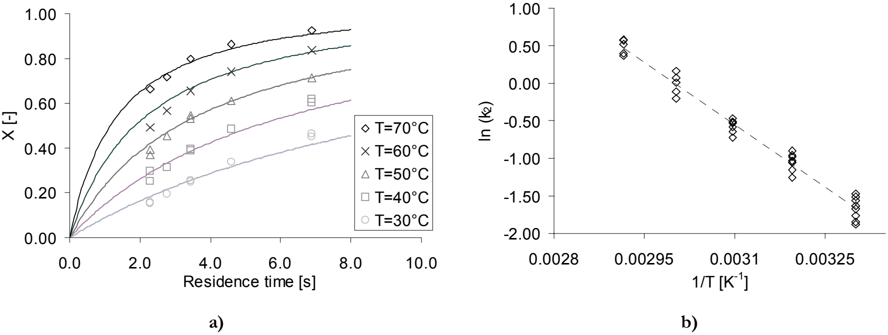

a) b)

Figure 6-5: Reaction kinetics of ethyl acetate 0.8 mol·l-1 with NaOH 1 mol·l-1 at various temperatures. a) experimental data, b) Arrhenius plot from these data.

The experimental conversions were then used to calculate the corresponding kinetic constant k_2 for each point using equation (6.13) developed in subsection §6.3.1.4. The activation energy obtained from the Arrhenius plot of Figure 6-5b was 46.1 kJ·mol^{-1}. This is close to the theoretical value of 47.3 kJ·mol^{-1} reported by Kirby et al. [94]. The kinetic parameter k_2 can be extrapolated at 25 °C and is 0.140 l·mol^{-1}·s^{-1}. Papoff [91] observed that this value depends on the concentration of NaOH and measured a k_2 equal to 0.141 l·mol^{-1}·s^{-1} with NaOH 1 mol·l^{-1}.

These results validate the suitability of the system for the determination of reaction kinetics.

In the control experiment performed with a Calvet calorimeter, the kinetic parameters calculated were much lower than the ones predicted from the literature (0.12 l·mol^{-1}·s^{-1} at 40 °C and 0.14 at 60 °C). The corresponding energy of activation is then approximately 10 kJ·mol^{-1}. Mixing is thus the rate limiting step of this system (more explanation in subsection §6.4.2.2). This reaction is too fast to be followed in this system.

6.3.3 Importance of the diameter of the outlet tube

In the original design of the microreactor, the outlet tube had an inner diameter of 0.65 mm. However with this layout, a systematic error was detected in the kinetics. The measured heat flows were systematically higher than expected. It was suspected that part of the heat measured was due to reaction outside of the reaction channel i.e. in the outlet tube.

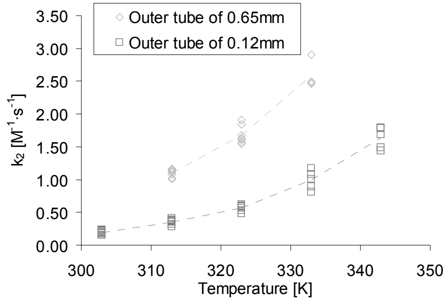

Figure 6-6: Identification of the systematic error induced by an outlet tube of large diameter. Kinetic constants determined experimentally with a outlet tube having an internal diameter of 0.65 mm or 0.12 mm.

The results presented in Figure 6-6 were both obtained with a microchannel of design 4. As shown in this figure, the kinetics parameters k_2 were significantly higher with large outlet tubes. The error varied by a factor 3.1 to 2.6 for temperatures increasing from 313 °K to 333 °K. This confirmed that the heat released in the outlet tube was part of the heat flow measured (as represented in Figure 6-7).

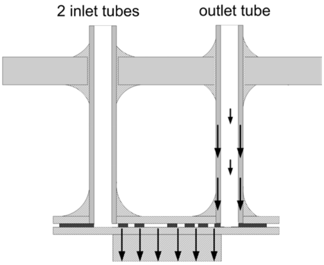

Figure 6-7: Scheme of the hypothetic heat flows in the microsystem. Influence of the heat released in the outlet tube on the heat flow measured.

The mechanism of heat transfer is probably a combination of conduction through the tube and diffusion through the liquid. The contribution of each of these phenomena can be evaluated as follows:

The resistance to conduction through the stainless steel tube can be calculated as described in chapter 5 (subsection §5.5.3, $R = \delta / (\lambda \cdot A)$) and is 130 K·W^{-1}. The resistance to conduction through the fluid in the outlet tube can be estimated with the same method at 3200 K·W^{-1} considering the thermal conductivity of water (0.6 W·m^{-1}·K^{-1}). Since the latter resistance is high compared to the resistance of the tube, heat conduction through the fluid can be neglected.

The Bodenstein number in the outlet tube can be calculated as explained in Chapter 3 and varies from 80 to 200 in the range of flow rates used for the experiments. Back mixing can therefore also be neglected.

As a first approximation it can be concluded that the heat transfer from the outlet tube to the calorimetric sensor is mainly due to conduction through the stainless steel tube.

It was noticed in chapter 5 that the temperature of the aluminum screen was close to the oven temperature. Above the aluminum screen, the temperature of the tube decreases and reaches room temperature at its top. As a first approximation, one may consider that the heat released in the area below the aluminum screen (5 mm) is entirely measured i.e. conducted to the sensors. Residence times should then be recalculated integrating this new volume. This was done both for an outlet tube of 0.65 mm and of 0.12 mm; the results are shown in Figure 6-8.

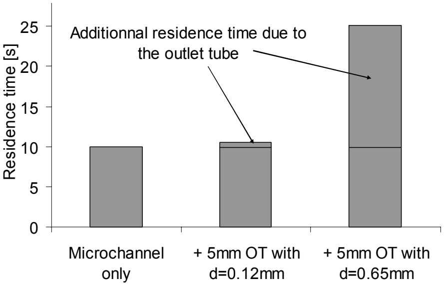

Figure 6-8: Estimated influence of the size of the outlet tube (OT) on the residence time when the first 5 mm are taken into consideration. Calculations made for the microchannel of design 4.

Calculations were made for the design 4 (L=44 mm) and with a fixed flow rate to obtain a 10 s residence time in the reaction channel. Figure 6-8 shows that the residence times are multiplied by 2.5 when the outlet tube has a diameter of 0.65 mm. This explains the systematic error observed in Figure 6-6. This problem is even further emphasized when smaller reaction channels are used. The reduction of the diameter size from 0.65 mm to 0.12 mm results into a significant decrease of this error.

The remaining predicted error in terms of residence time for an outlet tube of 0.12 mm and a reaction channel length of 44 mm (design 4) would be 5 %. This calculation relies however on the assumption that, as with larger outlet tubes, the main part of the heat released in the first five millimeters of the small outlet tube is conducted to the sensor. But the reduced section and wall thickness of the tube strongly affects the heat conduction. The resistance of losses of the small tube estimated using the method presented above corresponds to 390 $K \cdot W^{-1}$ i.e. 3 times higher than for the larger outlet tube. With such a resistance value, the influence of the heat conduction through the tube can be neglected.

The size of the outlet tube does not interfere with the results as long as the conversion of the reaction is complete at the end of the channel. It is therefore not a problem when working with instantaneous reactions (for example with the reaction of calibration). It is also not a problem for the determination of heat of reaction. However it becomes an important parameter when the residence time in the reaction channel is required for calculations as for the determination of reaction kinetics. All kinetic results presented in this work have been obtained with microreactors with a small outlet tube.

The study of a model reaction in our microchannel permits thus to put in light and to solve problems related to the design of the microreactor. The second part of this chapter is dedicated to the study of reactions generating high heat flows. This was the principal motivation of the development of this new microreactor-based system.

6.4 APPLICATION TO REACTION GENERATING HIGH HEAT FLOWS

The range of heat flows allowing to work in isothermal condition was first estimated using finite element modeling. Experiments with two reactions generating high heat flows were then performed and studied in the microchannel.

6.4.1 Simulations using finite element modeling

The properties of this new calorimetric system were estimated by a simplified model using finite elements. The limit for thermal explosion and the limit for maintaining isothermal condition were compared with a calorimetric system classically used in safety laboratories, i.e. the differential scanning calorimeter DSC.

This model allowed the assessment of the temperature profile in the reactor when various heat flows are released.

6.4.1.1 Hypothesis and parameters of the model

The major hypothesis of this simulation was that the heat was transferred by **conduction** only. No convection was taken into account. This hypothesis is valid for the microchannel but is more debatable in the case of the DSC crucible which has a higher volume. The calculated limits (limit for isothermal conditions and limit of explosion) are therefore probably slightly too strict in the case of the crucible but this will anyway give us an interesting approximation.

The crucible was treated like an equivalent sphere and the microchannel like an infinite cylinder. Using the dimension of a standard DSC crucible, the radius of the equivalent sphere calculated was 1.6 mm. For the microchannel, a rectangular shape of 250 μm width and 100 μm depth was taken into consideration, the corresponding hydraulic radius was then 72 μm (see chapter 4 for the calculation of the hydraulic radius).

The heat transfer coefficient was estimated, from experimental measurements, as 500 $W \cdot m^{-2} \cdot K^{-1}$ for the DSC crucible and as 10'000 $W \cdot m^{-2} \cdot K^{-1}$ for the microchannel. The other parameters of the model were defined as follow: $\lambda = 0.1\ W \cdot m^{-1} \cdot K^{-1}$, $\rho = 1'000\ kg \cdot m^{-3}$, $C_p = 1'800\ J \cdot kg^{-1} \cdot K^{-1}$, $E_a = 100'000\ J \cdot mol^{-1}$.

The geometries were divided into 100 small elements and a thermal balance was calculated for each element.

6.4.1.2 *Comparison of the microsystem with a DSC calorimeter*

For both systems, the heat flow released in the reactor was varied and the corresponding increase of the temperature profile was calculated. Isothermal conditions were defined as an augmentation of the temperature profile of less than 1 °C.

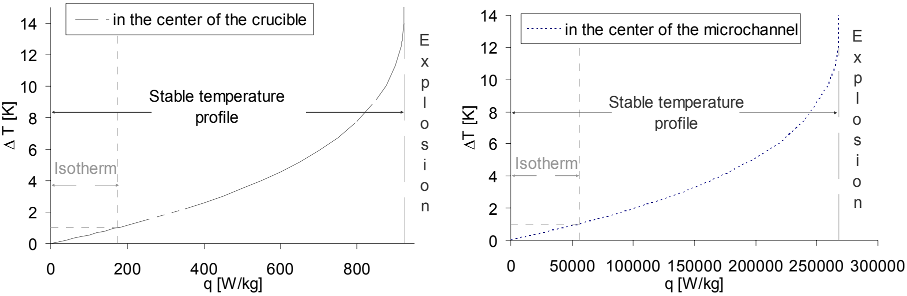

a) b)

Figure 6-9: Comparison of the limit of thermal explosion in a DSC crucible (a) and in the microchannel (b).

The conclusions of Figure 6-9 are summarized in Table 6-1.

Table 6-1: Summary of the calculated limits for isothermal conditions and of thermal explosion for both systems.

	DSC crucible	**Microchannel**
Limit for isothermal conditions	175 $W \cdot kg^{-1}$	56'000 $W \cdot kg^{-1}$
Limit of thermal explosion	923 $W \cdot kg^{-1}$	268'000 $W \cdot kg^{-1}$

In the microchannel, strictly isothermal conditions can be maintained even for heat flows 300 times higher than in a DSC crucible (Table 6-1). The low value of 175 $W \cdot kg^{-1}$ obtained for the crucible is due to the hypothesis of pure conduction but also to the strict definition of isothermal conditions.

Clearly, this new system should open new possibilities in the characterization of highly exothermal reactions.

6.4.1.3 *Comparison of the microsystem with an adiabatic calorimeter*

Adiabatic calorimeters are typically used for the study of the decomposition of highly exothermal compounds. One of the best performing equipment for such studies is the APTAC from Setaram which can follow temperature increases up to 400 °C·min^{-1}.

In an adiabatic calorimeter, a heat flow of 56'000 W·kg^{-1} (limit for isothermal conditions in the microchannel calculated in the preceding subsection) corresponds to a temperature increase of 1'866 °C·min^{-1} (see equation (6.16)).

$$dT/dt = \dot{q}/C_p = 56'000/1'800 = 31.1\left[°C \cdot s^{-1}\right] \Rightarrow 1866\left[°C \cdot \min^{-1}\right] \tag{6.16}$$

This heat flow is too high to be measured even in an adiabatic calorimeter.

6.4.2 Experimental validation

The simulations using finite elements modeling presented above showed that isothermal conditions should be obtained up to heat flows of 56'000 W·kg^{-1}. This estimate was checked experimentally by using the reaction of unsaturated ethers in a methanolic acidic solution.

6.4.2.1 *Calibration at high heat flows*

The first step was to check that linearity was maintained when the calibration reaction was performed at higher concentrations and higher flow rates.

The neutralization of H_2SO_4 0.6 mol·l^{-1} with NaOH 0.6 mol·l^{-1} was performed at 40 °C with flow rates of the feed streams varying from 10 to 25 µl·min^{-1}.

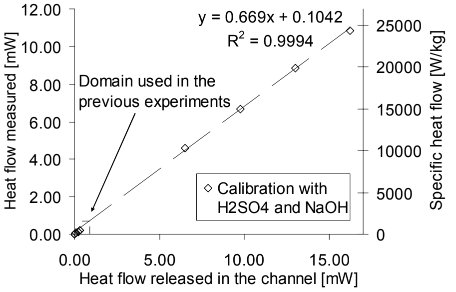

Figure 6-10: Calibration reaction: neutralization of H_2SO_4 0.6 mol·l^{-1} by NaOH 0.6 mol·l^{-1} at 40°C at flow rates varying from 10 to 25 µl·min^{-1}.

As shown in Figure 6-10, linearity was maintained up to the highest heat flow tested corresponding to 25'000 W·kg^{-1}.

6.4.2.2 Characterization of the reaction of two unsaturated ethers with methanol in acidic solution

The reaction of two unsaturated ethers with 2.5 % H_2SO_4 in methanol (see (II)) was studied both in a Calvet calorimeter and in the microreactor-based calorimeter.

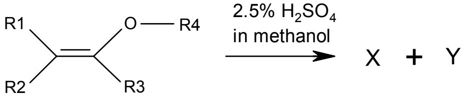

(II)

No thermal data were available on these two compounds and the mechanism of reaction was unknown. The objective of this work was to determine the kinetic parameters i.e. the order of the reaction for the different species, the frequency factor and the activation energy of the two reactions. One of these compounds was the cause of a serious chemical accident.

In a Calvet calorimeter BT 2.15

A parallel study was performed with a classical Calvet calorimeter to compare with the performance of our system. This calorimeter was selected because it allows working with small amounts of chemicals (adapted for the very exothermal reactions tested) and with mixing cells (adapted for fast reactions).

This calorimeter shows a better sensitivity than a DSC and a lower detection limit. The limit of heat saturation can moreover be raised from 35 mW until 350 mW by activating a heat flow attenuation. This calorimeter is described in more details in Chapter 2.

For all measurements in the Calvet calorimeter described in this chapter, glass mixing cells were used. These cells consist of two intertwined glass vessels containing respectively the reactant A and the reactant B. After temperature equilibration, the upper part of the glass cell is broken and the reactants are mixed.

In the following experiments, the thermal signal had to be deconvoluted because the time constant of the system (equal to 214 s) was much longer than the reaction time. For the deconvolution, the differentiation method and the Fourier transform analysis were both tested and showed similar results. The differentiation method was chosen.

Reaction of unsaturated ether A with a methanolic solution of H_2SO_4 *2.5%*

Ether A (150 µl) was introduced in the lower part of the glass mixing cell and the upper part was filled with 150 µl of the methanolic acidic solution (H_2SO_4 2.5 %).

The enthalpy of reaction was determined by integrating the heat flow released by the reaction as a function of time. The average value obtained was -44 kJ·mol^{-1}. For these experiments, the heat flow was attenuated to increase the limit of saturation.

Investigations for the determination of the activation energy were then carried out. The temperature was decreased down to -31 °C (Figure 6-11).

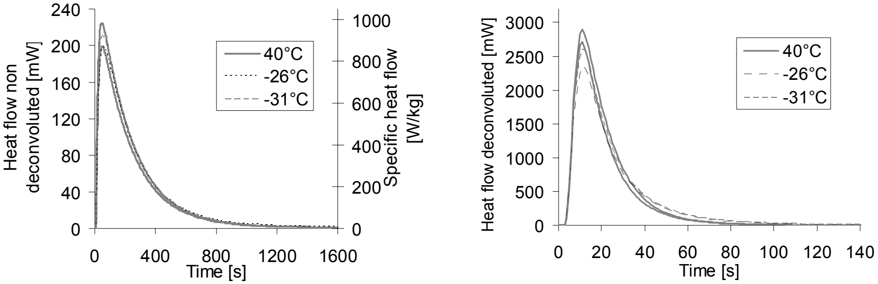

a) b)

Figure 6-11: Thermal signals obtained for the reaction of A at 40 °C, -26 °C and -31 °C, a) raw signal, b) deconvoluted signal.

The highest heat flow detected in this experiment corresponded to a real heat flow of 1000 W·kg^{-1} (due to the heat attenuation).

As seen in the deconvoluted curves (Figure 6-11b), due to the poor mixing achieved in this cell, the reaction was limited by diffusion even at a temperature of -31 °C. The variations observed between the maxima of the curves were within experimental error. Mixing was the result of diffusion and of natural convection induced by the addition of the second reagent. The time required for radial diffusion alone can be estimated at 20.3 s (the internal diameter of the cell was 9 mm and the diffusion constant used was $1 \cdot 10^{-8}$ m^2·s^{-1}).
The curves peaked at a time of 12 s; this can be used as an estimate of the time of mixing.

From this measurement, one can only conclude that this reaction is complete in less than 12 s even at -30 °C and has a low apparent energy of activation. This reaction is much too fast to be studied further in this system.

Reaction of unsaturated ether B with a methanolic solution of H_2SO_4 2.5 %

The reaction of the unsaturated ether B with a methanolic acidic solution was then studied at two temperatures. The enthalpy of reaction determined for this reaction was -39 kJ·mol^{-1}.

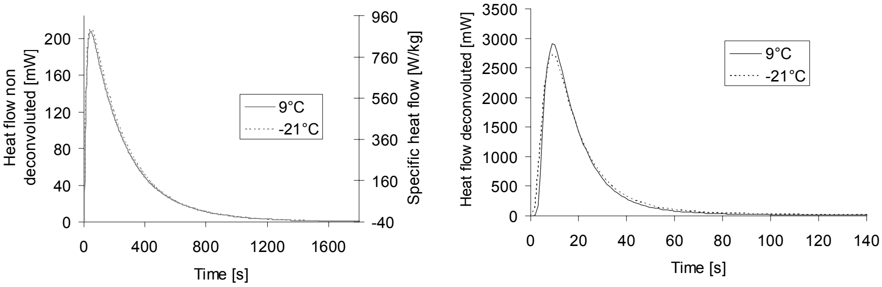

a) b)

Figure 6-12: Signal obtained for the reaction of B at 9 °C and -21 °C: a) raw signal measured, b) after deconvolution.

With regard to the kinetic study, as seen in Figure 6-12, the same observations can be made as in the previous paragraph. Within experimental error, the maxima of the curves were identical for the two experiments carried out at 30 °C of difference. The reaction is too fast to be followed in this type of calorimeter.

No other classical calorimetric system could be found to characterize both reactions.

In the microreactor-based calorimeter

Reaction of the unsaturated ether A with a methanolic solution of H_2SO_4 2.5 %

The reaction of the unsaturated ether A with a methanolic acidic solution was then investigated in the microreactor-based calorimeter.

A reference experiment was performed at 40 °C. The concentrations were maintained constant and the flow rates were varied. The raw data obtained are shown in Figure 6-13.

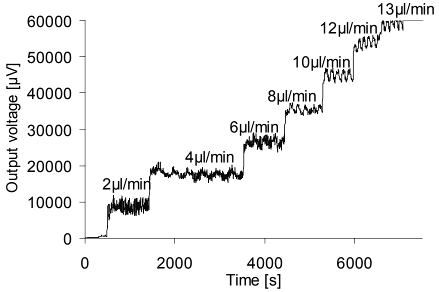

Figure 6-13: Raw data obtained for the reaction of A with methanol in acidic solution 2.5 % H_2SO_4, T=40 °C, Flow rates of the feed streams were 0, 2, 4, 6, 8, 10, 12 and 13 µl·min^{-1}.

The enthalpy of reaction determined using the raw data of Figure 6-13 was -41.5 kJ·mol^{-1} (Figure 6-14).

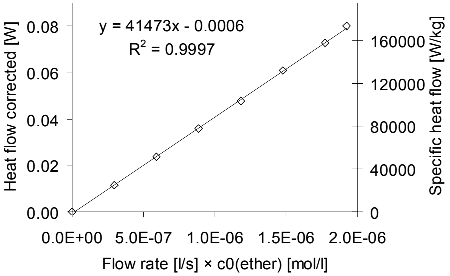

Figure 6-14: Reaction of the unsaturated ether A with an acidic methanol solution at T=40°C, determination of the enthalpy of reaction.

The heat flows measured in this experiment ranged between 23'000 W·kg^{-1} and 160'000 W·kg^{-1}. As explained in chapter 5, the linearity of the experimental points proves that there was no heat accumulation in the outlet fluids i.e. that isothermal conditions were maintained even at the highest value of 160'000 W·kg^{-1}.

The calculation of the corresponding conversion for each residence time is represented in Figure 6-15.

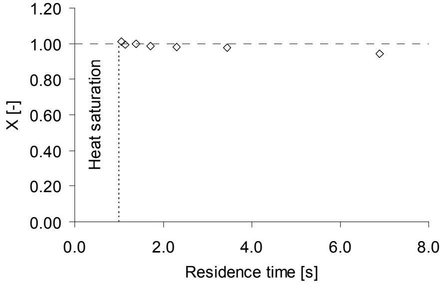

Figure 6-15: Reaction of unsaturated ether A with a methanolic acidic solution at T=40 °C. Estimation of the time of reaction.

Figure 6-15 shows that the reaction time was shorter than 1 s. The limit of saturation was reached at flow rates corresponding to the shortest residence time. This can be avoided by using a shorter microchannel. Experiments were performed with a microchannel corresponding to the design 1 described in chapter 3 but no significant additional information could be obtained since mixing became limiting for residence times below 1 s (see chapter 4).

Determination of the reaction order

In order to investigate the global kinetics of this reaction, additional experiments were performed varying the concentrations of the reactants and maintaining the temperature at 40 °C.

Since methanol was used as solvent, and was therefore present in large stoechiometric excess in the reaction its concentration can be considered as constant.

In a first series of experiments, the concentration of the ether was maintained constant and the amount of acid was decreased (Figure 6-16).

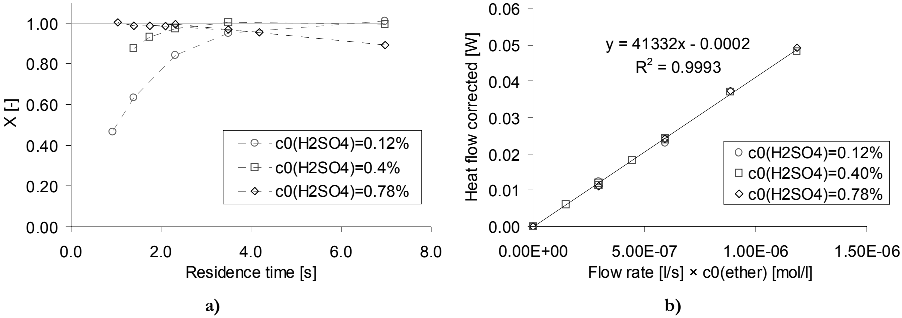

Figure 6-16: Influence of the acid concentration, T=40 °C, on the conversion rate (a) and on the enthalpy of reaction calculated relating to the ether concentration (b).

A decrease in the conversion rate was observed for acid concentrations below 0.4 %. Figure 6-16b shows that the enthalpy of reaction remained constant even at the lowest acid concentration. The acid was therefore not in stoechiometric defect even if its concentration was much lower than the ether concentration. This indicates that the acid probably works as a reaction catalyst.

The conversion rates of ethyl acetate obtained in Figure 6-16a were then used to calculate the kinetic constant k_1 of the reaction. This was done assuming a first order reaction and using equation (6.8) developed in subsection §6.3.1.4 (Figure 6-17).

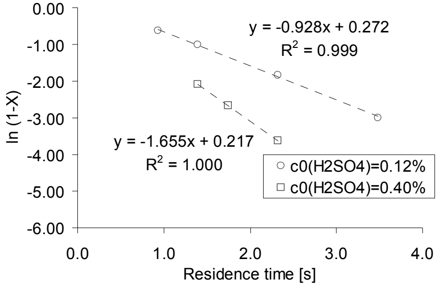

Figure 6-17: Estimation of the kinetic constant at two acid concentrations, 0.12 % and 0.40 %, T=40°C.

The linearity of the regressions confirmed that the reaction kinetics was first order with regard to the ether concentration as assumed. However, the kinetic constant varied with the acid concentration. This confirmed the catalytic action of the acid. In fact, for a fixed temperature, the catalyst lowers the energy of activation of the reaction and thus increases the kinetic constant; this effect can be increased with higher concentrations of catalyst.

The second series of experiment performed was the dilution of the reaction mass in a solvent. Ether A and the acid (at the original concentration of 2.5 %) were diluted while maintaining their ratio constant.

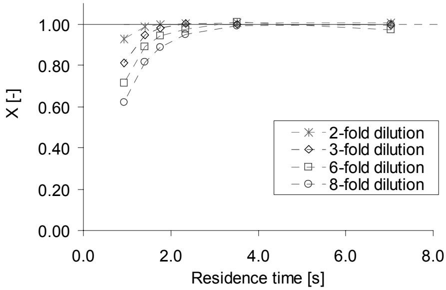

Figure 6-18: Influence of the dilution of ether A and acid at a constant ratio, T=40 °C.

A heat of mixing was observed between the solvent used for the dilution of the ether and methanol and was determined as explained in section §6.2.1. The results in Figure 6-18 are corrected for this enthalpy.

Using the results presented in Figure 6-18 and assuming first order kinetics, the kinetic constant k_1 can be determined (equation (6.8) developed in section §6.3.1.4, Figure 6-19).

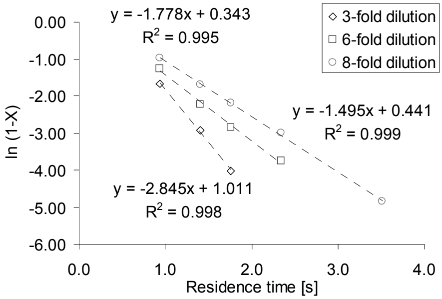

Figure 6-19: Determination of the first order kinetic constant, T=40°C.

The results obtained with 3-fold, 6-fold and 8-fold dilutions were only used. For the 2-fold dilution data, most of the points had a conversion equal to one and therefore only very few points could be used.

Combining the results presented in Figure 6-17 and Figure 6-19, a relationship between the value of the kinetics constant and the amount of catalyst can be deduced (Figure 6-20).

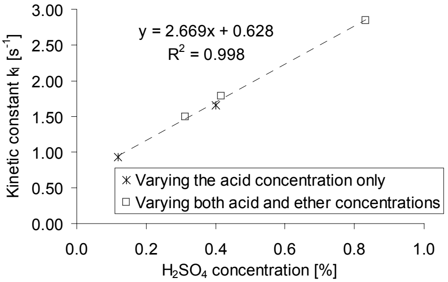

Figure 6-20: Relationship between the kinetic constant and the acid concentration.

Thus, in the range of concentration tested, the kinetics constant varied linearly with the amount of acid. This relation can be described using the following expression:

$$k_1 = k_0 + k_c \cdot \left[H^+ \right] \tag{6.17}$$

k_c corresponds to the slope of the curve i.e. 2.67 and k_0 to the ordinate at the origin i.e. 0.63. The latter corresponds to the kinetics constant without catalyst.

According to Figure 6-20, equation (6.17) becomes then:

$$k_1 = 0.63 + 2.67 \cdot \left[H^+ \right]$$

A brief investigation on the role of methanol in the reaction. In the previous subsection, it was shown that the reaction of the ether A with a methanolic acidic solution followed a first order kinetics catalyzed by the acid. However, as methanol was in large excess, the kinetics might in fact be a pseudo-first-order kinetics where the ether reacts with methanol. The resulting product is represented in (III).

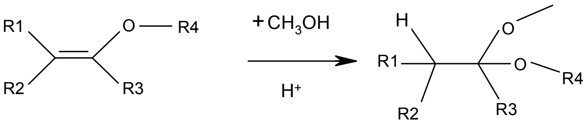

(III)

The reactivity of ether A with methanol was tested to get a better insight of this aspect (Figure 6-21).

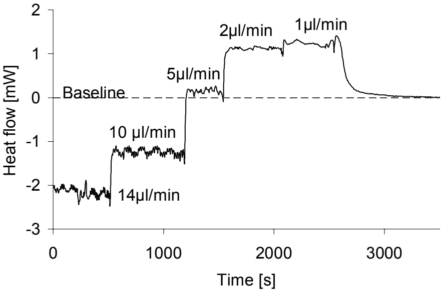

Figure 6-21: Raw signal obtained by the microcalorimeter for the reaction of the unsaturated ether A with pure methanol, T=40°C.

As can be seen in Figure 6-21, an endothermic signal was observed at high flow rates i.e. at short residence times. This is typical of a mixing enthalpy. For small flow rates i.e. longer residence times, an exothermal heat flow was measured. This heat flow increased with decreasing flow rates which is typical for an incomplete exothermal reaction.

There is thus a slow exothermal reaction between the ether A and the methanol. This reaction is however too slow to be characterized in the microreactor-based system.

Determination of the energy of activation

The activation energy of the reaction was determined by varying the temperature of the oven. The standard concentration of 2.5 % H_2SO_4 in methanol was used for these experiments (Figure 6-22).

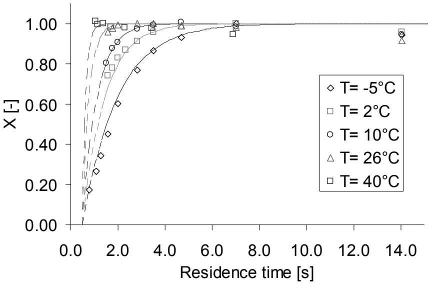

Figure 6-22: Determination of the energy of activation for the reaction of unsaturated ether A with a methanolic solution of H_2SO_4 2.5 %.

The standard technique consisting of using equation (6.8) to calculate the kinetic constant and then drawing an Arrhenius plot as done in subsection §6.3.2.2, was not applicable in this case as it appears from the experimental point that the time zero wasn't properly defined. A first approximation of the kinetics parameters was thus obtained in this case by fitting the experimental data using a model of first order reaction in the mathematical program Berkeley Madonna as represented in Figure 6-22.

The activation energy determined using this technique was 35.8 $kJ \cdot mol^{-1}$. The frequency factor k^0 was $6.4 \cdot 10^6$ s^{-1}.

The kinetic constant k at 40 °C was extrapolated and corresponds to 6.9 s^{-1}. This correlates well with the extrapolated value from Figure 6-20, which is 7.3 s^{-1} at a concentration of 2.5 % (6 % of error in extrapolation).

It appears from Figure 6-22 that the best fits of the experimental data were obtained for a conversion of zero at t=0.5 s. For such fast reactions, contrary to what was predicted with simulations (section §6.2) for rather fast model reactions, the diffusion of species has to be taken into account to better fit the results. Unfortunately, as explained in section §6.2, the simulation of such rapid reactions could not be performed with the software FEMLAB.

The data fit represented in Figure 6-22 is obviously not exact because even if mixing is not complete for residence times below 0.5 s (see chapter 4), the molecules react as soon as they are in contact with each other and part of ether A should be converted before 0.5 s. To take this into account, a better model had to be found.

One may divide the phenomena into two parts, the radial diffusion of the species in the channel and their reaction. The time required for each step determines the shape of the conversion curve. A second kinetic constant is therefore defined to characterize the rate of diffusion of the protons. The diffusion of the ether molecules was not taken into consideration since it is approximately ten times slower than the diffusion of protons. The diffusion-reaction system could thus be written as follows:

$$H' \xrightarrow{k_D} H$$
$$A' \xrightarrow{k_{rx}\,(=f(c_H)),\,H} P$$

H represented the protons that have diffused and reached the ether molecules A. The linear relationship between the kinetics constant of the reaction k_c and the amount of catalyst (established in previous paragraph and represented in Figure 6-20) can be simplified as follows,

$$\mathrm{k}_{\mathrm{rx}} = \left(\frac{\mathrm{k}^0 \cdot \exp(-E_a / R \cdot T)}{c_{0 H_2SO_4}} \right) \cdot c_H \qquad (6.18)$$

with $c_0(H_2SO_4)$ being the total acid concentration that has to diffuse. The resulting fit is shown in Figure 6-23.

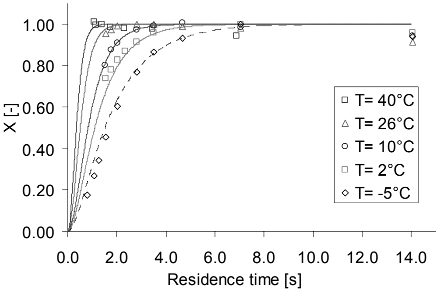

Figure 6-23: Fitting of the curve using a diffusion-reaction model.

The kinetic constant of mixing diffusion k_D determined for the better fit was 2.25 s^{-1} and corresponded to the diffusion of 90 % of the protons in 1 s. This is close to the experimental time for radial diffusion measured in chapter 4.

The activation energy of the reaction was then 35.7 $kJ \cdot mol^{-1}$and the frequency factor $5.8 \cdot 10^6$ s^{-1}.

This correlates well with the results obtained with the first fits taking only the reaction into account.

Reaction of the unsaturated ether B with a methanolic solution of H_2SO_4 2.5 %

The reaction of the unsaturated ether B with 2.5 % H_2SO_4 in methanol was then studied. The enthalpy of reaction determined experimentally was around 40 $kJ \cdot mol^{-1}$. The product of the reaction was a dark-red sticky liquid that tended to block the thin outlet tube. The microreactor had therefore to be changed frequently.

To determine the activation energy of this reaction, isothermal experiments were performed at various temperatures (Figure 6-24).

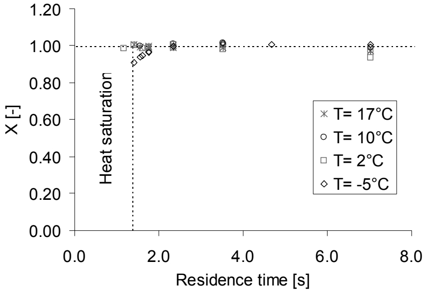

Figure 6-24: Determination of the energy of activation for the reaction of the unsaturated ether B with a methanolic solution of H_2SO_4 2.5 %.

As seen in Figure 6-24, the reaction was even faster than the reaction of ether A. The reaction was complete in less than 1 s even at a temperature of 2 °C. At -5 °C, a decrease of the conversion rate was observed for residence times shorter than 2 s. These values were however still very close to the experimental error and the energy of activation could not be determined under these conditions.

The current layout of the calorimeter could not be stabilized at temperatures below -5 °C due to water condensation and freezing of the heat carrier layer.

6.5 DETERMINATION OF KINETICS IN THE TEMPERATURE SCANNING MODE

In the previous experiments, the isothermal mode was used. The temperature was maintained constant during the experiment and the flow rates were changed to vary the residence time in the channel.

Interesting experiments can however be performed in the temperature scanning mode. In this approach, the flow rates are maintained constant and the temperature is varied slowly following a slope chosen by the operator.

Figure 6-25 shows an example of the raw data measured for the reaction of ether A in methanolic acidic solution for an inlet flow rate of 8 μl·min^{-1} and for a temperature scanning rate of 0.6 °C·min^{-1}.

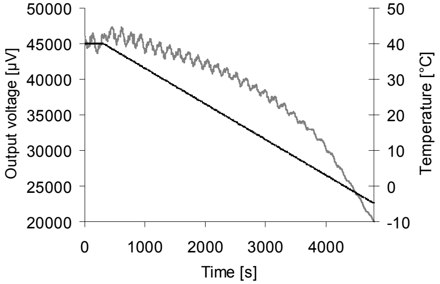

Figure 6-25: Reaction of unsaturated ether A with a methanolic solution of H_2SO_4 2.5 %. Raw data of the temperature scanning mode (inlet flow rate of 8 µl·min^{-1}, scanning rate: 0.6 °C·min^{-1}).

Five different scans were performed varying the inlet flow rates of the fluids at respectively 2, 4, 6, 8 and 11 µl·min^{-1}. The same scans were performed with the solvent (methanol) and used as baseline. The output voltages were converted into heat flow signals and plotted versus temperature. For visibility reasons, only three of them are shown in Figure 6-26.

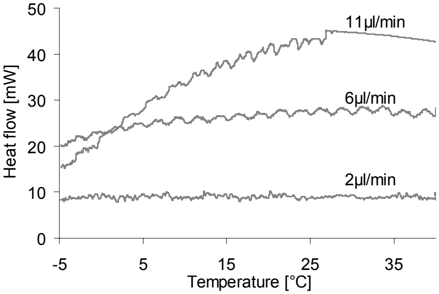

Figure 6-26: Examples of three temperature-scans varying the inlet flow rates of the fluids.

At a flow rate of 2 µl·min^{-1}, there was no influence of the temperature on the heat flow; the reaction was complete in the entire range of temperature scanned. At a flow rate of 11 µl·min^{-1}, the reaction was complete at a temperature above 27 °C. Below this temperature, a drop in conversion was observed. This type of experiment allows to identify the appropriate range of experimental parameters for the kinetics determination.

The oscillations detectable in each curve were observed for all measurements. They were attributed to the pump since their oscillation frequencies increased with flow rates and their amplitude increased with the heat flows involved.

6.5.1 Comparison with the results obtained in isothermal mode

In order to compare the results obtained in scanning mode with those obtained in the isothermal mode, the conversion achieved during the scanning measurement was calculated at five discrete temperatures corresponding to the five isotherms presented in the previous subsection.

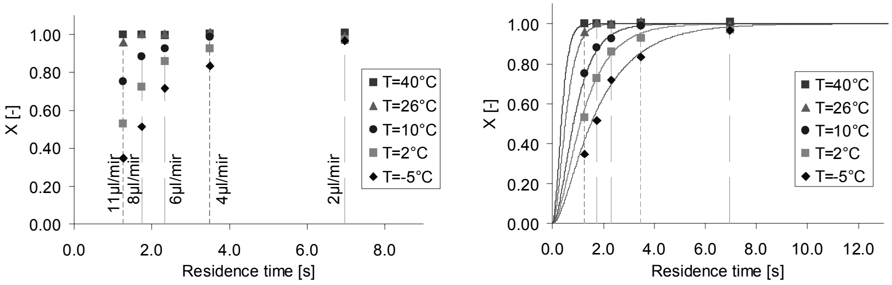

a) b)

Figure 6-27: a) Representation of the 5 scans performed at various inlet flow rates, b) comparison with the curves fitted using the isothermal mode.

The curves fitted using the results of isothermal mode (Figure 6-23) were introduced in Figure 6-27b. As seen on this figure, the results correlated well with the previous ones.

One of the advantages of this mode compared to the isothermal mode is that the manipulations performed by the operator are reduced: i.e. once the flow rate is set and stabilized, the temperature scan is entirely automatic. In the isothermal mode, the flow rate has to be manually changed approximately every 15 minutes.

6.5.2 Determination of the activation energy with a single scan

Moreover, with this mode, an approximation of the activation energy of a reaction could be obtained by performing a single experiment. This is exemplified in Figure 6-28.

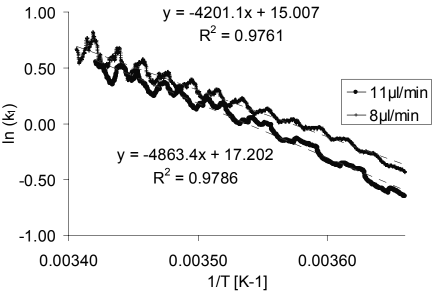

Figure 6-28: Estimation of the energy of activation using the temperature scan mode. Assessment of the precision using two different flow rates 8 µl·min^{-1} and 11 µl·min^{-1}.

In Figure 6-28, the points corresponding to temperatures below 0 °C were not taken into account because the small fluctuations observed in the baseline generated a significant error in the regression curve. The activation energy[4] estimated using this technique was 34.9 and 40.4 $kJ \cdot mol^{-1}$ for the curves obtained respectively at flow rates of 8 and 11 $\mu l \cdot min^{-1}$. The deviation difference between these two values was close to 13 %. The results were thus not as precise as the ones obtained previously using the isothermal mode. The errors due to baseline corrections and to the sensitivity correction become important when only one experiment was performed. However this method allowed obtaining easily and rapidly a good approximation of the energy of activation.

6.5.3 Rapid identification of the working range of reactions

The temperature scan mode allows to identify very rapidly whether a reaction is potentially too fast or too slow to be studied in this system (Figure 6-29).

To detect if a reaction is potentially too fast, one simply has to set the flow rate at the maximal value (limited by heat saturation and by the mixing time) and to check that a decrease of temperature induces a drop in conversion. For example, in the case of the reaction of ether B, it was predictable in just a single experiment that the reaction could not be studied in this system. On the other hand, one can check that a reaction is not too slow by setting the flow rate at a low value and verify that at the higher temperature the heat flow tends to a maximum.

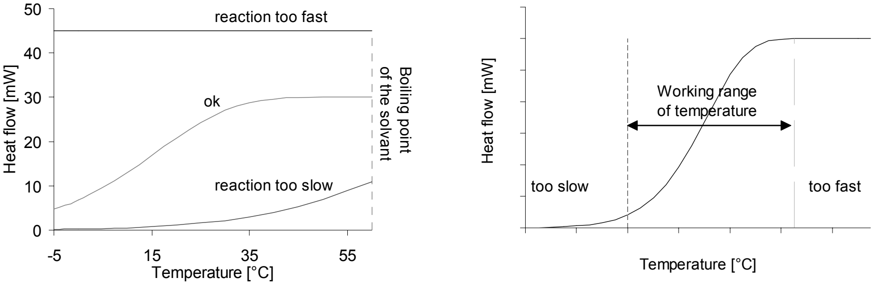

a) b)

Figure 6-29: Rapid identification of the reactions that can be studied in the new microreactor-based calorimetric system a) suitable reaction for a fixed range of temperature, b) identification of the working range of temperature of a reaction.

These experiments also provide information on the working range with respect to temperature.

---

[4] The kinetic constant k_1 was estimated assuming a first order reaction (as determined in section §6.4.2.2). The effective reaction start was set at t=0.5 s as determined in the fit of the Figure 6-22.

6.6 LIMITS OF THE SYSTEM: EXAMPLE OF THE HYDROLYSIS OF ACETIC ANHYDRIDE IN ACIDIC SOLUTION

As shown in the previous subsection, the microsystem developed displays some interesting properties. However, its application is not adapted to all types of reaction and the hydrolysis of acetic anhydride in acidic solution is a good example of a reaction, which is very difficult to characterize in this novel system. This reaction is much slower than the other reactions presented before and only small heat flows are involved. This reaction has been widely described in the literature [95-97].

Acetic anhydride is mixed with acetic acid in a 1:1 w/w ratio. The adjunction of acetic acid was done to facilitate the mixing of the acetic anhydride with the aqueous solution [96] which are otherwise poorly miscible.

The mixture of acetic anhydride and acetic acid was introduced in the first syringe and the aqueous solution of HCl 0.1 mol·l^{-1} was introduced in the second one. The flow rates were changed between 0 and 1 $\mu\text{l·min}^{-1}$ and the kinetic parameters were determined using the equations derived in section §6.3.1.

6.6.1 The baseline problem

When small thermal signals were measured, the variation of the baseline with time became an important issue.

The heat flow induced by the microsystem filled by the chemical compounds of interest with zero flow is typically used as the baseline. However the time required for the baseline stabilization may be very long and can induce some error on the heat flow evaluation when the signal measured is small (Figure 6-30).

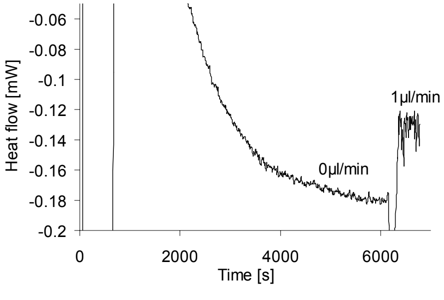

Figure 6-30: Example of a measurement limited by the variation of the baseline: hydrolysis of acetic anhydride in acidic solution, microchannel of design 3, T=40°C.

The limit of detection of heat flow is thus given by this baseline variation.

Some investigations were performed to identify parameters that have an influence on the baseline deviation and on the time required for baseline stabilization. The most influent factors were:

- the diffusion of the reacting species in the tubes,
- the thermal equilibration due to the aluminum screen,
- the amount of heat carrier layer used,
- the life time of the microcalorimetric chip.

When working with higher heat flows, this problem was considerably reduced and small variations of the baseline did not significantly affect the precision of the measurements (Figure 6-31). Higher heat flows can be obtained by using a longer microchannel (for example design 4) and working at higher temperature.

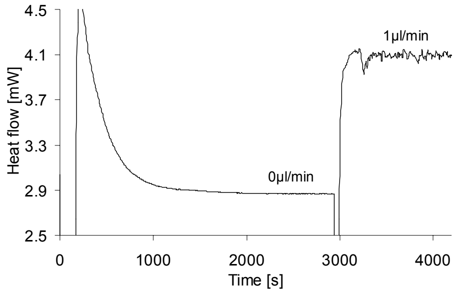

Figure 6-31: Example of a measurement where the variation of the baseline can be neglected: hydrolysis of acetic anhydride in acidic solution, microchannel of design 4, T=50 °C.

This effect is even less important when working with highly exothermal reaction, which was the main aim of this work.

6.6.2 Determination of the enthalpy of mixing

As explained in section §6.3.1, for the characterization of kinetic parameters in a flow-through microreactor, a precise determination of the mixing and reaction enthalpies is required. The enthalpy of mixing was estimated using the technique explained in section §6.3.1 for a temperature of 50 °C. The flow rates of the feed streams were varied from 3 to 20 $\mu l \cdot min^{-1}$. The results are shown in Figure 6-32.

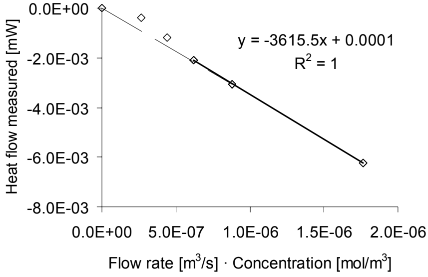

Figure 6-32: Assessment of the enthalpy of mixing of the hydrolysis of acetic anhydride in acidic solution at 50°C.

In Figure 6-32, the three points corresponding to the higher flow rates were on a straight line (feed streams of respectively 7, 10 and 20 µl·min^{-1}). The enthalpy of mixing estimated from the slope of this curve was +3.6 kJ·mol^{-1}. The contribution of the enthalpy of reaction at such flow rate seems to be low but both processes i.e. the endothermic mixing and the exothermal reaction are so closely linked that one cannot ensure that the integrality of the mixing enthalpy was measured.

This value is in contradiction with Becker et al. [96, 98] who reported a heat of mixing of -5 kJ·mol^{-1} at 25 °C but is in agreement with the value reported recently by Zogg et al. of 3 kJ·mol^{-1} at 55°C. The conditions used in both cases were however different from the one used in the present experiment since Becker et al. used 6 g of mixture acetic anhydride/acetic acid mixed with 100 ml of an aqueous solution of HCl 0.1 mol·l^{-1}. Zogg et al. used the same proportions but with a total volume of 35 ml. Literature references using conditions suitable for our system have not been found.

The precise determination of this heat of mixing has a tremendous influence on the calculation of the corresponding conversion.

Moreover, even mixed with acetic acid, acetic anhydride is very poorly miscible with water and this may also influence the time of mixing.

6.6.3 Determination of the enthalpy of reaction

The reaction was performed at 70 °C in the long microchannel of design 4. The flow rates required at that temperature for complete conversions were between 0 and 0.6 µl·min^{-1}. However, as seen in chapter 4, at flow rates below 1 µl·min^{-1}, back diffusion in the inlet tubes becomes important between the pulses of the pump. No significant result for the enthalpy of reaction could thus be obtained. The value of literature had therefore to be used.

6.7 CONCLUSIONS

In conclusion, the determination of the kinetic parameters of a model reaction, the saponification of ethyl acetate in alkaline solution, allowed validating the suitability of the system for the determination of reaction kinetics.

Moreover, the application of the system to reactions generating high heat flows showed that isothermal conditions can be obtained for heat flows up to 160'000 $W\cdot kg^{-1}$.
The kinetics of reaction of unsaturated ether A in acidic solution was then investigated. Precious information concerning the global kinetics and the reaction rate could be obtained in a short period of time.

Experiments in the temperature scanning mode were shown to offer new possibilities in the application of this system. Indeed the energy of activation of an unknown reaction can be estimated with an error of 10 % in about 1 hour.

However, this novel system cannot be extended to all types of chemical reactions. This microsystem is designed for the characterization of highly exothermal reactions and the measurement of small heat flow faces some limitations due to baseline variations. Moreover in order to be precisely studied in this microsystem, the reaction should be fast enough to permit the characterization of the enthalpy of reaction in the microchannel and should have a low mixing enthalpy.

Chapter 7

SUMMARY AND CONCLUSIONS

7.1 OVERVIEW OF THE MAIN RESULTS

The characterization of the global kinetics and exothermy of reactions is a crucial aspect for process safety analysis. However, the study of fast exothermal reactions in liquid phase still raises several major problems in classical systems. Indeed, both the control of the temperature and a sufficiently rapid mixing are difficult to achieve.

In the present thesis, a novel microreactor-based calorimeter is proposed. This system combines a microfluidic system with a commercially available calorimeter (Setline 120, Setaram, France). The high surface to volume ratio of the microreactor leads to a high heat exchange rate, which allows working in isothermal conditions even when high heat flows are generated. The small radius of the channel provides short times for radial diffusion i.e. short mixing times.
The work principle of the calorimeter used for the thermal measurement line is very similar to the work principle of a DSC except that no reference crucible is required. In the novel system proposed, the original crucible containing the sample is replaced by a flow-through microreactor.

Two different ways were tested for the construction of the microreactor. The first technique investigated, the spark-assisted chemical engraving of glass, was abandoned since it did not fulfill our requirements. The silk-screen printing of a thick-film dielectric was found to be a sufficiently precise, inexpensive and flexible technique for building the microchannels. The geometry and especially the length of the microchannel could be adapted to the type of reaction (Figure 7-1), a long reaction channel being used for slow reactions and a short one for rapid reactions.

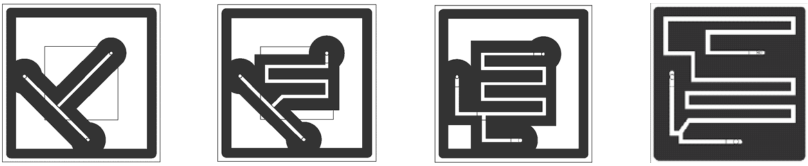

Design 1	**Design 2**	**Design 3**	**Design 4**
d = 0.25 mm	d = 0.25 mm	d = 0.25 mm	d = 0.25 mm
L = 2.85 mm	L = 11.30 mm	L = 18.75 mm	L = 44.00 mm
e = 0.10 mm	e = 0.10 mm	e = 0. 10 mm	e = 0. 10 mm

Figure 7-1: Drawings of the four different designs. Design 3 was the most frequently used in the experiments.

After the construction of the microchannel, the degree of mixing achieved at the end of the reaction channel was assessed. This was done by calculation of the Reynolds and of the Bodenstein number, by CFD simulations (using the mathematical program FEMLAB) and confirmed experimentally. The calculation of the Bodenstein number predicted that the rapid radial diffusion of solutes in the small channel would result in a distribution of residence times corresponding to a plug flow reactor.

All approaches tested converged to the conclusion that the flow was purely laminar in the microchannel and that the time of mixing was the time required for radial diffusion. For the microreactors used (d=250 μm and e=100 μm), this time was 0.5 s for protons.

The flow in the microchannel was also visualized and recorded in real time using Laser-Induced-Fluorescence (LIF) measurements. This allowed checking that no unpredicted disturbances were produced in the flow. The laminar flow obtained in the microchannel was clearly visible (Figure 7-2).

a) b)

Figure 7-2: Inlet of Design 3, 2 μl·min^{-1} a) picture taken by LIF measurements, b) FEMLAB-based simulations.

The microreactor was then introduced in the cavity of the calorimeter and thermal measurements were started. The system was calibrated using the neutralization of sulphuric acid by NaOH.

For flow-through reactors, the global heat flow $\dot{q}_{rx}$ released by the reaction in the channel is:

$$\dot{q}_{rx} = \dot{V} \cdot (-\Delta H_r) \cdot c_0 \cdot X \tag{7.1}$$

In the first experiment performed, the microreactor was simply placed on the measuring membrane of the calorimeter and only 10 % of the heat flow released in the reaction channel was actually measured by the sensor. This ratio was called the thermal efficiency *F*:

$$F = \dot{q}_{meas} / \dot{q}_{rx} \tag{7.2}$$

Various modifications were subsequently performed on the microreactor design (contact pin, heat carrier layer…) to guide the heat flow to the sensors of the membrane and limit the losses. The thermal efficiency increased up to 80 %. It was shown from the heat flow balance that the limiting part of the system i.e. the highest remaining resistance of the system was the thermal contact between the microreactor and the sensors, especially at the level of the heat carrier layer introduced to avoid an air layer.

Another important improvement was the preheating of the entering fluids at the oven temperature. An efficient and reproducible preheating of the entering fluids was achieved electrically by introducing small resistances in a layer glued to the tubes.

The final set-up of the system is represented in Figure 7-3.

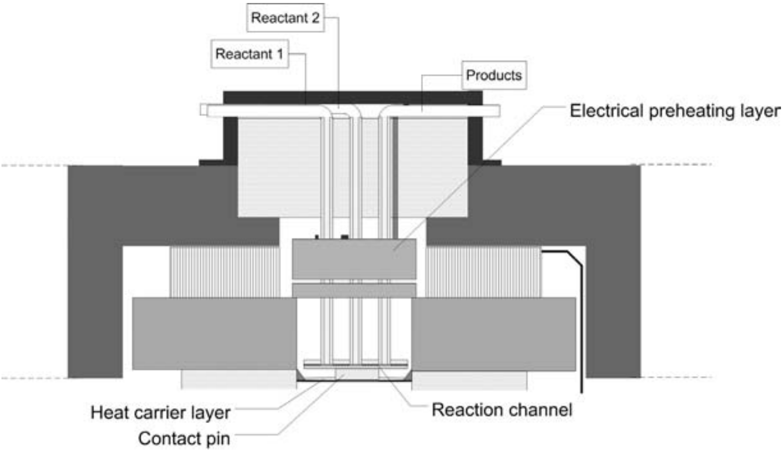

Figure 7-3: Final configuration of the microcalorimetric system.

The suitability of the system for the determination of reaction kinetics was assessed. The saponification of ethyl acetate in alkaline solution, a reaction well-characterized in the literature, was used as model reaction. The residence time in the microchannel was varied by varying the flow rate of the feed streams and the conversion rate achieved at the end of the reaction channel was determined. The enthalpy of reaction was determined in a first step by choosing conditions of concentration and temperature assuring a complete conversion at the end of the channel (see equation (7.1), Figure 7-4a). In a second step, the temperature was varied to assess the activation energy and the frequency factor (see Figure 7-4b).

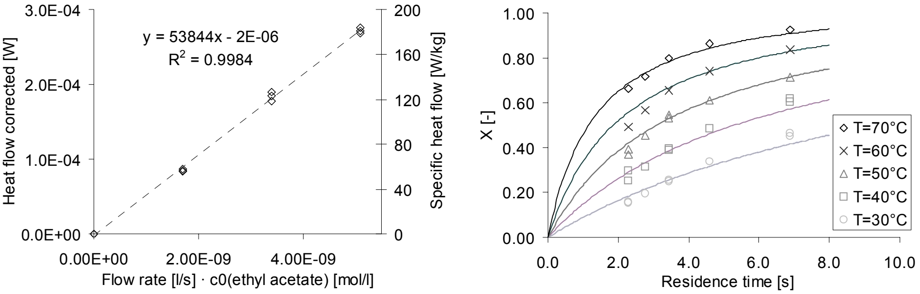

a)

b)

Figure 7-4: Reaction of ethyl acetate with NaOH. a) Determination of the enthalpy of reaction at 40°C, b) Determination of the activation energy.

The kinetic parameters obtained with the novel calorimeter were very close to ones reported in the literature. This allowed the validation of both the thermal measurements and the thermal analysis method.

Reactions generating higher heat flows were then investigated. Finite element modeling of the heat conduction in the microchannel predicted that isothermal conditions would be maintained in the microchannel for heat flows even 200 times higher than in a DSC i.e. for heat flows of 56'000 W·kg^{-1}. This feature allowed carrying out the kinetic study of a still undefined fast exothermal reaction.

Experiments showed that isothermal conditions were achieved for heat flows up to 160'000 W·kg^{-1} - the maximum heat flow tested. Such high heat flows were obtained during the characterization of the reaction of an unsaturated ether A with an acidic methanol solution (see Figure 7-5a).

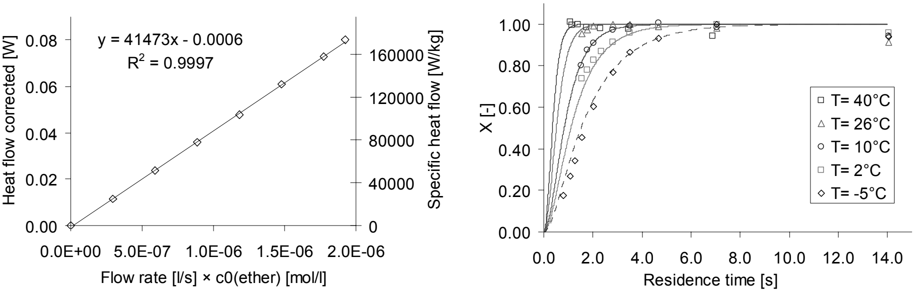

a)

b)

Figure 7-5: Reaction of the unsaturated ether A with an acidic methanol solution, a) Determination of the enthalpy of reaction at 40°C, b) Determination of the activation energy.

The order of reaction was determined by varying the concentrations whereas the activation energy was assessed by varying the temperature (see Figure 7-5b).

Finally, experiments were performed in a temperature-scan mode. As for DSC calorimeters, this scanning mode leads, in less than one hour, to important data such as the working range of reaction or an approximation of the activation energy.

The system presented here shows a number of attractive abilities. Although according to the inherent safety principles, such fast exothermal reactions should rather be avoided in chemical processes, the ability of mastering them opens new opportunities for the fine chemical industry. As the proverb says, "To defeat the enemy, one must first know the enemy". A better understanding of fast reactions will result in the optimization of the production conditions as well as in the optimization of preventive and protective safety measures.

Figure 7-6 compares the usability domain of the microsystem proposed in this thesis with the usability domain of classical systems described in chapter 2.

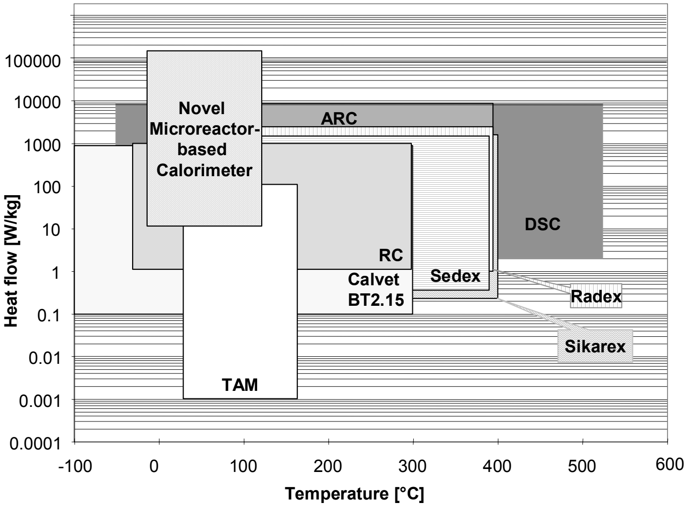

Figure 7-6: Comparison of the usability domain of our system compared to the classical systems presented in chapter 2.

As can be seen in Figure 7-6, this system allows the measurement of heat flows at least more than 10 times higher than in classical systems.

7.2 PERPECTIVES

Even if the first objective of this novel microreactor-based calorimeter was the determination of the kinetic parameters of fast exothermal reactions, the application of this system to other types of problems should be investigated in the light of the exciting results obtained by now.

For example, systematic reactivity studies can be investigated in isothermal mode. The main reactant is introduced continuously in the microchannel and its reactivity with various compounds can be quickly tested. The compounds to test are introduced consecutively in the microchannel using two different pumps, switching from one to the other (e.g. with an electrovalve). The kinetic parameters of the reacting compounds can be approximated by performing a temperature-scanning of the mixture of interest directly after having observed the thermal effects in isothermal mode. No additional manual operations are required and very small amounts of chemicals are needed since low flow rates are involved. Information such as the influence of the solvent on the reaction or the decomposition or interaction tables of compounds can be obtained.
It can also be used for the determination of heats of dilution or of reaction enthalpies for instance when only small amounts of chemicals are available.

The major limitations of this system are still:

- the precise characterization of reactions showing an important mixing enthalpy,
- the restriction to liquid phase reactions leading to liquid products,
- the time of mixing in the case of organic molecules instead of protons.

The first two limitations are related in an intrinsic way to reactions in a plug-flow microreactor and are difficult to avoid. However, the integration of analytical measurements e.g. a gas chromatograph, in parallel with the calorimetric measurements could allow fixing the problem related to the badly characterized mixing enthalpy. The investigation of this aspect was begun and a microchannel allowing the inlet of a quencher at the end of the channel was constructed. With the latter design, the reaction is stopped at the end of the reaction channel and the conversion achieved can be analyzed off-line by gas chromatography. The comparison of the thermal conversion with the chemical conversion for one experiment should ensure that the mixing enthalpy determined experimentally is correct.

The third limitation of the system referred above can easily be avoided. Indeed, the time of mixing can still be significantly improved by using other designs of micromixers. This point was not investigated further since the reactions tested involved mainly protons which have a high diffusion constant. T-mixers and V-mixers were chosen in this study since they are easy to construct. However, it is commonly known that the mixing achieved in these mixers is poor compared to many other designs.

The next table presents some mixers reported in the literature to achieve better mixing.

Table 7-1: Examples of micromixers providing a better mixing than the T or V-mixers used in this work.

Mixer with multi-lamination	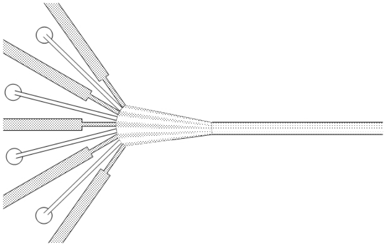	Stream of reactants distributed in different inlets. Distances for radial diffusion decrease and thus the time required for the mixing decrease [43].
Chaotic mixing	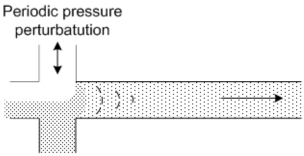	Stretching and folding of material lines e.g. by applying a transversal pressure to the main stream. Pressure drop unsteady and chaotic regime obtained [99].
Microjet mixers	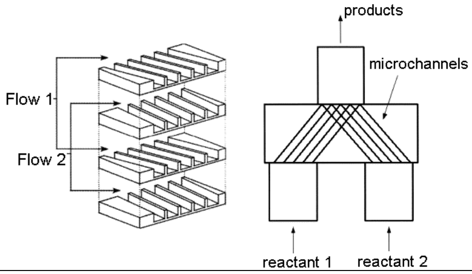	Uses multi-lamination. Division of the flow done in 3-dimensions. Mixing can be provided by parallel channels (P-microjet mixers) or by crossed microchannels (V-microjet mixers) [71].
Static mixer Möbius type	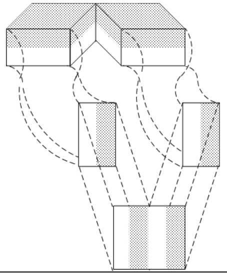	Twisted band where the layers of two non-miscible fluids are separated perpendicular to the boundary layers, subsequently twisted and reunited [100], [101].

The four micromixers presented in Table 7-1 could be used for calorimetric measurements in the novel microcalorimeter.

A new technique was recently developed in the Laboratory of microtechnical production (LPM, Institute of Production and Robotics, EPFL): the "Low Temperature Co-fired Ceramic" method or LTCC. With this technique, different layers of ceramic can be designed and superposed. A three dimensional mixing can be obtained. Figure 7-7 shows an example of a simple Y-shaped microreactor constructed in ceramics using this technique.

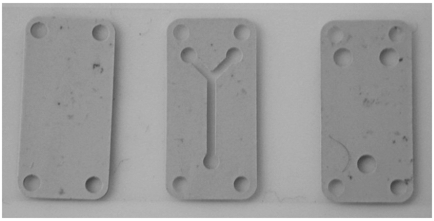

Figure 7-7: Example of a simple microreactor constructed using LTCC techniques.

Even if, in the example presented above, the mixing of the reactants takes place in a single layer, one can imagine mixers where the flow passes from one layer to the next inducing multi-lamination of the fluid layers as described by Schwesinger et al. [101]. This opens a new dimension in microchannel design. Obviously, one has to ensure that the heat released in any place of the reaction channel is equally conducted to the sensors. Otherwise the thermal signal obtained would be difficult to interpret.

Chapter 8

REFERENCES

1. http://slp.icheme.org/incidents.html.
2. Kletz, T.A., *Learning from accidents in industry*, ed. Butterworths. 1988, London.
3. Marschall, V.C., *Major Chemical Hazards (Ellis Horwood series in chemical engineering)*, ed. E. Horwood. 1987, Chichester.
4. Steen, H., *Das Bhopal-Unglück 1984*, ed. Umweltbundesamt. 1987, Berlin.
5. *Rhein-Bericht, Bericht der Bundesregierung über die Verunreinigung des Rheins durch die Brandkatastrophe bei der Sandoz AG/Basel*, ed. N.u.R. Bundesminister für Umwelt. 1987, Bonn.
6. Stoessel, F., *Design thermally safe semi-batch reactors.* Chemical Engineering Progress, 1995. **91**(9): p. 46-53.
7. Stoessel, F., *Intégration de la sécurité dans les stratégies de développement de procédés.* Actes du colloque: la sécurité dans la conduite des procédés chimiques, Paris, CNAM, 1997: p. 1-8.
8. Kletz, T.A., *Inherently Safer Design: The growth of an Idea.* Process Safety Progress, 1996. **15**(1): p. 5-8.
9. Laurent, A., *Emballement thermique*, in *Sécurité des procédés chimiques: connaissances de base et méthodes d'analyse de risques.*, T. DOC, Editor. 2003, Lavoisier: Nancy. p. 273-314.
10. Willson, R.J., *Calorimetry*, in *Principles of Thermal Analysis and Calorimetry*, P.J. Haines, Editor. 2002, RSC. p. 129-165.
11. Pastré, J., *Beitrag zum erweiterten Einsatz der Kalorimetrie in frühen Phasen der chemischen Prozessentwicklung*, in *Safety and Environmental Technology Group*. 2000, ETH Zurich. p. 13-25.
12. Höhne, G., *Thermal analysis and calorimetry*, in *Ullman's Encyclopedia of industrial chemistry*, J. Wiley, Editor. 2000, Wiley-VCH.
13. Hemminger, W. and G. Höhne, *Calorimetry: Fundamentals and practice*, ed. V. Chemie. 1984, Weinheim.
14. Regenass, W., *The development of heat flow calorimetry as a tool for process optimization and process safety.* Journal of Thermal Analysis, 1997. **49**: p. 1661-1675.
15. Schildknecht, J., *Reaction calorimeter for applications in chemical process industries: performance and calibration.* Thermochimica Acta, 1981. **49**: p. 87-100.
16. Stoessel, F., *Personal communication "Domaine d'utilisation"*. 2001: Lausanne.
17. Stoessel, F., *Polycopié de cours "La sécurité des procédés chimiques", 8ème semestre, section Génie Chimique*, in *EPFL*. 2002: Lausanne.

18. Van Herwaarden, A.W. and P.M. Sarro, *Thermal sensors based on the seebeck effect.* Sensors and Actuators, 1986. **10**(3-4): p. 321-346.
19. Lerchner, J., A. Wolf, and G. Wolf, *Recent developments in integrated circuit calorimetry.* J. Therm. Anal. Cal., 1999. **57**(1): p. 241-251.
20. Setaram, *User manual BT2.15.* 2003: Caluire, France.
21. Point, R.P. and P.C. Gravelle, *Reconstruction of Thermokinetics from Calorimetric Data by Means of Numerical Inverse Filters.* J. Therm. Anal., 1979. **17**: p. 383-393.
22. Cesari, E.G. and J. Gutenbaum, *Recent Progress in Numerical Methods for the Determination of Thermokinetics.* J. Therm. Anal., 1981. **20**: p. 47-59.
23. Navarro, J.T. and V. Rojas, *Détermination d'une Thermogenèse par Analyse Harmonique. Application à l'Étude Calorimetrique des Amalgames.* Rev. Gén. Therm, 1973. **143**: p. 1137-1143.
24. Ortin, J.R., V. Torra, and J. Vinals, *Thermogenesis: Determination of the Thermokinetic Parameters.* Thermochimica Acta, 1984. **76**: p. 325-332.
25. Zogg, A., *A combined approach using calorimetry and IR-ATR spectroscopy for the determination of kinetics and thermodynamic reaction parameters*, in *Safety and Environmental Technology Group.* 2003, ETH Zurich.
26. Stoesser, P.R. and S.J. Gill, *Precision Flow-Microcalorimeter.* The review of scientific instruments, 1967. **38**(3): p. 422.
27. Huang, Y.-C. and B.E. Eichinger, *Flow microcalorimetry on dilute polymer solutions.* Polymer, 1977. **18**: p. 55.
28. Gill, S.J., N.F. Nichols, and I. Wadsö, *Calorimetric determination of enthalpies of solution of slightly soluble liquids I. Application to benzene in water.* J. Chem. Thermodynamics, 1975. **7**: p. 175-183.
29. Monk, P. and I. Wadsö, *A Flow Micro Reaction Calorimeter.* Acta chimica Slovenica, 1968. **22**: p. 1842-1852.
30. Monk, P. and I. Wadsö, *Flow Microcalorimetry as an Analytical Tool in Biochermistry and Related Areas.* Acta chimica Slovenica, 1969(23): p. 29-36.
31. Kemp, R.B. and I. Lambrecht, *La vie est donc un feu pour la calorimétrie: half a century of calometry - Ingemar Wadsö at 70.* Thermochimica Acta, 2000. **348**: p. 1-17.
32. Picker, P., C. Jolicoeur, and J. Desnoyers, *Steady state and composition scanning differential flow microcalorimeters.* J. Chem. Thermodynamics, 1969. **1**: p. 469-483.
33. Desnoyers, J., C. Jolicoeur, and P. Picker, *Flow calorimeter.* 1973, University of Sherbrooke: United States Patent 3'726'644.
34. Roux, A., et al., *Enthalpies of reaction and reaction rates by flow microcalorimetry: Ester Hydrolysis in basic medium.* Journal of Solution Chemistry, 1980. **9**: p. 59-73.
35. Lerchner, J., et al., *On-line monitoring of enzyme Activities using Microreactor Heat Power Meters*, in *IMRET 3: Proceedings of the Third International Conference on Microreaction Technology.* 1999. p. 469-478.
36. Lerchner, J., et al., *Accuracy in integrated circuit (IC) calorimeters.* Thermochim. Acta, 2002. **382**(1-2): p. 65-76.
37. Kohler, J.M. and M. Zieren, *Chip reactor for microfluid calorimetry.* Thermochim. Acta, 1998. **310**(1-2): p. 25-35.
38. Ehrfeld, W., et al., *Potentials and realisation of microreactors.* DECHEMA Monographs. Vol. 132. 1996.
39. Wörz, O., et al., *Microreactors, a new efficient tool for optimum reactor design.* Chemical Engineering Science, 2001. **56**: p. 1029-1033.
40. Harrison, J.D., et al., *Micromachining chemical and biochemical analysis and reaction systems on glass substrates.* Sensors and Actuators B-Chemical, 1996. **33**: p. 105-109.

41. Antes, J., et al., *Use of microreactors for nitration processes.* Presentation at IMRET 4, 4th International Conference on Microreaction Technology at the 2000 Spring National Meeting of the American Institute of Chemical Engineers, Atlanta GA usa, 2000.
42. Janicke, M.T., et al., *The Controlled Oxidation of Hydrogen from an Explosive Mixture of Gases Using a Microstructured Reactor/Heat Exchanger and Pt/Al2O3 Catalyst.* Journal of Catalysis, 2000. **191**: p. 282-293.
43. Floyd, T.M., et al., *Novel Liquid Phase Microreactors for Safe Production of Hazardous Speciality Chemicals.* Microreaction technology/IMRET 3, W. Ehrfeld, ed. B.S. 2000. 2000. 171-180.
44. Lowe, H. and W. Ehrfeld, *State-of-the-art in microreaction technology: concepts, manufacturing and applications.* Electrochimica Acta, 1999. **44**(21-22): p. 3679-3689.
45. Ehrfeld, W., V. Hessel, and H. Lowe, *Modern Microfabrication Techniques for Microreactors*, in *Microreactors, New Technology for Modern Chemistry.* 2000, Wiley-VCH. p. 15-39.
46. Dietrich, T., et al., *Fabrication technologies for microsystems utilizing photoetchable glass.* Microelectronic Engineering, 1996. **30**: p. 497-504.
47. Zissi, S., et al., *Stereolithography and microtechniques.* Microsystem Technologies, 1996. **2**: p. 97-102.
48. Arnold, J., et al., *Combination of excimer laser micromachining and replication processes suited for large scale production.* Applied Surface Science, 1995. **86**: p. 251-258.
49. Ehrfeld, W. and H. Lehr, *Deep X-Ray Lithography for the production of three-dimensional microstructures from metals, polymers and ceramics.* Radiat. Phys. Chem., 1995. **45**(3): p. 349-365.
50. Lok, Y.K. and T.C. Lee, *Processing of Advanced Ceramics unsing the Wire-Cut EDM Process.* Journal of Materials Processing Technology, 1997. **63**: p. 839-843.
51. Ehrfeld, W., et al., *Micro Electro Discharge Machining as Technology in Micromachining*, in *Micromachining and microfabrication process technology II*, S.W.P.S.-C. Chan, Editor. 1996, SPIE: Bellingham, Washington. p. 332-337.
52. Kussul, E.M., et al., *Micromechanical engineering: a basis for the low-cost manufacturing of mechanical microdevices using microequipment.* Journal of Micromechanics and Microengineering, 1996. **6**: p. 410-425.
53. Masuzawa, T., et al., Annals of the CIRP, 1985(34): p. 431.
54. Egashira, K. and K. Mizutani, *Micro-drilling of monocrystalline silicon using a cutting tool.* Precision engineering journal of the international societies for precision engineering and nanatechnology, 2002. **26**(3): p. 263-268.
55. Choo, J.H., S.H. Yeo, and F.F. Tan, *Flexible tooling for localized electrochemical deposition with wire-electrodischarge grinding.* Microsystem Technologies, 2004(10): p. 127-136.
56. Fascio, V., *Etude de la microstructuration du verre par étincelage assisté par attaque chimique: une approche électrochimique.* Ph.D. Dissertation EPFL, 2002. **2691**.
57. Wüthrich, R., *Spark Assisted Chemical Engraving - A Stochastic Modelling Approach.* Ph.D. Dissertation EPFL, 2003. **2776**.
58. Fascio, V., et al., *Investigations of the spark assisted chemical engraving.* Electrochemistry communications, 2003(5): p. 203-207.
59. Prudenziati, M., *Thick film sensors*, in *Handbook of sensors and actuators- Vol 1*, S. Middelhoek, Editor. 1994, Amsterdam Elsevier.
60. Pitt, K., *Handbook of thick film technology.* 2003: Electrochemical Publications.
61. White, F.M., *Flow in Noncircular Ducts*, in *Fluid Mechanics, Fourth Edition.* 1999, McGraw-Hill. p. 357-366.
62. Flumerfelt, R.W., *Transport Phenomena*, in *Ullman's Encyclopedia of industrial chemistry*, J. Wiley, Editor. 2000, Wiley-VCH.
63. Felder, R. and R. Rousseau, *Elementary principles of chemical processes.* 1986: Wiley.
64. Peng, X.F., G.P. Peterson, and B.X. Wang, *Heat transfer characteristics of Water Flowing Through Microchannels.* Exp. Heat Transfer, 1994. **7**: p. 265.

65. Pfund, D., et al., *Pressure drop measurements in a microchannel.* Aiche Journal, 2000. **46**(8): p. 1496-1507.
66. Debray, F., et al., *Mesure des coefficients de transfert thermique par convection forcee en mini-canaux; Measurement of forced convection heat transfer coefficients in mini-channels.* Mecanique & Industries, 2001. **2**(5): p. 443-454.
67. Taine, J. and J.-P. Petit, *Convection laminaire interne. Etablissement de regime en convection forcee*, in *Transferts thermiques: Mecanique des fluides anisothermes*. 1989, Dunod Universite: Paris. p. 245-254.
68. Baerns, M., H. Hofmann, and A. Renken, in *Chemische Reaktionstechnik. Lehrbuch der technischen Chemie. Band 1*, G.T.V.S.N. York, Editor. 1987. p. 331-336.
69. Baerns, M., H. Hofmann, and A. Renken, in *Chemische Reaktionstechnik. Lehrbuch der technischen Chemie. Band 1*, G.T.V.S.N. York, Editor. 1987. p. 347-358.
70. Levenspiel, O., *The Dispersion Model*, in *Chemical Reaction Engineering*, O. Levenspiel, Editor. 1999.
71. Ehlers, S., et al., *Mixing in the offstream of a microchannel system.* Chemical Engineering and Processing, 2000. **39**: p. 291-298.
72. Marioth, E., et al., *Investigation of microfluidics and heat transferability inside a microreactor array made of glass.* Presentation at IMRET 5, 5th International Conference on Microreaction Technology Strasbourg, FRANCE, 2001.
73. Mengeaud, V., J. Josserand, and H. Girault, *Mixing processes in a zigzag microchannel: Finite Element simulations and optical study.* Analytical Chemistry, 2002. **74**(16): p. 4279-4286.
74. Favre, E., *Introduction à la modélisation avec Femlab.* 2003: 2 days courses.
75. Feynman, R., R. Leighton, and M. Sands, *Le cours de physique de Feynman: Electromagnetisme 1*, ed. N.E. Poche. 1998, Paris.
76. Hessel, V., et al., *Gas/Liquid dispersion processes in micromixers: the hexagon flow*, in *Process miniaturization: 2nd International Conference on Microreaction Technology, IMRET 2; Topical Conference Preprints*, W. Ehrfeld, I.H. Rinard, and R.S. Wegeng, Editors. 1998, AIche: New Orleans (USA). p. 259-266.
77. Bourne, J.R., F. Kozicki, and P. Rys, *Mixing and fast chemical reaction*, in *Chemical Engineering Science*, P. Press, Editor. 1981: Great Britain. p. 1643-1663.
78. Bourne, J.R., et al., *Kinetics of the Diazo Coupling between 1-Naphthol and Diazotized Sulfanilic Acid.* Industrial & Engineering Chemistry Research, 1990. **29**(9): p. 1761-1765.
79. Barthole, J., et al., *Cinétique macroscopique de la précipitation du sulfate de baryum en présence d'EDTA: une réaction chimique test pour la caractérisation de la qualité du mélange dans les réacteurs industriels.* Journal de chimie physique, 1982. **79**(10): p. 719-724.
80. Dushman, S., *The rate of the reaction between iodic and hydriodic acids.* J. Phys. Chem., 1904. **8**: p. 453-482.
81. Fournier, M.C., L. Falk, and J. Villermaux, *A new parallel competing reaction system for assessing micromixing efficiency - Experimental approach.* Chem. Eng. Sci., 1996. **51**(22): p. 5053-5064.
82. Fournier, M.C., L. Falk, and J. Villermaux, *A new parallel competing reaction system for assessing micromixing efficiency-determination of micromixing time by a simple mixing model.* Chem. Eng. Sci., 1996. **51**(23): p. 5187-5192.
83. Guichardon, P. and L. Falk, *Characterisation of micromixing efficiency by the iodide-iodate reaction system: Part I: Experimental procedure.* Chem. Eng. Sci., 2000. **55**: p. 4233-4243.
84. Guichardon, P., L. Falk, and J. Villermaux, *Characterisation of micromixing efficiency by the iodide-iodate reaction system: Part II: kinetic study.* Chem. Eng. Sci., 2000. **55**: p. 4245-4253.
85. Ehrfeld, W., et al., *Characterization of mixing in micromixers by a test reaction: Single mixing units and mixer arrays.* Ind. Eng. Chem. Res., 1999. **38**(3): p. 1075-1082.
86. Kling, K. and D. Mewes, *Two-color laser induced fluorescence for the quantification of micro- and macromixing in stirred vessels.* Chemical Engineering Science, 2004. **59**(7): p. 1523-1528.

87. Lavieille, P., et al., *Non-intrusive temperature measurements using three-color laser-induced fluorescence.* Experiments in Fluids, 2004. **36**(5): p. 706-716.

88. D'Ans, J. and E. Lax, *Taschenbuch für Chemiker und Physiker.* 1949: p. 1090-1093.

89. Levenspiel, O., *Interpretation of Batch Reactor Data*, in *Chemical Reaction Engineering*, O. Levenspiel, Editor. 1999. p. 38-65.

90. Mata-Segreda, J., *Hydroxide as General Base in the Saponification of Ethyl acetate.* J. Am. Chem. Soc, 2002. **124**(10): p. 2259-2262.

91. Papoff, P. and P.G. Zambonin, *Applicability of the quasi-adiabatic enthalpimetric method for the study of chemical kinetics.* Talanta, 1967. **14**: p. 581-590.

92. Potts, J.E. and E.S. Amis, *The alkaline hydrolysis of ethyl acetate from the standpoint of ion-dipole theory.* J. Amer. Chem. Soc., 1949. **71**: p. 2112-2116.

93. Johnson, R.E. and R.L. Biltonen, *Determination of Reaction Rate Parameters by Flow Calorimetry.* J. Amer. Chem. Soc., 1975. **97**(9): p. 2349-2355.

94. Kirby, A.J., in *Comprehensive Chemical Kinetics*, C.H. Bamford and C.F.H. Tipper, Editors. 1972, Elsevier: Amsterdam.

95. Zogg, A., U. Fischer, and K. Hungerbuehler, *A new small-scale reaction calorimeter that combines the principles of power compensation and heat balance.* Industrial & Engineering Chemistry Research, 2003(42): p. 767-776.

96. Becker, F. and W. Walisch, *Isothermal calorimetry with automatically controlled Peltier-cooling and continuous integration of the compensation power.* Z. Phys. Chem. Neue Folge, 1965(46): p. 279.

97. Asprey, S.P., et al., *Applications of Temperature Scanning in Kinetic Investigations: The Hydrolysis of Acetic Anhydride.* Chem. Eng. Sci., 1996. **51**(20): p. 4681-4692.

98. Becker, F. and A. Maelicke, *Thermokinetic measurements using the principle of heat-flow calorimetry.* Z. Phys. Chem. Neue Folge, 1967(55): p. 280.

99. Lee, Y.-K., et al., *Chaotic mixing in electrokinetically and pressure driven micro flows.* Book of Abstract, IMRET 5, 5th International Conference on Microreaction Technology, 2001: p. 43-46.

100. Mensinger, H., et al., *Microreactor with integrated static mixer and analysis system*, in *Micro total Analysis Systems*, A.v.d.B.a.P. Bergveld, Editor. 1995, Kluwer Academic Publisher. p. 237-243.

101. Schwesinger, N., T. Frank, and H. Wurmus, *A modular microfluid system with an integrated micromixer.* Journal of Micromechanics and Microengineering, 1996. **6**: p. 99-102.

Curriculum Vitae

Marie-Agnès Schneider
Born August 30, 1978, in Geneva, Switzerland
Swiss Nationality

Education

- 2001-2004: PhD in Safety of the Chemical reaction at the Swiss Federal Institute of Technology (EPFL), Lausanne, Switzerland

- 1996-2001: Obtaining of the degree of Master of Chemical Engineering at EPFL

  October 2000 - March 2001: Diploma work in Cellular Biotechnology (Professor Dr F. Wurm) at the EPFL: "The use of the yellow fluorescent protein (YFP) for the assessment of growth and viability of CHO cells in suspension".

- 1996: French Scientific Baccalauréat at St Julien-en-Genevois specialization mathematic (mention Bien)

Work experience

- 2001-2004: Supervisor of practical work for students in the Swiss Federal Institute of Technology of Lausanne (EPFL), Switzerland
  Subject: "Risk assessment using DSC calorimetry", Machine: DSC of Mettler-Toledo and DSC of Perkin-Elmer.
  Supervisor of the exercises of the course of Chemical Process Safety given by the Professor Stoessel to students in 8th semester of chemical engineering, EPFL

- 1998: Traineeship in the pharmaceutical research center Bracco Research, Geneva, Switzerland